Bloch $\vec{k}$-Selective Resonant Inelastic Scattering of Hard X-Rays from Valence Electrons of 3d-Metals

vorgelegt von

Hartmut Enkisch

November 2001

Erster Gutachter: Prof. Dr. W. Schülke
Zweiter Gutachter: Prof. Dr. W. Eberhardt

Tag der mündlichen Prüfung: 18. Dez. 2001

Contents

Introduction

Since the discovery of the characteristic x-ray lines by C. G. Barkla [Bark08], the x-ray fluorescence radiation was considered to be isotropically emanated and to be independent of the mechanism creating the core hole which is refilled during the fluorescence process. This picture has been commonly accepted until the discovery of the x-ray resonant Raman effect in the middle of the 1970s (see [Hämä89] for an introduction and see references therein).

More subtle effects like the Bloch $\vec{k}$-selectivity of resonantly excited valence fluorescence spectra remained undiscovered until the advent of intense synchrotron radiation sources and the availability of high resolution single crystal monochromators and spectrometers.

First evidence for the Bloch $\vec{k}$-selectivity of resonant inelastic x-ray scattering (RIXS) spectra was found by Rubensson *et al.* in 1990. They discovered that in the case of a resonant excitation by monochromatic photons with energies close to the Si $L_{2,3}$ binding energy (100 eV), the shape of the valence fluorescence line from a Si single crystal sample depends on the actual energy of the incident photons [Rube90]. However, at that time this observation was attributed to a multielectron excitation due to shake processes during the creation and the subsequent annihilation of the core hole.

Only two years later, Ma *et al.* presented RIXS spectra from the C K edge in diamond (284 eV), showing a more drastic dependence of the valence line shape on the incident photon energy [Ma92]. They for the first time explained this effect in terms of the electronic band structure of the sample by treating the resonantly excited fluorescence process as one single scattering process instead of using the absorption-followed-by-emission picture. Applying the Kramers-Heisenberg formula, they derived the law of Bloch $\vec{k}$-momentum conservation. It states that the difference between the Bloch $\vec{k}$-vector of the photoelectron and the Bloch $\vec{k}$-vector of the valence electron refilling the core hole, must equal the momentum $\vec{q}$ transferred to the electron system by the scattering photon. Thereby the absorption and the emission part of the scattering process are interconnected via the electronic band structure. Based on this mechanism the authors have explained the occurence of distinct spectral features in the valence fluorescence line as a function of the actual energy of the incident photons.

Miyano and coworkers proved the incident energy dependence to be caused by the electronic band structure by comparing Si $L_{2,3}$ RIXS spectra from a Si single crystal to RIXS spectra from amorphous Si, measured under identical experimental conditions. The spectra obtained from the single crystal depend on the incident energy as expected, whereas the spectra gained from the amorphous sample do not [Miya93].

By the middle of the 1990s, the law of Bloch $\vec{k}$-momentum conservation was well established. Within a short time several fundamental articles were published. In 1994 Johnson and Ma presented the first set of calculated $\vec{k}$-selective RIXS spectra [John94]. They compared the calculated RIXS spectra from the K edge of C in diamond to the previously measured ones [Ma92]. In the same year Ma gave an extensive derivation of the Bloch $\vec{k}$-conserving RIXS cross section [Ma94]. Shortly after, Ma and Blume discussed the conditions required for a Bloch $\vec{k}$-conserving scattering process [Ma95a]. They stated, that both the valence and the conduction band states have to be delocalized, and that the localization of the core hole does not disturb the Bloch $\vec{k}$-conservation as long as it is impossible to identify the atom whose core state actually has been excited. Moreover, Ma and coworkers explicitly showed the importance of a nonvanishing amount of the momentum transfer $\vec{q}$ for the RIXS process. They measured the resonantly excited Si Kβ valence fluorescence line with $\vec{q}$ parallel to the $\langle 100 \rangle$, $\langle 110 \rangle$, and $\langle 111 \rangle$ crystal axes and found the shape to show a significant dependence on the orientation of $\vec{q}$ relative to the crystal axes [Ma95b]. Thanks to the high energy of the Si Kβ radiation (1839 eV), the size of the momentum transfer $\vec{q}$ is not negligible compared to the size of the first Brillouin zone of the sample. Therefore, the photoelectron and the valence electron refilling the core hole do not have the same Bloch $\vec{k}$-momentum, as it is the case if the C K edge (285 eV) or the Si L edge (100 eV) is investigated.

In the follwing years Bloch $\vec{k}$-selective RIXS was applied to a variety of materials such as hexagonal BN at the B K edge [Jia96, Carl99, Shir01], graphite at the C K edge [Carl95, Carl99], SiC at the Si L and at the C K edge [Lüni97], and the III-IV semiconductors AlN and GaN at the N K edge and InP at the P K edge [Eise99].

However, Bloch $\vec{k}$-selective RIXS so far has not been applied to metallic samples nor has it been tested within the hard x-ray regime. In this thesis a study of RIXS at the K edge of Ni in NiAl and at the Cu K edge in metallic Cu is presented, demonstrating the validity of the Bloch $\vec{k}$-conservation for RIXS using hard x-rays and its applicability to metals and alloys. In order to do so, the measured spectra are compared to calculated ones that are based on a linearized augmented plane waves (LAPW) band structure calculation.

Moreover, four effects that may affect the Bloch $\vec{k}$-conserving RIXS process are discussed for the example of metallic Cu:

1. The interaction with phonons in the intermediate state can lead to the partial destruction of the $\vec{k}$-momentum conservation resulting in a non-$\vec{k}$-conserving fraction present in the RIXS spectra. The amount of this non-$\vec{k}$-conserving fraction is investigated by means of measurements performed at different temperatures.

2. The shift of bands due to the screening of the core hole is accounted for within a supercell calculation. Special attention will be paid to the convergence of the charge density with respect to the size of the supercell.

3. In the case of late 3d elements like Ni and Cu, the valence band is dominated by the 3d electrons whereas only a small admixture of 4p states is present. Assuming the dipolar matrix element to be two orders of magnitude larger than the quadrupolar matrix element, about 90 % of the valence fluorescence line is due to the

dipolar 4p→1s transition and approximately 10 % of the intensity stems from the quadrupolar 3d→1s transitions. The relative strength of the dipolar and quadrupolar transititions is calculated ab initio, based on the LAPW calculation.

4. The low energy tail of the valence fluorescence spectra is dominated by the KNN radiative Auger satellite, partly obscuring the shape of the Bloch $\vec{k}$-selective valence spectra. This satellite is accounted for by a semiempirical model which is derived from the resonant double differential scattering cross section. The model is validated by investigating the KMN and KMM radiative Auger satellites.

The thesis is organized as follows. Within Chapter 1 the fundamentals of Bloch $\vec{k}$-selective resonant inelastic x-ray scattering are presented. In Chapter 2 the principles of the density functional theory (DFT) and of the LAPW method are resumed. The results on NiAl are given in Chapter 3. In the following chapters the four effects mentioned above are discussed, and the results are applied to Cu in Chapter 8.

Chapter 1

Bloch $\vec{k}$-Selective Resonant Inelastic Scattering of X-rays

This chapter resumes the theoretical fundamentals of inelastic x-ray scattering and gives a short description of x-ray absorption and emission as well as nonresonant inelastic x-ray scattering processes. Then the resonant inelastic scattering scheme is evaluated revealing a law of Bloch $\vec{k}$-momentum conservation. Its implication for the lineshape of resonantly excited valence fluorescence spectra is discussed in the last section.

1.1   Inelastic X-Ray Scattering

The scattering of x-rays by an electron system can be described as follows. The incoming photon, characterized by its energy $\hbar\omega_1$, its momentum $\hbar\vec{k}_1$, and its polarization vector $\hat{\varepsilon}_1$, is scattered into an outgoing photon having the energy $\hbar\omega_2$, the momentum $\hbar\vec{k}_2$, and the polarization vector $\hat{\varepsilon}_2$. During the scattering process the energy $\hbar\omega = \hbar(\omega_1 - \omega_2)$ and the momentum $\hbar\vec{q} = \hbar(\vec{k}_1 - \vec{k}_2)$ are transferred to the electron system of the sample thereby undergoing a transition from the ground state into an excited state.

energy transfer:
$$\hbar\omega = \hbar(\omega_1 - \omega_2)$$

momentum transfer:
$$\hbar\vec{q} = \hbar(\vec{k}_1 - \vec{k}_2)$$
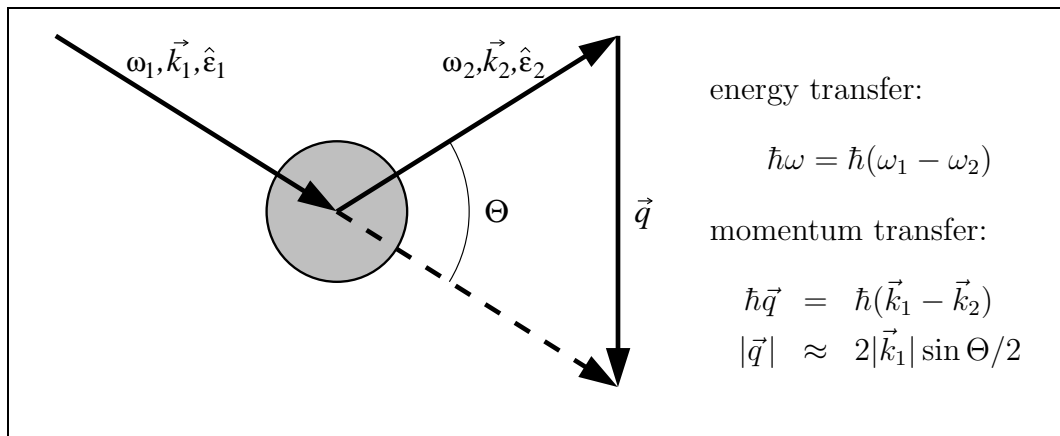$$|\vec{q}| \approx 2|\vec{k}_1|\sin\Theta/2$$

Figure 1.1: The scattering process.

Within the low energy transfer limit, when $\omega_1 \approx \omega_2$ and thus $|\vec{k}_1| \approx |\vec{k}_2|$, the momentum transfer $|\vec{q}|$ is determined by the scattering angle Θ via $|\vec{q}| \approx 2|\vec{k}_1| \sin(\Theta/2)$ (Fig. 1.1).

The quantity measured in the experiment is the double differential scattering cross section (DDSC) which is defined as the number of photons scattered into the energy interval $[\hbar\omega_2, \hbar\omega_2 + d\hbar\omega_2]$ and into the interval of the solid angle $[\Omega, \Omega + d\Omega]$ normalized to the incoming photon flux. The DDSC is related to the transition probability of the system $w_{i \mapsto f}$ by

$$\frac{d^2\sigma}{d\omega_2 \, d\Omega} = N_0 \sum_{i,f} \frac{p_i}{I_0} \, w_{i \mapsto f} \, \rho_f, \qquad (1.1)$$

where p_i is the probability for the system to be in the initial state $|i\rangle$,

$$I_0 = \frac{N_0}{V} c \quad \text{is the incident photon flux,} \qquad \rho_f = \frac{V}{(2\pi)^3} \frac{\omega_2^2}{c^3}$$

denotes the photon density of the final states and where V is the scattering volume. The electron system of the sample without external fields is described by the many particle Hamiltonian

$$\mathcal{H} = \sum_j -\frac{\hbar^2}{2m} \vec{\nabla}_j^2 + V(\vec{r}_j) \equiv \mathcal{H}_0, \qquad (1.2)$$

where the sum over j covers all electrons of the system. In the presence of a photon field the vector potential operator $\vec{A}(\vec{r}_j)$ acting on the jth electron has to be included into the kinetic energy term of the Hamiltonian:

$$\mathcal{H} = \sum_j \frac{1}{2m} \left(-i\hbar\vec{\nabla}_j - \frac{e}{c}\vec{A}(\vec{r}_j) \right)^2 + V(\vec{r}_j). \qquad (1.3)$$

The vector potential can be expanded into photon creation and photon annihilation operators a and $a^\dagger$:

$$\vec{A}(\vec{r}_j) = \sum_\lambda \sqrt{\frac{2\pi\hbar c^2}{V\omega_\lambda}} \left(\hat{\varepsilon}_\lambda \, a_\lambda \, e^{i\vec{k}_\lambda \cdot \vec{r}_j} + \hat{\varepsilon}_\lambda^* \, a_\lambda^\dagger \, e^{-i\vec{k}_\lambda \cdot \vec{r}_j} \right). \qquad (1.4)$$

where the index λ labels both the wave vector and the polarization of each photon state. Within the Coulomb gauge ($\vec{\nabla} \cdot \vec{A} = 0$) the photon field results in two additional terms in the Hamiltonian that are considered to be the interaction term $\mathcal{H}_{\text{int}}$:

$$\mathcal{H} = \sum_j -\frac{\hbar^2}{2m}\vec{\nabla}_j^2 + \underbrace{\frac{i\hbar e}{mc}\vec{A}(\vec{r}_j) \cdot \vec{\nabla}_j + \frac{e^2}{2mc^2}\vec{A}(\vec{r}_j)^2}_{\mathcal{H}_{\text{int}}} + V(\vec{r}_j) = \mathcal{H}_0 + \mathcal{H}_{\text{int}}. \qquad (1.5)$$

The photon field is only a small perturbation to the electron system and therefore can be accounted for by means of time dependent perturbation theory. Up to second

order the transition probability is then given by

$$w_{i \mapsto f} = \frac{2\pi}{\hbar} \left| \langle f | \mathcal{H}_{\text{int}} | i \rangle + \sum_m \frac{\langle f | \mathcal{H}_{\text{int}} | m \rangle \langle m | \mathcal{H}_{\text{int}} | i \rangle}{\epsilon_m - \epsilon_i} \right|^2 \delta(\epsilon_f - \epsilon_i), \qquad (1.6)$$

where $|m\rangle$ is an intermediate state. The states $|i\rangle$, $|m\rangle$, and $|f\rangle$ are compound states describing both the electron system of the sample and the photon field.

Now considerations are restricted to processes with at most *one* photon present in the initial and in the final state. Thus, the states $|i\rangle$ and $|f\rangle$ consist of the many particle states $|a\rangle$ and $|b\rangle$ of the sample and a single photon state characterized by $|\hat{\varepsilon}_1 \vec{k}_1\rangle$ and $|\hat{\varepsilon}_2 \vec{k}_2\rangle$ respectively. Accordingly, the energies ϵ_i and ϵ_f are the energies of the sample E_a and E_b plus the energies of the photons $\hbar\omega_1$ and $\hbar\omega_2$ respectively. Thus

$$\begin{aligned} |i\rangle &= |a, \hat{\varepsilon}_1 \vec{k}_1\rangle & \epsilon_i &= E_a + \hbar\omega_1 \qquad \text{and} \\ |f\rangle &= |b, \hat{\varepsilon}_2 \vec{k}_2\rangle & \epsilon_f &= E_b + \hbar\omega_2. \end{aligned} \qquad (1.7)$$

Before the transition probability for scattering processes is calculated, the transition probability for the absorption and the emission of one single photon originating from the $\vec{A} \cdot \vec{\nabla}$ term in 1st order perturbation theory is discussed (the second addend of Eq. 1.5 is inserted into the first addend of Eq. 1.6).

a) Absorption of a photon:
The photon annihilation operator a_λ of the vector potential contributes only to the DDSC if a photon with energy $\hbar\omega_\lambda$, wave vector $\vec{k}_\lambda$, and polarization vector $\hat{\varepsilon}_\lambda$ is present in the initial state and has been annihilated in the final state. With the inital and final states

$$\begin{aligned} |i\rangle &= |a, \varepsilon_1 \vec{k}_1\rangle & \epsilon_i &= E_a + \hbar\omega_1 \\ |f\rangle &= |b, 0\rangle & \epsilon_f &= E_b \end{aligned}$$
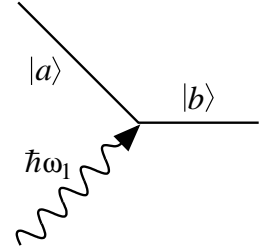
λ must equal 1 and the annihilation operator results in $\delta_{\lambda,1}|0\rangle$. Now the sum over λ can be carried out and the transition probability becomes

$$w_{i \mapsto f} = \frac{2\pi}{\hbar} \frac{2\pi\hbar c^2}{V\omega_1} \frac{e^2}{m^2 c^2} \left| \langle b | \sum_j i\hbar e^{i\vec{k}_1 \cdot \vec{r}_j} \, \hat{\varepsilon}_1 \cdot \vec{\nabla}_j | a \rangle \right|^2 \delta(E_b - E_a - \hbar\omega_1) \qquad (1.8)$$

b) Similarly the transition probability for emission processes is obtained and with

$$\begin{aligned} |i\rangle &= |a, 0\rangle & \epsilon_i &= E_a \\ |f\rangle &= |b, \hat{\varepsilon}_2 \vec{k}_2\rangle & \epsilon_f &= E_b + \hbar\omega_2 \qquad \text{one gets} \end{aligned}$$

$$w_{i \mapsto f} = \frac{2\pi}{\hbar} \frac{2\pi\hbar c^2}{V\omega_2} \frac{e^2}{m^2 c^2} \left| \langle b | \sum_j i\hbar e^{-i\vec{k}_2 \cdot \vec{r}_j} \, \hat{\varepsilon}_2^* \cdot \vec{\nabla}_j | a \rangle \right|^2 \delta(E_b - E_a + \hbar\omega_2) \qquad (1.9)$$

Spectroscopies based on these transitions are x-ray absorption spectroscopy (XAS) and x-ray emission spectroscopy (XES), giving access to the unoccupied and the occupied density of states, respectively.

The terms contributing to the transition probability of photon scattering (one photon in, one photon out) are the $\vec{A} \cdot \vec{A}$ term in 1$^{\text{st}}$ order and the $\vec{A} \cdot \vec{\nabla}$ term in 2$^{\text{nd}}$ order perturbation theory.

The $\boldsymbol{\vec{A} \cdot \vec{A}}$ **term in 1$^{\text{st}}$ order** (inserting the third addend of Eq. 1.5 into the first addend of Eq. 1.6) describes nonresonant inelastic scattering. The product of the two vector potentials yields four terms

$$A_\lambda \cdot A_{\lambda'} \propto a_\lambda a_{\lambda'} + a_\lambda a_{\lambda'}^\dagger + a_\lambda^\dagger a_{\lambda'} + a_\lambda^\dagger a_{\lambda'}^\dagger \qquad (1.10)$$

of which clearly only the second and the third contribute to the DDSC. With the definitions in Eq. 1.7 the second term persists if $\lambda = 1$ and $\lambda' = 2$, whereas the third term remains if $\lambda = 2$ and $\lambda' = 1$. Thus, the transition probability is:

$$
\begin{aligned}
w_{i \mapsto f} &= \frac{2\pi(2\pi\hbar c^2)^2}{\hbar V^2 \omega_1 \omega_2} \left(\frac{e^2}{mc^2}\right)^2 \left| \langle b| \sum_j e^{i\vec{k}_1 \cdot \vec{r}_j}\, \hat{\varepsilon}_1 \cdot e^{-i\vec{k}_2 \cdot \vec{r}_j}\, \hat{\varepsilon}_2^* |a\rangle \right|^2 \delta(E_b + \hbar\omega_2 - E_a - \hbar\omega_1) \\
&= \frac{8\pi^3 \hbar e^4}{m^2 V^2 \omega_1 \omega_2} \left(\hat{\varepsilon}_1 \cdot \hat{\varepsilon}_2^*\right)^2 \left| \langle b| \sum_j e^{i\vec{q} \cdot \vec{r}_j} |a\rangle \right|^2 \delta(E_b - E_a - \hbar\omega), \qquad (1.11)
\end{aligned}
$$

with $\vec{q} = \vec{k}_1 - \vec{k}_2$ and $\omega = \omega_1 - \omega_2$.

The $\boldsymbol{\vec{A} \cdot \vec{\nabla}}$ **term in 2$^{\text{nd}}$ order** (inserting the second addend of Eq. 1.5 into the second addend of Eq. 1.6) yields a resonant and a nonresonant contribution depending on the intermediate state $|m\rangle$. A contribution to the DDSC results only if two or no photons are present in the intermediate state, since the first vector potential operator creates or annihilates only one photon.

a) The nonresonant term:
With two photons present in the intermediate state $|m\rangle = \left|c, \lambda_1 \vec{k}_1, \lambda_2 \vec{k}_2\right\rangle$ and thus $\epsilon_m = E_c + \hbar\omega_1 + \hbar\omega_2$ the emission process takes place before the absorption process. The respective transition probability is

$$w_{i \mapsto f} = \frac{2\pi}{\hbar} \left| \left(\frac{e\hbar}{mc}\right)^2 \sum_c \frac{\langle b| \sum_j \vec{A}_2 \cdot \vec{\nabla}_j |c\rangle \langle c| \sum_j \vec{A}_1 \cdot \vec{\nabla}_j |a\rangle}{E_c - E_a + \hbar\omega_2} \right|^2 \delta(E_b - E_a - \hbar\omega_1 + \hbar\omega_2). \tag{1.12}$$
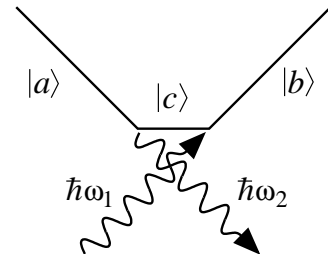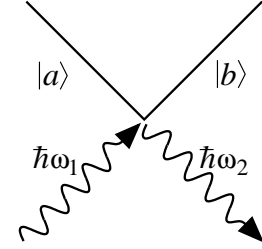
Since $|a\rangle$ is the ground state of the sample $E_c - E_a$ is always positive and the process can never be resonant. Thus, this term can be neglected in comparison to the nonresonant $\vec{A} \cdot \vec{A}$ term in first order.

b) The resonant term:

If no photon is present in the intermediate state $|m\rangle = |c, 0\rangle$ and thus $\epsilon_m = E_c$ the absorption process takes place before the emission process and with 1.7 the transition probability reads:

$$
\begin{aligned}
w_{i \mapsto f} &= \frac{2\pi}{\hbar} \frac{2\pi \hbar c^2}{V \omega_1} \frac{2\pi \hbar c^2}{V \omega_2} \left(\frac{e^2}{m^2 c^2} \right)^2 \\
&\times \left| \sum_c \frac{\langle b| \sum_j i\hbar e^{-i\vec{k}_2 \cdot \vec{r}_j} \, \hat{\varepsilon}_2^* \cdot \vec{\nabla}_j |c\rangle \langle c| \sum_j i\hbar e^{i\vec{k}_1 \cdot \vec{r}_j} \, \hat{\varepsilon}_1 \cdot \vec{\nabla}_j |a\rangle}{E_c - E_a - \hbar\omega_1 - i\Gamma_c/2} \right|^2 \\
&\times \delta(E_b - E_a - \hbar\omega_1 + \hbar\omega_2).
\end{aligned}
\tag{1.13}
$$

In contrast to the previous term this one becomes resonant if the energy of the incident photon $\hbar\omega_1$ equals the energy difference of the initial and any of all intermediate state of the sample. This is the case if the incident photon energy is close to the binding energy of an electron in the sample. The quantity $-i\Gamma_c/2$ is introduced to account for the finite lifetime of the intermediate state $|c\rangle$.

Thus, up to second order perturbation theory only two terms contribute to inelastic scattering processes: the $\vec{A} \cdot \vec{A}$ term in 1$^{\text{st}}$ order and the $\vec{A} \cdot \vec{\nabla}$ term in 2$^{\text{nd}}$ order perturbation theory. Since the number of photons in the incident beam is small compared to the interaction time, the probability to find the system in its ground state $|a\rangle$ is one ($p_a = 1$). Thus, the double differential scattering cross section (1.1) becomes:

$$
\begin{aligned}
\frac{d^2\sigma}{d\omega_2 \, d\Omega} &= \sum_{a,b} p_a \frac{V^2}{(2\pi)^3} \frac{\omega_2^2}{c^4} w_{a \to b} \\
&= \hbar \frac{\omega_2}{\omega_1} \frac{e^4}{c^4 m^2} \sum_b \left| (\hat{\varepsilon}_1 \cdot \hat{\varepsilon}_2^*) \langle b| \sum_j e^{i\vec{q} \cdot \vec{r}_j} |a\rangle \right. \\
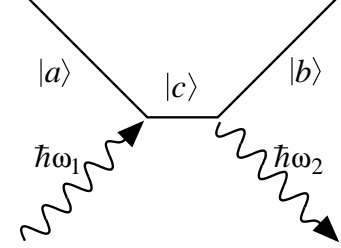&\quad + \left. \frac{1}{m} \sum_c \frac{\langle b| \sum_j i\hbar e^{-i\vec{k}_2 \cdot \vec{r}_j} \, \hat{\varepsilon}_2^* \cdot \vec{\nabla}_j |c\rangle \langle c| \sum_j i\hbar e^{i\vec{k}_1 \cdot \vec{r}_j} \, \hat{\varepsilon}_1 \cdot \vec{\nabla}_j |a\rangle}{E_c - E_a - \hbar\omega_1 - i\Gamma_c/2} \right|^2 \\
&\quad \times \delta(E_b - E_a - \hbar\omega_1 + \hbar\omega_2).
\end{aligned}
\tag{1.14}
$$

The first term is dominating the DDSC if the energy of the incident photon $\hbar\omega_1$ is far away from binding energies of the electrons of the sample. If on the other hand the energy of the incident photon is close to a binding energy of an electron of the sample then the denominator of the second term is close to zero and causes the DDSC to be dominated by the second term.

The first term describes nonresonant processes, generally referred to as inelastic x-ray scattering spectroscopy (IXSS). It is proportional to the dynamic structure factor

$S(\vec{q}, \omega)$ yielding information about the spatial and temporal correlation of the valence electrons of the sample. If the energy and momentum transfer to the system are small compared to characteristic energies and characteristic reciprocal distances of the electron system, respectively, then individual and collective excitations are probed, for example plasmons and electron-hole pair excitations [Schü91]. In case of large energy and momentum transfers to the system the impulse approximation can be applied leading to Compton scattering. Thereby information about the momentum density and the occupation function of the electronic ground state of the sample can be obtained [Coop85].

For the special case $|b\rangle = |a\rangle$ one gets elastic scattering. If $|b\rangle$ differs only slightly from $|a\rangle$, e.g. due to interacion with phonons, quasi-elastic (Rayleigh) scattering is present. In the case of a linearly polarized x-ray source the $\hat{\varepsilon}_1 \cdot \hat{\varepsilon}_2^*$ factor in Eq. 1.14 offers the opportunity to suppress the so called quasi-elastic line present in the resonant scattering spectra.

The second term of 1.14 describes the resonant inelastic x-ray scattering (RIXS). Due to the involvement of the electron binding energy $E_c - E_a$ in the DDSC, RIXS it is element selective. Moreover, since the momentum operator $\vec{p} = -i\hbar\vec{\nabla}$ and the polarization vector $\hat{\varepsilon}$ are present in both scattering operators, RIXS is sensitive to the angular momentum of the electronic states and depends on the polarization of the x-rays. This makes RIXS a powerful tool to investigate the electronic structure.

In addition, RIXS exhibits a law of Bloch $\vec{k}$-momentum conservation when valence electrons are probed. As a consequence, the shape of resonantly excited valence fluorescence spectra changes when either the incident energy or the momentum transfer is altered. This effect will be addressed in more detail in the following section.

1.2   The Resonant Inelastic Scattering Cross Section

So far no assumption has been made about how the electron system of the sample reacts to the transfer of energy and momentum. For resonant inelastic scattering one now assumes that only one electron interacts with a photon at a time, i.e. during the absorption of a photon one electron is excited from a bound state into a formerly unoccupied state above the Fermi energy, and during the emission of a photon one electron from the valence band refills the previously created core hole. Moreover, one assumes that the excitation and the deexcitation of an electron does not affect the other electrons of the sample via Coulomb interaction but that they remain 'frozen' in their states.

It is important to note that the frozen core approximation is only valid as long as the creation of holes in valence states is concerned. If a hole in the valence band is created the resulting change of the potential is uniform over the whole sample, due to the delocalization of valence states. Thus, the states of the other valence electrons are only marginally affected. If on the other hand a strongly bound core electron is removed from its shell, all electrons within the outer shells screen the core hole

thus changing their states. Accordingly, the calculated binding energy of the Cu 1s electrons for example is underestimated in the frozen core approximation by about 1.6%. Again the valence states remain nearly unaltered since the core hole is widely screened by the inner shell electrons as will be shown in Chapter 5.

Furthermore, due to the creation or the annihilation of a core hole the rearrangement of the electrons causes a sudden change of the atomic potential, leading to the possibility of double ionization excitations during the absorption or during the emission of a photon. The first kind of processes leads to the hypersatellites (see for example [Deut95, Diam00, Ster00] and Appendix C) whereas processes of the latter kind cause the radiative Auger satellites that will be described in Chapter 7.

By applying the frozen core approximation one can replace the many particle wave functions used so far by single particle wave functions. Thus, the sums over j vanish. Secondly, the states may be characterized by a single hole wave function instead of a product of electron wave functions. The necessary replacements are depicted in Figure 1.2. Namely $|a\rangle$, $|c\rangle$, and $|b\rangle$ are replaced by the conduction band state $|i\rangle$, the core state $|m\rangle$, and the valence state $|f\rangle$, respectively.
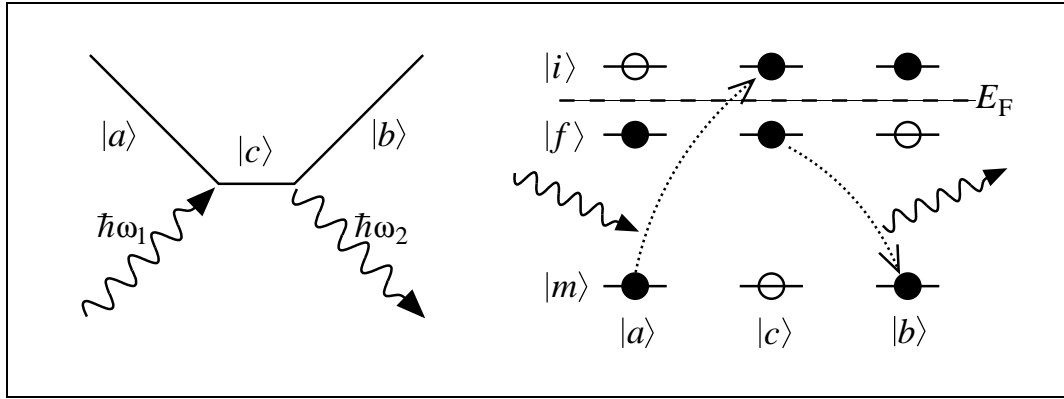
Figure 1.2: Many particle and single particle states of the sample.

Accordingly, the total electron energies E_a, E_c, and E_b are replaced by the single electron energies E_i, E_m, and E_f. Furthermore, the sum over the initial states i has to be reintroduced, since the hole state in the conduction band is not known a priori. Thus, the resonant part of the DDSC becomes:

$$\frac{d^2\sigma}{d\omega_2\, d\Omega} = \hbar\frac{\omega_2}{\omega_1}\left(\frac{e}{mc}\right)^4 \sum_{i,f}\left|\sum_m \frac{\langle f|\, i\hbar e^{-i\vec{k}_2\cdot\vec{r}}\, \hat{\varepsilon}_2\cdot\vec{\nabla}\, |m\rangle\, \langle m|\, i\hbar e^{i\vec{k}_1\cdot\vec{r}}\, \hat{\varepsilon}_1\cdot\vec{\nabla}\, |i\rangle}{E_m - E_i - \hbar\omega_1 - i\Gamma_m/2}\right|^2$$
$$\times\ \delta(E_f - E_i - \hbar\omega_1 + \hbar\omega_2). \tag{1.15}$$

For the derivation of the Bloch $\vec{k}$-conserving RIXS cross section further assumptions about the wave functions have to be made. The states in the conduction band and in the valence band of a conducting periodic crystal can be described by Bloch wave functions:

$$|i\rangle = |n_i\vec{k}_i\rangle = e^{i\vec{k}_i\cdot\vec{r}}\, u_{n_i\vec{k}_i}(\vec{r}) \quad \text{and} \quad |f\rangle = |n_f\vec{k}_f\rangle = e^{i\vec{k}_f\cdot\vec{r}}\, u_{n_f\vec{k}_f}(\vec{r}), \tag{1.16}$$

where n is the band index, $\vec{k}$ is the Bloch wave vector, and $u_{n,\vec{k}}$ is a lattice periodic function. In the original paper of Ma [Ma94] the core state $|m\rangle$ is described by a tight binding orbital $|m\rangle = \sum_{\vec{R}} e^{i\vec{k}_c \cdot \vec{R}} \psi_c(\vec{r} - \vec{R})$. Thus, the intermediate state $|m\rangle$ is characterized by the wave vector $\vec{k}_c$. A more striking Ansatz, suggested by Eisebitt [Eise00], will be used here:

$$|m\rangle = |n_j \vec{R}_j\rangle = \psi_{n_j}(\vec{r} - \vec{R}_j), \tag{1.17}$$

where ψ is an atomic wave function with core level index n_j centered at the atomic position $\vec{R}_j$. With this choice $|m\rangle$ is characterized by the atomic level of the core wave function and by the position of the atom at which the core hole is localized. Moreover the single particle hole states are replaced by the corresponding single particle electron states, noticing that a hole wave function is the complex conjugate of the corresponding electron wave function, and that the energy of a hole state is the negative of the corresponding electron state. Thus, the DDSC becomes

$$
\begin{aligned}
\frac{d^2\sigma}{d\omega_2\,d\Omega} \;=\; & \hbar\frac{\omega_2}{\omega_1}\left(\frac{e}{mc}\right)^4 \sum_{n_i\vec{k}_i}\sum_{n_f\vec{k}_f}\left|\sum_{n_j\vec{R}_j}\frac{M_2(n_f,\vec{k}_f,n_j,\vec{R}_j)M_1(n_i,\vec{k}_i,n_j,\vec{R}_j)}{E_{n_i\vec{k}_i} - E_{n_j\vec{R}_j} - \hbar\omega_1 - i\Gamma_{n_j\vec{R}_j}/2}\right|^2 \\
& \times\; \delta(E_{n_i\vec{k}_i} - E_{n_f\vec{k}_f} - \hbar\omega_1 + \hbar\omega_2), \tag{1.18}
\end{aligned}
$$

where

$$
\begin{aligned}
M_1(n_i,\vec{k}_i,n_j,\vec{R}_j) \;=\; & \langle e^{i\vec{k}_i\cdot\vec{r}}\,u_{n_i\vec{k}_i}(\vec{r})|i\hbar e^{i\vec{k}_1\cdot\vec{r}}\,\hat{\varepsilon}_1\cdot\vec{\nabla}|\psi_{n_j}(\vec{r}-\vec{R}_j)\rangle \qquad\text{and} \\
M_2(n_f,\vec{k}_f,n_j,\vec{R}_j) \;=\; & \langle\psi_{n_j}(\vec{r}-\vec{R}_j)|i\hbar e^{-i\vec{k}_2\cdot\vec{r}}\,\hat{\varepsilon}_2^*\cdot\vec{\nabla}|e^{i\vec{k}_f\cdot\vec{r}}\,u_{n_f\vec{k}_f}(\vec{r})\rangle \tag{1.19}
\end{aligned}
$$

are the transition matrix elements. Those can be evaluated by (i) substituting $\vec{r} - \vec{R}_j = \vec{r}\,'$, (ii) making use of the lattice periodicitiy of $u(\vec{r})$, and (iii) by assuming that the spatial extent of the core wave function is small compared to the lattice spacing and thus $e^{-i\vec{k}_i\cdot\vec{r}\,'} \approx 1$ and $e^{i\vec{k}_f\cdot\vec{r}\,'} \approx 1$:

$$
\begin{aligned}
M_1(n_i,\vec{k}_i,n_j,\vec{R}_j) \;=\; & \int d\vec{r}\; e^{-i\vec{k}_i\cdot\vec{r}}\,u_{n_i\vec{k}_i}(\vec{r})\;i\hbar e^{i\vec{k}_1\cdot\vec{r}}\,\hat{\varepsilon}_1\cdot\vec{\nabla}\,\psi_{n_j}(\vec{r}-\vec{R}_j) \\
\stackrel{(i)}{=}\; & \int d\vec{r}\,'\; e^{-i\vec{k}_i\cdot(\vec{r}\,'+\vec{R}_j)}\,u_{n_i\vec{k}_i}(\vec{r}\,'+\vec{R}_j)\;i\hbar e^{i\vec{k}_1\cdot(\vec{r}\,'+\vec{R}_j)}\,\hat{\varepsilon}_1\cdot\vec{\nabla}\,\psi_{n_j}(\vec{r}\,') \\
\stackrel{(ii)}{=}\; & e^{-i\vec{k}_i\cdot\vec{R}_j}\,e^{i\vec{k}_1\cdot\vec{R}_j}\int d\vec{r}\,'\; e^{-i\vec{k}_i\cdot\vec{r}\,'}\,u_{n_i\vec{k}_i}(\vec{r}\,')\;i\hbar e^{i\vec{k}_1\cdot\vec{r}\,'}\,\hat{\varepsilon}_1\cdot\vec{\nabla}\,\psi_{n_j}(\vec{r}\,') \\
\stackrel{(iii)}{=}\; & e^{-i\vec{k}_i\cdot\vec{R}_j}\,e^{i\vec{k}_1\cdot\vec{R}_j}\underbrace{\int d\vec{r}\,'\; u_{n_i\vec{k}_i}(\vec{r}\,')\;i\hbar e^{i\vec{k}_1\cdot\vec{r}\,'}\,\hat{\varepsilon}_1\cdot\vec{\nabla}\,\psi_{n_j}(\vec{r}\,')}_{M_1'(n_i,\vec{k}_i,n_j)}, \tag{1.20}
\end{aligned}
$$

$$
M_2(n_f,\vec{k}_f,n_j,\vec{R}_j) \;=\; e^{-i\vec{k}_2\cdot\vec{R}_j}\,e^{i\vec{k}_f\cdot\vec{R}_j}\underbrace{\int d\vec{r}\,'\; \psi_{n_j}(\vec{r}\,')\;i\hbar e^{-i\vec{k}_2\cdot\vec{r}\,'}\,\hat{\varepsilon}_2\cdot\vec{\nabla}\,u_{n_f\vec{k}_f}(\vec{r}\,')}_{M_2'(n_f,\vec{k}_f,n_j)}. \tag{1.21}
$$

Hence, the matrix elements M_1' and M_2' are independent of $\vec{R}_j$. Stating that the energy and the lifetime of a core hole are independent of the position of the atom,

one finds that $E_{n_j,R_j} = E_{n_j}$ and $\Gamma_{n_j,R_j} = \Gamma_{n_j}$ and the sum over the intermediate states can be carried out at once:

$$\sum_{\vec{R}_j} e^{i\vec{k}_1\cdot\vec{R}_j}\, e^{-i\vec{k}_2\cdot\vec{R}_j}\, e^{-i\vec{k}_i\cdot\vec{R}_j}\, e^{i\vec{k}_f\cdot\vec{R}_j} \;=\; \sum_{\vec{R}_j} e^{i(\vec{k}_1-\vec{k}_2-\vec{k}_i+\vec{k}_f)\cdot\vec{R}_j} = \delta_{\vec{G},(\vec{k}_1-\vec{k}_2-\vec{k}_i+\vec{k}_f)}, \quad (1.22)$$

$\vec{G}$ being any reciprocal lattice vector. Thus, the DDSC reads

$$
\begin{aligned}
\frac{d^2\sigma}{d\omega_2\,d\Omega} \;=\;& \hbar\frac{\omega_2}{\omega_1}\left(\frac{e}{mc}\right)^4 \sum_{n_i\vec{k}_i}\sum_{n_f\vec{k}_f}\left| \delta_{\vec{G},(\vec{k}_1-\vec{k}_2-\vec{k}_i+\vec{k}_f)} \sum_{n_j} \frac{M_2'(n_f,\vec{k}_f,n_j)M_1'(n_i,\vec{k}_i,n_j)}{E_{n_i\vec{k}_i}-E_{n_j}-\hbar\omega_1-i\Gamma_{n_j}/2} \right|^2 \\
&\times\; \delta(E_{n_i\vec{k}_i}-E_{n_f\vec{k}_f}-\hbar\omega_1+\hbar\omega_2).
\end{aligned}
\quad (1.23)
$$

Moreover, the denominator constitutes a Lorentzian which converts into a δ-function in the case of $\Gamma_{n_j}\Rightarrow 0$:

$$\lim_{y\to 0}\left|\frac{1}{x-iy}\right|^2 \;=\; \lim_{y\to 0}\frac{1}{x^2+y^2} \;=\; \lim_{y\to 0}\mathrm{Lor}(x,y) \;=\; 2\pi\delta(x). \quad (1.24)$$

For the time being, one may assume that the lifetime of the intermediate state is infinite giving rise to: $\delta(E_{n_i\vec{k}_i}-E_{n_j}-\hbar\omega_1)$. Using this δ-function to remove $E_{n_i\vec{k}_i}$ and $\hbar\omega_1$ from the total energy conservation $\delta(E_{n_i\vec{k}_i}-E_{n_f\vec{k}_f}-\hbar\omega_1+\hbar\omega_2)$ one ends up with

$$
\begin{aligned}
\frac{d^2\sigma}{d\omega_2\,d\Omega} \;=\;& \hbar\frac{\omega_2}{\omega_1}\left(\frac{e}{mc}\right)^4 \sum_{n_i\vec{k}_i}\sum_{n_f\vec{k}_f}\sum_{n_j}\left| M_1'(n_i,\vec{k}_i,n_j)\right|^2 \delta(E_{n_i\vec{k}_i}-E_{n_j}-\hbar\omega_1) \\
&\times\; \delta_{\vec{G},(\vec{k}_1-\vec{k}_2-\vec{k}_i+\vec{k}_f)}\;\left| M_2'(n_f,\vec{k}_f,n_j)\right|^2 \delta(E_{n_f\vec{k}_f}-E_{n_j}-\hbar\omega_2).
\end{aligned}
\quad (1.25)
$$

This formula will be discussed in the following. The first matrix element and first δ-function together with the sum over the initial states $n_i\vec{k}_i$ describes the absorption part of the scattering process, in analogy to the absorption probability in formula 1.8. Likewise the second matrix element, the second δ-function, and the sum over $n_f\vec{k}_f$ describe the emission part of the scattering process.

The sum over all unoccupied states $n_i\vec{k}_i$ together with the δ-function $\delta(E_{n_i\vec{k}_i}-E_{n_j}-\hbar\omega_1)$ gives rise to the unoccupied density of states (DOS) thus containing the crystal properties of the sample whereas the matrix element $\left|M_1'(n_i,\vec{k}_i,n_j)\right|^2$ reflects the atomic part of the transition probability, namely the overlap between the core wave function $\psi_{n_j}(\vec{r}\,')$ and the valence wave function $u_{n_i\vec{k}_i}(\vec{r}\,')$ mediated by the scattering operator $i\hbar e^{-i\vec{k}_1\cdot\vec{r}\,'}\,\hat\varepsilon_1\cdot\vec\nabla$. Since $\psi_{n_j}(\vec{r}\,')$ is strongly localized, only the part of $u_{n_f\vec{k}_i}(\vec{r}\,')$ localized at the same atom contributes to the matrix element, making the absorption process element specific. The same considerations apply to the emission part of the scattering process. Therefore, RIXS an element specific technique.

In the matrix elements M_1' and M_2' the exponential of the scattering operator may be expanded into its Tailor series giving rise to the series of multipole operators imposing the respective selection rules and angular dependencies from the polarization of

the photon, thereby making RIXS selective to orbital and magnetic quantum numbers. For the time being only the term $e^{-i\vec{k}_2 \cdot \vec{r'}} \approx 1$, being of zeroth order in $\vec{k}_2 \cdot \vec{r'}$, will be kept, leading to the dipole approximation. Contributions from quadrupolar transitions will be discussed in the Chapters 3 and 6.

If absorption and emission of the photon are treated as two independent consecutive processes, i.e. one uses the $\vec{A} \cdot \vec{\nabla}$ term in 1$^{\text{st}}$ order for both the absorption and the emission process and calculates the product of both, one gets the same cross section except for the Kronecker-δ which interconnects the two parts into one single scattering process. The consequence of the Kronecker-δ is the conservation of the Bloch $\vec{k}$-momentum: The difference of the wave vectors of the incoming and the outgoing photon (i.e. the momentum transfer $\vec{q}$) has to equal the difference of the Bloch $\vec{k}$-momenta of the conduction and the valence electron involved in the process modulo any reciprocal lattice vector.

1.3   Bloch $\vec{k}$-Momentum Conservation

The influence of the Bloch $\vec{k}$-momentum conservation on the line shape of valence fluorescence spectra may be explained by the example of RIXS at the Ni K edge in NiAl. The states relevant in the scattering process are depicted in Fig. 1.3. It shows the electronic band stucture of NiAl in the vicinity of the Fermi energy E_{F} along the high symmetry directions of the Brillouin zone[1]. The diameter of the circles is proportional to the fraction of Ni 4p orbitals contributing to the respective state. Also shown is the Ni 1s state at 8333.0 eV below E_{F} from which an electron is excited into the conduction band after the absorption of a photon with energy $\hbar\omega_1$. The first δ-function in Eq.1.25 determines the energy of the states in the conduction band the core electron can be excited into.

Due to the band structure not the whole Brillouin zone but only $\vec{k}$-points on the respective isoenergetic surface can contribute to the absorption process. In Fig. 1.3 the incident energy is chosen to be 2 eV above the K-absorption threshold, marked by the horizontal bar. At this energy only a limited number of $\vec{k}$-points allowed states exist. Additionally within the dipole approximation the first matrix element requires the conduction band state to have Ni p-character. In the above example the strongest Ni p-character is present around the R point of the Brillouin zone. Thus, in the sum over $n_i \vec{k}_i$ predominantly states with $\vec{k}_i$ in the vicinity of the R point remain.

Now the Kronecker-δ, conserving the Bloch $\vec{k}$-momentum of the process, comes into play. Since $\vec{k}_1 - \vec{k}_2 = \vec{q}$ is determined by the scattering angle and since $\vec{k}_i$ is selected by $\hbar\omega_1$ via the band structure as described above, $\delta_{\vec{G}, \vec{k}_1 - \vec{k}_2 + \vec{k}_i - \vec{k}_f}$ together with the sum over $\vec{k}_f$ selects specific $\vec{k}_f$, in this example at a point between Γ and M, marked by a vertical bar in Fig. 1.3. Thus, only electrons with a Bloch $\vec{k}$-vector equal to $\vec{k}_f$

---

[1]One has to keep in mind that the x-axis of Fig. 1.3 describes a zigzag path through the Brillouin zone and that thus distances on the x-axis are generally *not* proportional to the distances in 3D-space

Figure 1.3: RIXS at the K edge of Ni in NiAl. The diameter of the circles is proportional to the fraction of Ni 4p character of the electron states.
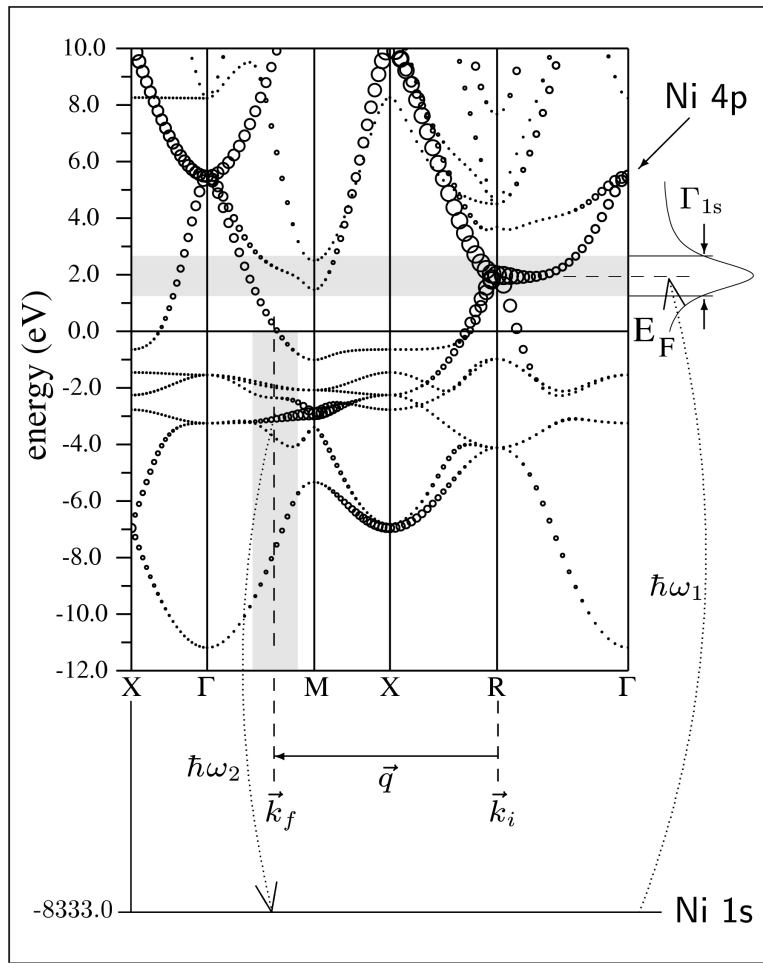
can refill the core hole, thereby emitting a photon with an energy determined by the second δ-function. Again the matrix element requires the emitting orbitals to be of Ni p-character. In our example one would expect to see a strong emission line at -3 eV and two smaller lines at -0 and -8 eV below the Fermi energy.

Thus, not the whole Brillouin zone contributes to the emission spectrum but only a restricted number of $\vec{k}$-points, that are selected by $\hbar\omega_1$ and by the momentum transfer $\vec{q}$ via the band structure. If one changes the energy of the incoming photon, then a different set of $\vec{k}_i$ is selected, thereby also selecting a new set of allowed $\vec{k}_f$, even if the momentum transfer $\vec{q}$ is kept constant. If on the other hand the energy of the incoming photon is kept constant, the selected $\vec{k}_i$ remain the same, but by changing the scattering angle and thus changing the momentum transfer $\vec{q}$ the allowed values of $\vec{k}_f$ are changed as well. As a result the shape of the resonantly excited valence fluorescence line strongly depends on both the energy of the incoming photon and on the momentum transfer.

This is one of the advantages offered by the use of hard x-rays. In the case of soft x-rays, where $|\vec{k}_1|$ and $|\vec{k}_2|$ are much smaller than the dimensions of the first Brillouin zone, the $\vec{k}$-momentum conservation reduces to $\vec{k}_i = \vec{k}_f$. Thus, the RIXS spectra obtained by the use of soft x-ray are idependent of the scattering angle and depend solely on the incident energy. In contrast, Bloch $\vec{k}$-selective RIXS using hard x-rays

via the length and the direction of $\vec{q}$ with respect to the crystal axes of the sample introduces additional degrees of freedom.

In short: the Bloch $\vec{k}$-conservation in the RIXS process leads to valence RIXS spectra that are selective to the Bloch $\vec{k}$-momentum.

However, there are some restrictions to the picture drawn above. Firstly the intermediate state has a limited lifetime, thus $\Gamma_{1s} \neq 0$. Therefore the first δ-function has to be replaced by a Lorentzian leading to excitations into a broader energy region around the incident energy. Thereby the number of $\vec{k}$-points accessible in the absorption process is enlarged. Similarly in the emission process the second δ-function has to be modified leading to a broadening of the fluorescence line. Secondly the momentum transfer $\vec{q}$ is not infinite sharp defined in the experiment resulting in a further increase of the number of $\vec{k}$-points contributing to the emission process. Finally the energy resolution of both the monochromator and the analyzer has to be accounted for.

Nevertheless, it is possible to obtain Bloch $\vec{k}$-selective spectra from a large variety of samples. Moreover, in many cases it is possible to perform a kind of band tracing, i.e. the dispersion of certain features in the RIXS spectra can be directly assigned to the dispersion of certain bands in the electronic band structure.

Chapter 2

Band Structure Calculation using the LAPW Algorithm

In order to compare measured Bloch $\vec{k}$-selective fluorescence spectra to calculated ones, the electronic band structure of the sample has to be obtained. Among the numerous methods available, the density functional theory (DFT) has proven successful for the description of both molecules and crystals.

An extensive description of the linearized augmented plane waves (LAPW) method can be found in the book by David J. Singh [Sing94].

2.1 Density Functional Theory and Kohn-Sham Equations

Condensed matter consists of a system of electrons that interact with the atomic nuclei and with each other. The calculation of the electronic structure therefore results in a many particle problem whose Schrödinger equation cannot be solved analytically. Thus, one needs to find approximations to the general problem. An elegant solution is based on the theorem of Hohenberg and Kohn [Hohe64]:

> *The total energy of a system of interacting electrons in an external potential is a functional of the electron density. The total energy is minimized by the electron density of the electronic ground state.*

The functional $E_{\text{tot}} = E_{\text{tot}}[\rho]$ generally is of the form

$$E_{\text{tot}}[\rho] = T_{\text{e}}[\rho] + T_{\text{i}}[\rho] + E_{\text{ee}}[\rho] + E_{\text{ii}}[\rho] + E_{\text{ei}}[\rho], \qquad (2.1)$$

where $T_{\text{e}}[\rho]$ and $T_{\text{i}}[\rho]$ are the kinetic energies of the electrons and of the nuclei, whereas $E_{\text{ee}}[\rho]$, $E_{\text{ii}}[\rho]$, and $E_{\text{ei}}[\rho]$ describe the electron-electron, the nucleus-nucleus, and the electron-nucleus interactions, respectively.

Often the adiabatic approximation is applied. Since the nuclei are much heavier than the electrons, the latter follow the slow movements of the nuclei in a quasi-static manner. Thus, the electron system remains is its ground state even if the nuclei

oscillate around their equilibrium positions. Therefore T_i and E_ii can be omitted if one is interested in electronic properties only.

However, the functional describing the electron-electron interactions is unknown in general and is subject to approximation. Usually E_ei is split up into the local part of the Coulomb interaction giving rise to the Hartree total energy of the electron-electron interaction E_H and into the exchange-correlation functional E_xc which contains the non-local many particle part of the the electron-electron interaction. This yields:

$$E_\mathrm{tot}[\rho] = T[\rho] + E_\mathrm{ei}[\rho] + E_\mathrm{H}[\rho] + E_\mathrm{xc}[\rho] \tag{2.2}$$

with the energy functionals:

$T\,[\rho]$ the kinetic energy of the electrons,
$E_\mathrm{ei}\,[\rho]$ the potential energy of the electrons in the potential of the nuclei,
$E_\mathrm{H}\,[\rho]$ the Coulomb part of the electron electron interaction, and
$E_\mathrm{xc}\,[\rho]$ the exchange correlation energy of the electrons.

A direct minimization yielding the electron density ρ of the ground state is not feasible since the number of parameters needed to properly describe the electron density is much too large. Indeed from 2.2 the Kohn-Sham equations can be derived [Kohn65],

$$(T + V_\mathrm{ei}(\vec{r}) + V_\mathrm{H}(\vec{r}) + V_\mathrm{xc}(\vec{r}))\ \varphi_i(\vec{r}) = \varepsilon_i\ \varphi_i(\vec{r}), \tag{2.3}$$

where the Kohn-Sham orbitals $\varphi_i(\vec{r})$ are single particle like wave functions. The electron density then is given by the sum over the squares of all occupied Kohn-Sham orbitals:

$$\rho(\vec{r}) = \sum_\mathrm{occ} \varphi_i^*(\vec{r})\varphi_i(\vec{r}). \tag{2.4}$$

As in Eq. 2.2 the potentials depend on the electron density:

$$V_\mathrm{H}(\vec{r}) = e^2 \int d^3r' \frac{\rho(\vec{r}\,')}{|\vec{r} - \vec{r}\,'|} \qquad \text{and} \qquad V_\mathrm{xc}(\vec{r}) = \frac{\delta E_\mathrm{xc}[\rho]}{\delta \rho(\vec{r})}. \tag{2.5}$$

Again, the exchange-correlation energy $E_\mathrm{xc}[\rho]$ contains the non-local part of the electron-electron interaction. It may be calculated within the local density approximation (LDA)

$$E_\mathrm{xc}[\rho] = \int d\vec{r}\, \rho(\vec{r})\, \varepsilon_\mathrm{xc}(\rho(\vec{r})), \tag{2.6}$$

where $\varepsilon_\mathrm{xc}\,(\rho(\vec{r}))$ is the exchange-correlation energy per electron of the homogeneous electron gas, which can be calculated exactly. Thus, the non-local exchange-correlation of the inhomogeneous system is expressed in terms of its density $\rho(\vec{r})$ and the exchange-correlation of the homogeneous electron gas ε_xc corresponding to the

local density of the actual system. Although succesfull in many cases, the LDA can be improved by considering not only the local density but also its gradient, giving rise to the generalized gradient approximation (GGA), see e.g. [Perd92, Perd96]. By means of these approaches, the non-local exchange-correlation functional is replaced by a local potential, being a prerequisit for the applicability of the density functional theory.

The advantage of the Kohn-Sham equations over the equation of Hohenberg and Kohn is the fact that the many particel problem is reduced to the solution of a series of single particle Schrödinger equations that are only coupled via the total potential $V = V_{\text{ei}} + V_{\text{H}} + V_{\text{xc}}$. Consequently these equations must be solved self-consistently:

One chooses a certain set of wave functions $\varphi_i^{(1)}(\vec{r})$ having eigenvalues $\varepsilon_i^{(1)}$ and calculates the respective electron density $\rho^{(1)}(\vec{r})$. Thereof one determines the total potential $V^{(1)}(\vec{r})$, solves the Kohn-Sham equations and thus finds new eigenvalues $\varepsilon_i^{(2)}$ and wave functions $\varphi_i^{(2)}(\vec{r})$. From these again a charge density $\rho^{(2)}(\vec{r})$ can be otained. This cycle is performed until the electron density has converged to a stable distribution.

In the case of a crystalline substance the Bloch theorem gives rise to further simplifications. Like the wave function also the charge distribution, the potential and thus the whole Hamiltionian have lattice periodicity and symmetry. Thus, for the calculation of bulk properties it is sufficient to obtain the solution of the Kohn-Sham equation on a grid of $\vec{k}$-points in the irreducible wedge of the Brillouin zone, thereby reducing the computational effort significantly.

2.2   The Kohn-Sham Orbitals

Although the direct numerical solution of the Kohn-Sham equations is in principle possible, the Kohn-Sham orbitals are mostly expanded into a basis $\phi_\alpha(\vec{r})$,

$$\varphi_i(\vec{r}) = \sum_\alpha c_{i\alpha}\phi_\alpha(\vec{r}), \tag{2.7}$$

thereby introducing the expansion coefficients $c_{i\alpha}$ that are now the only variables to be determined self-consistently. Then the solution of the Kohn-Sham equations reduces to an eigenwert problem. In order to do so, the expanded Kohn-Sham orbitals 2.7 are inserted into the Kohn-Sham equation 2.3. The resulting eigenwert equation is multiplied from left by the basis and the integration over the unit cell is performed on both sides. The integrals are the elements of the matrices $\mathcal{H}_{\alpha\alpha'}$ and $\mathcal{S}_{\alpha\alpha'}$. The expansion coefficients $c_{i\alpha}$ are the components of the eigenvectors c_i corresponding to the eigenvalues ε_i.

$$\mathcal{H}\varphi_i(\vec{r}) = \varepsilon_i\varphi_i(\vec{r}) \tag{2.8}$$

$$\sum_\alpha c_{i\alpha}\mathcal{H}\phi_\alpha(\vec{r}) = \varepsilon_i\sum_\alpha c_{i\alpha}\phi_\alpha(\vec{r}) \tag{2.9}$$

$$\sum_{\alpha\alpha'} \underbrace{\int \phi_{\alpha'}^*(\vec{r}) \mathcal{H} \phi_\alpha(\vec{r}) d^3r}_{\mathcal{H}_{\alpha\alpha'}} \; c_{i\alpha} \;=\; \varepsilon_i \sum_{\alpha\alpha'} \underbrace{\int \phi_{\alpha'}^*(\vec{r}) \phi_\alpha(\vec{r}) d^3r}_{\mathcal{S}_{\alpha\alpha'}} \; c_{i\alpha} \qquad (2.10)$$

$$(\mathcal{H}_{\alpha\alpha'} - \varepsilon_i \mathcal{S}_{\alpha\alpha'}) c_{i\alpha} \;=\; 0 \qquad (2.11)$$

The resulting eigenwert problem can be solved efficiently by well established matrix algorithms.

However, the basis functions $\phi_\alpha(\vec{r})$ are in general not eigenfunctions of the Hamiltonian $\mathcal{H}$ and therefore the Hamilton matrix $\mathcal{H}_{\alpha\alpha'}$ is not diagonal in general. Although the basis $\phi_\alpha(\vec{r})$ is complete it is not necessarily orthonormal. Therefore the overlap matrix $\mathcal{S}_{\alpha\alpha'}$ usually is not the unit matrix.

As an example the Kohn-Sham orbitals are expanded into plane waves:

$$\phi_\alpha(\vec{r}) = \phi_{\vec{G},\vec{k}}(\vec{r}) = e^{i(\vec{k}+\vec{G})\cdot\vec{r}}. \qquad (2.12)$$

Here the $\vec{k}$ are Bloch wave vectors from within the irreducible wedge of the first Brillouin zone and the $\vec{G}$ are the reciprocal lattice vectors. Practically the expansion has to be truncated at $\vec{G} = \vec{G}_{\max}$ resulting in a set of n reciprocal lattice vectors. At a given point $\vec{k}$ in reciprocal space the basis consists of n plane waves. Accordingly the matrices $\mathcal{H}$ and $\mathcal{S}$ have $n \times n$ components giving rise to n eigenvalues $\varepsilon_{i,\vec{k}}$ and n eigenvectors $c_{i,\vec{k}}$ with n components $c_{i,\vec{k},\vec{G}}$.

2.3   The Choice of the Basis Functions

The choice of the basis functions $\phi_\alpha(\vec{r})$ strongly influences the performance of the algorithm. The better the basis is matching the actual Kohn-Sham orbitals, the faster the charge density will converge. In addition, the algorithm is less sensitive to possible restrictions of the flexibility of the basis, if the Kohn-Sham orbital are well suited to the problem. Moreover, the basis should enable a fast calculation of the matrix elements $\mathcal{H}_{\alpha\alpha'}$ and $\mathcal{S}_{\alpha\alpha'}$.

In a solid the wave functions of the electrons in the vicinity of the atomic nuclei, where the potential strongly varies, are similar to atomic wave functions, whereas between the atomic nuclei, where the potential is nearly constant, the electron wave functions are similar to plane waves.

2.3.1   Plane Waves

If plane waves are used as a basis, a large number of expansion coefficients has to be taken into acount in order to adequately describe the short range oscillations of the wave functions in the vicinity of the nuclei. This leads to large matrices whose inversion is rather time consuming and sometimes is outnumbering the advantage of the fast calculation of the matrix elements due to the orthogonality of the basis. To overcome this difficulty, two different strategies can be used.

2.3.2 Pseudopotentials

In pseudopotential methods the states corresponding to localized electrons are excluded from the calculation. Their influence on the valence electrons is only accounted for by the screening of the potential of the atomic nuclei. Thus, the strongly varying atomic potential is replaced by a smooth pseudopotential. Within this potential the valence electrons can be considered to move like nearly free electrons, which can be properly described by a small set of plane waves. The disadvantage of this method is the extensive calculation of the pseudopotential which in contrast to the total potential $V(\vec{r})$ is not local but depends on $\vec{k}$.

2.3.3 APW Methods

The second possibility is based on a dual representation of the basis functions. The direct space is divided into spheres centered at the atomic positions and into the interstitial space in between the atomic spheres. Within the interstitial region the basis consists of plane waves, whereas within the atomic spheres the wave functions are represented by atomic orbitals. Thus, in each region the basis is well suited to represent the behaviour of the single electron wave functions in the Kohn-Sham equation. Since the Kohn-Sham orbitals have to be continuous, the plane waves are augmented at the sphere boundary by a linear combination of atomic orbitals. Thus, this method is named *Augmented Plane Waves* (APW).

The basis functions are defined as follows:

$$\phi_{\vec{k},\vec{G}}(\vec{r}) = \begin{cases} \frac{1}{\sqrt{\Omega}} e^{i(\vec{k}+\vec{G})\cdot\vec{r}} & \vec{r} \in \mathbf{Interstitial} \\ \sum_{lm} a_{\vec{k}\vec{G}lm} u_l(r) Y_{lm}(\hat{r}) & \vec{r} \in \mathbf{Spheres}. \end{cases} \quad (2.13)$$

Therein $Y_{lm}(\hat{r})$ are the spherical harmonics and the $u_l(r)$ denote the solutions of the radial part of the Schrödinger equation:

$$\left(-\frac{d^2}{dr^2} + \frac{l(l+1)}{r^2} + V(r) - E_l \right) r\, u_l(r) = 0. \quad (2.14)$$

where E_l is an energy parameter and where $V(r)$ is the spherical component of the total potential within the atomic sphere. The coefficients $a_{\vec{k}\vec{G}lm}$ are determined from the continuity condition at the sphere boundary.

In analogy, the potential V and the electron density ρ are expanded:

$$V(\vec{r}) = \begin{cases} \frac{1}{\sqrt{\Omega}} \sum_{\vec{G}} V_{\vec{G}} e^{i\vec{G}\cdot\vec{r}} & \vec{r} \in \mathbf{Interstitial} \\ \sum_{lm} V_{lm}(r) Y_{lm}(\hat{r}) & \vec{r} \in \mathbf{Spheres}. \end{cases} \quad (2.15)$$

$$\rho(\vec{r}) = \begin{cases} \frac{1}{\sqrt{\Omega}} \sum_{\vec{G}} \rho_{\vec{G}} e^{i\vec{G}\cdot\vec{r}} & \vec{r} \in \mathbf{Interstitial} \\ \sum_{lm} \rho_{lm}(r) Y_{lm}(\hat{r}) & \vec{r} \in \mathbf{Spheres}. \end{cases} \quad (2.16)$$

The muffin-tin approximation, where only coefficients with $l = 0$, $m = 0$, and $\vec{G} = 0$ are taken into account, restrics the potential to be spherical within the atomic

spheres and to be constant within the interstitial region. Calculations making use of further components are called full potential calculations.

A major drawback of the APW method is that the solution of the radial Schrödinger equation depends on the energy parameter E_l. As a consequence the augmented plane waves are only in those cases solutions of the Kohn-Sham equation where the respective energy eigenvalue ε equals the energy parameter E_l. Thus, the APWs have no variational freedom to follow the shift of band energies if the energy parameters are kept fixed throughout the self-consistence circle. Therefore, after each digonalization of the Hamilton matrix, the energy parameter for each band must be varied until it equals its respective energy eigenvalue. This procedure can be rather time consuming.

2.3.4 LAPW Method

To overcome the described limitation of the APW method Koelling and Arbman [Koel75] performed a Taylor expansion of the radial wave function $u_l(r)$ with respect to the energy parameter E_l:

$$u_l(\varepsilon, r) = u_l(E_l, r) + (\varepsilon - E_l)\, \dot{u}_l(E_l, r) + O\left((\varepsilon - E_l)^2\right), \tag{2.17}$$

where $\dot{u}_l(E_l, r)$ denotes the partial derivative of the radial function with respect to the energy parameter evaluated at $E = E_l$:

$$\dot{u}_l(E_l, r) = \left.\frac{\partial u_l}{\partial E}\right|_{E=E_l}. \tag{2.18}$$

The consideration of the first derivative of the radial wave function with respect to the energy parameter leads to the linearization of the APWs with respect to the energy. Therefore these basis functions are called *Linearized Augmented Plane Waves* (LAPW). Within this basis the Kohn-Sham orbitals are solutions of the Kohn-Sham equation in those cases where the energy parameter E_l differs from the respective band energy ε. Thereby the flexibility of the basis is increased to such an extent that in principle one single E_l can be used for all valence states.

Thus, the LAPW basis is defined as

$$\phi_{\vec{k},\vec{G}}(\vec{r}) = \begin{cases} \frac{1}{\sqrt{\Omega}} e^{i(\vec{k}+\vec{G})\cdot\vec{r}} & \vec{r} \in \textbf{I}\text{nterstitial} \\ \sum_{lm}\left(a_{\vec{k}\vec{G}lm}u_l(r) + b_{\vec{k}\vec{G}lm}\dot{u}_l(r)\right)Y_{lm}(\hat{r}) & \vec{r} \in \textbf{S}\text{pheres,} \end{cases} \tag{2.19}$$

where the matching coefficients $a_{\vec{k}\vec{G}lm}$ and $b_{\vec{k}\vec{G}lm}$ are determined to ensure the continuity of both the LAPW orbital $\phi_{\vec{k},\vec{G}}(\vec{r})$ and its first derivative at the sphere boundary. The radial wave functions and their energy derivatives are obtained from

$$\left(-\frac{d^2}{dr^2} + \frac{l(l+1)}{r^2} + V(r) - E_l\right) r\, u_l(r) \;\; = \;\; 0 \tag{2.20}$$

with the condition $\lim_{r\to 0} r\dot{u}_l(r) = 0$ and by

$$\left(-\frac{d^2}{dr^2} + \frac{l(l+1)}{r^2} + V(r) - E_l\right) r\, \dot{u}_l(r) \;\; = \;\; r\, u_l(r). \tag{2.21}$$

Moreover, the orthonormalization conditions

$$\int_0^{R_{\mathrm{MT}}} (r\,u_l(r))^2 \; dr = 1 \qquad\qquad \int_0^{R_{\mathrm{MT}}} r^2 u_l(r)\dot{u}_l(r) \; dr = 0 \qquad (2.22)$$

are imposed, where R_{MT} is the muffin-tin radius, i.e. the radius of the atomic sphere. Due to the above mentioned orthonormalization the matrices $\mathcal{H}$ and $\mathcal{S}$ can easily be calculated from the coefficients $c_{i,\vec{k}\vec{G}}$, $a_{\vec{k}\vec{G}lm}$ and $b_{\vec{k}\vec{G}lm}$.

Furthermore, summation over $\vec{G}$ at a certain $\vec{k}$ for a given combination of l and m yields the partial charge $Q_{l,m}(\vec{k},i)$, representing the contribution of the atomic orbital with quantum numbers l and m to the Kohn-Sham orbital with wave vector $\vec{k}$ and band index i. Thus, the partial charges contain information about the hybridization of states. Similarly the partial densities of states $\mathrm{DOS}_{l,m}$ are obtained by summation over $\vec{k}$ and $\vec{G}$ with l and m kept fixed.

In principle it is possible to treat all electronic states in a solid as LAPWs. However, such expenses are not necessary for the core electrons. Since these are strictly confined within the atomic spheres they do not interact with the neighbouring atoms and thus are not subject to hybridization. Instead, the core states can be treated within an purely atomic calculation. In the case of the WIEN97 package the core states are obtained from a relativistic calculation considering only the spherical part of the current total potential. Especially in the case of high Z materials this distinction between core and valence states reduces the effort significantly. The energy separating core and valence states has to be choosen in such a way that the core orbitals are strictly confined to within the atomic spheres to ensure their orthogonalization with respect to the valence states.

Another important modification to the picture drawn in the preceeding sections is the mixing of the charge density. If the new density $\rho^{(2)}$, obtained from the starting density $\rho^{(1)}$ in the first iteration cycle, is directly used as the input for the second iteration step, the charge will not converge, but will oscillate between two different charge distributions. Therefore, only a small fraction of the new density $\rho_{\mathrm{out}}^{(j)}$ is admixed to the old density $\rho_{\mathrm{in}}^{(j)}$:

$$\rho_{\mathrm{in}}^{(j+1)} = (1-\alpha)\rho_{\mathrm{in}}^{(j)} + \alpha\rho_{\mathrm{out}}^{(j)} \qquad (2.23)$$

If the mixing parameter α is sufficiently small the charge density converges. In the case of simple metal convergence can be reached for $\alpha \approx 0.1$. This type of mixing is named Pratt or direct mixing. However, often different components of the charge exhibit different convergence behaviour. Thus, it can be difficult to find the best choice of α. Therefore, more sophisticated mixing schemes have been constructed. The most common of these is the Broyden mixing scheme [Broy65], where the mixing parameter is determined individually for each parameter of the charge density. If a certain density parameter exhibits an oscillatory behaviour its mixing parameter is set to a smaller value than for a well converging density component.

Chapter 3

Bloch $\vec{k}$-Selective RIXS from NiAl at the K Edge of Ni

To show the validity of the Bloch $\vec{k}$-momentum conservation in the hard x-ray regime resonantly excited valence fluorescence spectra have been measured from a single crystal sample of the ordered stoichiometric alloy Ni_1Al_1, using excitation energies $\hbar\omega_1$ close to the Ni K edge. By using a binary compound one can show the element specificity of RIXS. Moreover, the difficulties related to core excitons [Veen97] are not present in this metallic sample. Stoichometric NiAl crystallizes in the CsCl structure with a lattice constant of $a = 2.88$ Å. Since it has only one Ni and one Al atom within the unit cell and due to the high symmetry of the crystal, the band structure consists only of a few bands (see Fig. 1.3). Therefore, the conduction band structure of NiAl allows to select a relatively limited number of Bloch $\vec{k}$-points to contribute to absorption and emission.

The measurements have been performed at beamline ID28 at the ESRF using a Rowland spectrometer suited for spherically bent analyzer crystals with a bending radius of 1 m, allowing for an energy resolution of about 0.5 eV at 8 keV photon energy. The spectrometer and its x-ray optical properties are described elsewhere [Schü95, Kao96]. A short description can be found in Appendix E. The incident radiation was monochromatized to about 8335 eV by a Si 111 double crystal monochromator and an additional two-reflection Si 333 channel cut crystal. The energetic width of the incident beam was set to 0.85 eV resulting in an over-all experimental resolution of 1.0 eV FWHM. Valence fluorescence spectra have been measured for a set of four $\vec{q}$-values each parallel to the $\langle 110 \rangle$ axis and for 5 different incident energies $\hbar\omega_1$ for each $\vec{q}$. Series of measured spectra for fixed $\vec{q}$ and for fixed $\hbar\omega_1$ are shown in Figs. 3.1, 3.2, and 3.3, respectively, clearly featuring dependence on both the incident energy and the momentum transfer.

The experimentally choosen values for $\vec{q}$ within the first Brillouin zone were 0.1,

Table 3.1: Experimentally chosen reduced and absolute values of the momentum transfer $\vec{q}$ and corresponding scattering angles for NiAl.

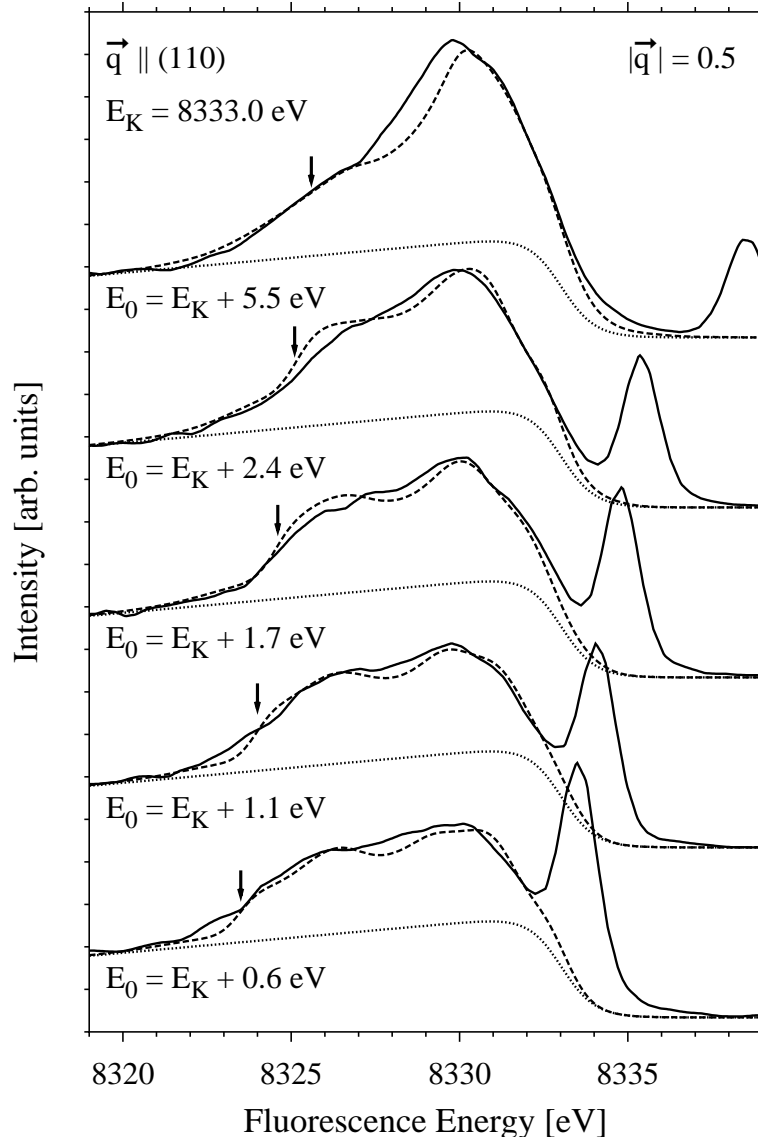| $\vec{q}_{\mathrm{red}}$ $[2\pi/a]$	$\vec{q}_{\mathrm{abs}}$ $[2\pi/a]$	$|\vec{q}_{\mathrm{abs}}|$ [a.u.]	Θ [°]
0.1 $\cdot\langle 110 \rangle$	1.9 $\cdot\langle 110 \rangle$	3.43	87.86
0.25 $\cdot\langle 110 \rangle$	1.75 $\cdot\langle 110 \rangle$	3.16	79.43
0.4 $\cdot\langle 110 \rangle$	1.6 $\cdot\langle 110 \rangle$	2.88	71.50
0.5 $\cdot\langle 110 \rangle$	1.5 $\cdot\langle 110 \rangle$	2.71	66.42

Figure 3.1: Measured (solid lines) and calculated (dashed lines) spectra with constant momentum transfer together with the estimated radiative Auger satellite (dotted line). The incident energy $E = \hbar\omega_1$ is given with respect to the Ni 1s binding energy (8333 eV). $|\vec{q}|$ is given in units of $|\langle 110 \rangle|\frac{2\pi}{a}$. The narrow peak dispersing from 8333.6 eV to 8338.5 eV is due to quasi-elastic scattering. To make the calculated spectra comparable to the experiment the sum of the calculated spectra and the estimated satellite are shown.

0.25, 0.4, and 0.5 in units of $\langle 110 \rangle \cdot \frac{2\pi}{a}$, a being the lattice constant. To suppress the quasi-elastic line (see Chapter 1 Page 10) a scattering angle close to 90° is desirable. Therefore, $\vec{q}$ has been extended by a $\langle 220 \rangle$ reciprocal lattice vector, according to $\vec{q}_{abs} = \vec{q}_{red} + \langle 220 \rangle$, where $\vec{q}_{red}$ denotes the reduced vector being confined to within the first Brillouin zone. Table 3.1 summarizes the reduced and absolute values of the momentum transfer as well as the corresponding scattering angles. The excitation
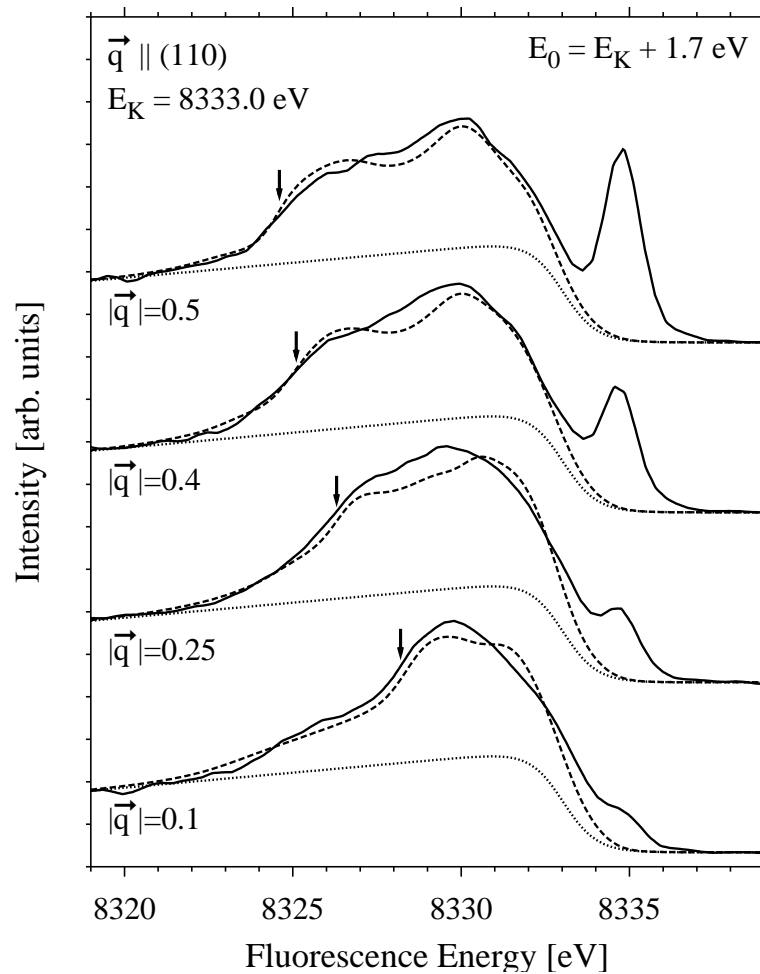
Figure 3.2: Measured (dashed lines) and calculated (solid lines) spectra with constant incident energy together with the estimated radiative Auger satellite (dotted line). Units are as in Fig. 3.1.

energy $\hbar\omega_1$ for each $\vec{q}$ was set to 0.6, 1.1, 1.7, 2.4, and 5.5 eV above the 1s binding energy of Ni (8333 eV).

Inherent to this technique is the fact that the valence emission spectra lie on top of the so-called radiative Auger satellite to the valence line, being the excitation of another valence electron into the conduction band during the emission process resulting in an energy loss to the emitted photon (see for example [Åber71]). The minimal energy loss of this process is zero whereas the maximum energy loss is only limited by the fluorescence energy of the corresponding parent line. Therefore, the radiative Auger satellite of the valence line is showing a steep drop on its high energy side coincident with the binding energy of the 1s electron and a slowly decreasing tail on its low energy side as is indicated in Figs. 3.1–3.3. Since the behaviour of the satellite in this energy regime has not yet been calculated and since this satellite cannot be measured independently from its parent line it has to be approximated by a model function. The satellite line shown in Fig. 3.1–3.3 consists of a linear
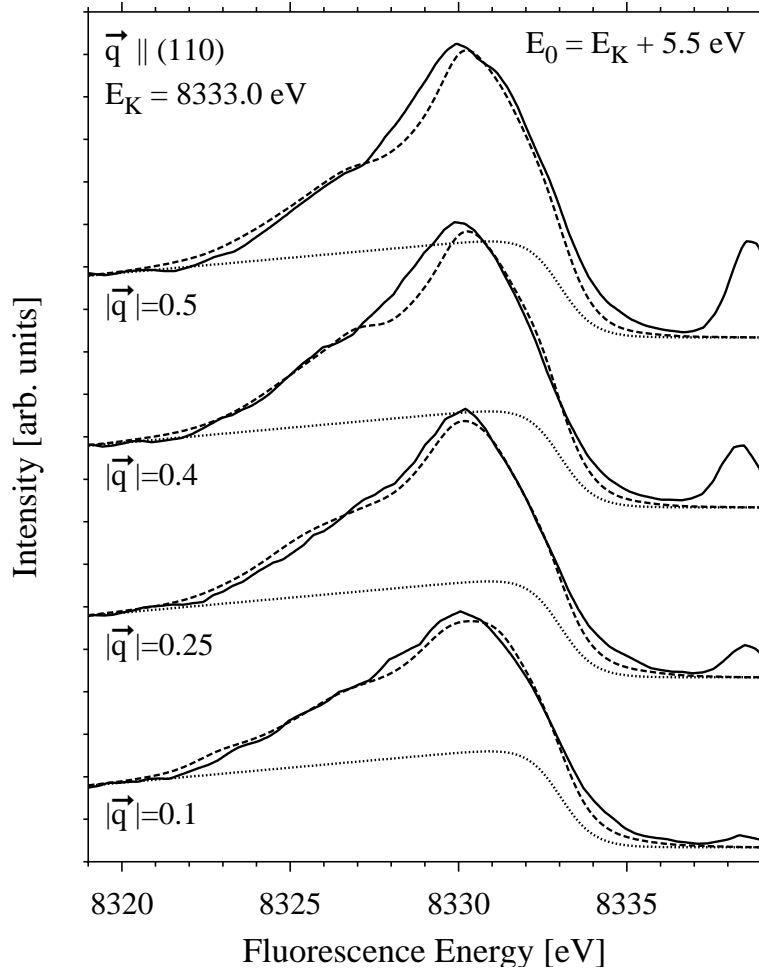
Figure 3.3: Measured (dashed lines) and calculated (solid lines) spectra with constant incident energy together with the estimated radiative Auger satellite (dotted line). Units are as in Fig. 3.1.

function multiplied by a arctan function with a width of 2.2 eV. The radiative Auger satellites will be discussed in more detail in Chapter 7.

The measured spectra are compared to theoretical RIXS spectra calculated from Eq. 1.25 as derived in Chapter 1. The calculated spectra are based on a band structure calculation obtained with the WIEN97 package [Wien97], using the full potential LAPW algorithm as described in Chapter 2. The energy eigenvalues and the partial charges at 9139 $\vec{k}$-points within the irreducible wedge of the first Brillouin zone have been used. Furthermore, the finite energy resolution of both the monochromator and the spectrometer together with the lifetime broadening of the 1s core hole were taken into account. Additionally, self absorption effects have been accounted for. Part of the code used for the calculation is described elsewhere [Enki98].

While the dipole approximation generally yields satisfactory results, this is not the case for the valence fluorescence spectra of the late 3d elements. In the case of Ni

Figure 3.4: The CsCl crystal structure and the irreducible wedge of the Brillouin zone of NiAl.
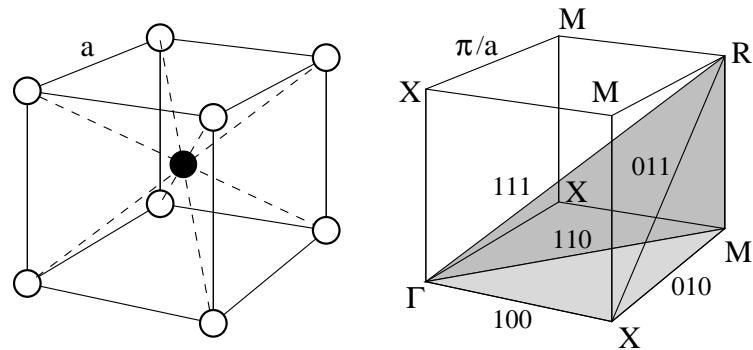
0.45 4p electrons contribute to the dipolar transition into the 1s core hole but 9 3d electrons give rise to the quadrupolar transition. Assuming that the quadrupolar matrix element is two orders of magnitude smaller than the dipolar matrix element, 20 % of the fluorescence intensity are due to the 3d→1s quadrupolar transition.

For the calculation of the RIXS spectra of NiAl the energy dependence of the dipole matrix elements of the Ni-1s to Ni-4p transition, as calculated by the WIEN97 program, has been used, whereas for the quadrupolar Ni-3d to Ni-1s transition a constant matrix element as estimated above has been applied. The relative intensity of the 4p→1s dipolar and the 3d→1s quadrupolar transitions as well as the energy dependence of the quadrupolar matrix element will be discussed in Chapter 6.

As can be seen from Figs. 3.1–3.3 there is considerable agreement between the measured and the calculated spectra. Despite the fact that the Bloch $\vec{k}$-space resolution (via the conduction band structure) is limited by the energy width of the intermediate state ($\Gamma = 1.44$ eV [Zsch89]), the shape of the fluorescence spectra changes significantly with both the incident energy (Fig. 3.1) and the momentum transfer (Fig. 3.2). A dispersion of the low energy shoulder in both cases (marked by the arrows) is clearly visible. Also the growth of the main peak at -3 eV with increasing incident energy is nicely reproduced in the calculated spectra (Fig. 3.1), justifying the assumptions made above.

These changes can be easily explained by distinct features of the electronic band structure (see Fig. 3) in connection with the length and the orientation of the momentum transfer $\vec{q}$ relative to the crystal axes of the sample. The unit cell of NiAl and the corresponding irreducible wedge of the Brillouin zone are depicted in Fig. 3.4. If $\hbar\omega = E_K + 1.7$eV (Fig. 3.2), the possible values for $\vec{k_i}$ are distributed around the R-point. With increasing $|\vec{q}|$ the $\vec{k_f}$ are shifted parallel to the 110 direction from the R-point to the X-point and consequently the lowest band with p-character around X causes the dispersing shoulder. Similarly in Fig. 3.1 the growth of the main peak at -3 eV is originating from the p-states around M.

Even though the spectra of the series with $\hbar\omega = E_K + 5.5$ eV (Fig. 3.3) are different from the spectra at $\hbar\omega = E_K + 1.7$ eV, the changes with varying $\vec{q}$ are not as large as in the series at lower energy. From the good agreement with the calculated spectra taking into accout the fully $\vec{k}$-conserving scattering process, one can conclude that this decreasing $\vec{q}$-sensitivity is exclusively a band structure effect. The reduced $\vec{k}$-selectivity of the spectra gives evidence of an increased number and a more widely
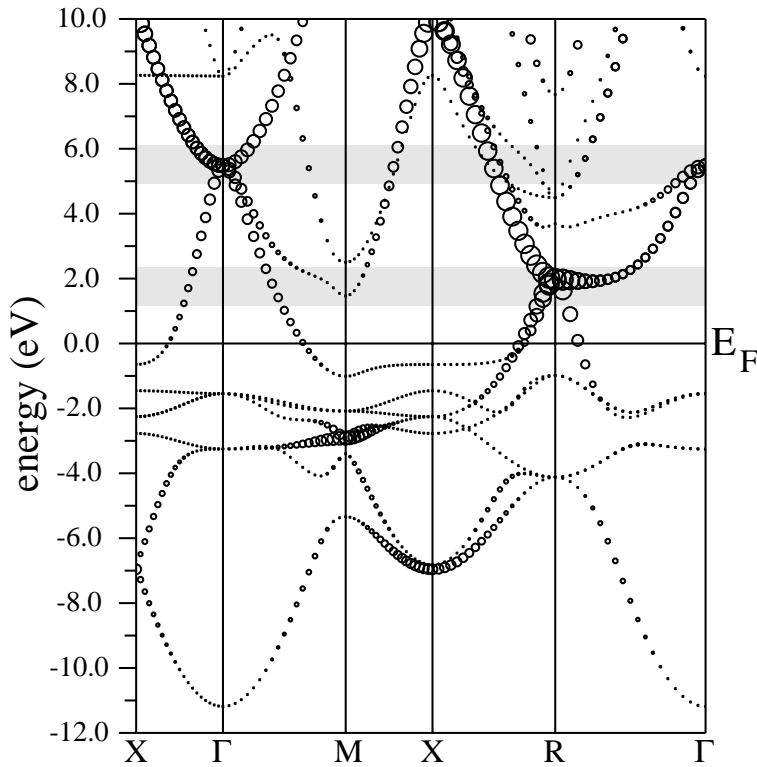
Figure 3.5: The electronic band structure of NiAl. The lower and upper bar indicate the incident energy at which the RIXS spectra depicted in Fig. 3.2 and Fig. 3.3 have been measured, respecively.

spread distribution of $\vec{k_f}$-points that contribute to the emission, originating from the increased number of bands in the energy region dominating the absorption process.

Thus, one has to distinguish between the $\vec{k}$-conservation, which is an attribute of the RIXS process, and the $\vec{k}$-selectivity, being a property of the RIXS spectrum.

The possible destruction of the $\vec{k}$-conservation due to interaction with phonons will be treated in Chapter 4.

Conclusion

The Bloch $\vec{k}$-momentum conservation is valid in the hard x-ray regime and RIXS spectra from the metallic NiAl sample show the expected Bloch $\vec{k}$-selectivity. The use of hard x-rays makes the Bloch $\vec{k}$-selective RIXS spectra dependent on both the incident energy *and* the momentum transfer.

Chapter 4

Destruction of the Bloch $\vec{k}$-Momentum Conservation

As shown in Chapter 1, the Bloch $\vec{k}$-momentum selectivity of resonantly excited valence fluorescence spectra is based on the Bloch $\vec{k}$-momentum conservation in the RIXS process. However, this picture is only true as long as apart from the electrons directly involved in the scattering process no interaction with quasi-particles like phonons takes place.

In the case of such an intermediate state relaxation, certain energy and momentum is added to or removed from the electron system of the sample. Since the energy of a phonon is usually much smaller than the energies of interest in the valence band the energy transfer provoked by the phonon can be neglected. In contrast, the momentum transferred by the phonon can adopt arbitrary values within the first Brillouin zone. Therefore, the momentum $\vec{q} = \vec{k}_1 - \vec{k}_2$ deposed into the sample by the photons differs from the momentum $\vec{q}_{\mathrm{el}}$ actually transferred to the electron system (see Fig. 4.1).

Figure 4.1: Alteration of the momentum transfer by interaction with phonons.
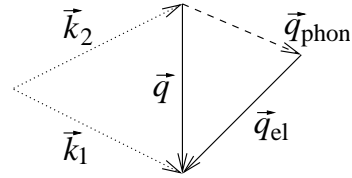
In other words, the momentum of the phonon must be included into the Kronecker-δ (see Eq. 1.25) expressing the momentum conservation:

$$\delta_{\vec{G},(\vec{k}_1 - \vec{k}_2 - \vec{k}_i + \vec{k}_f)} \implies \delta_{\vec{G},(\vec{k}_1 - \vec{k}_2 - \vec{k}_i + \vec{k}_f + \vec{q}_{\mathrm{phon}})}. \tag{4.1}$$

Since the momentum of the phonon is only limited by the first Brillouin zone, the actual momentum transfer $\vec{q}_{\mathrm{el}}$ is randomized and the Bloch $\vec{k}$-momentum conservation of the RIXS process is lost. If the randomization is complete, the whole Brillouin zone contributes to the emission process and the RIXS spectra resemble the shape of ordinary $\vec{k}$-unselective fluorescence spectra, as obtained if the incident energy is high above the respective absorption threshold.

4.1   The Shape of the $\vec{k}$-Unselective Spectrum

As will be shown in Section 7.4 even in the case of a non $\vec{k}$-conserving process
the RIXS spectra depend on the energy of the incident photon via the core hole
Lorentzian and via the fine structure of the unoccupied DOS, leading to the x-ray
resonant Raman effect. Moreover, satellite lines due to double ionization processes
during the absorption of the incoming photon may change the shape of RIXS spectra
from valence electrons (see introductory section of Chapter 7). Therefore, a $\vec{k}$-
unselective spectrum must be measured at incident energies in the same range as
the $\vec{k}$-selective spectra are recorded.

To obtain a $\vec{k}$-unselective spectrum the momentum transfer $\vec{q}$ has to be randomized
completely. This can be done in two different ways: The $\vec{k}$-unselective spectrum can
be calculated by averaging a complete set of measured $\vec{k}$-selective spectra, whose
different momentum transfer vectors cover the whole first Brillouin zone, or it may
be obtained from a powder sample. However, these different approaches feature a
subtle difference. By averaging a complete set of measured spectra the direction
and the magnitude of $\vec{q}$ are averaged, whereas in the case of a powder spectrum
only the direction of $\vec{q}$ is averaged. The aim of this section is to show that the two
approaches, despite their different influence on $\vec{q}$, yield identical spectra. Fig. 4.2
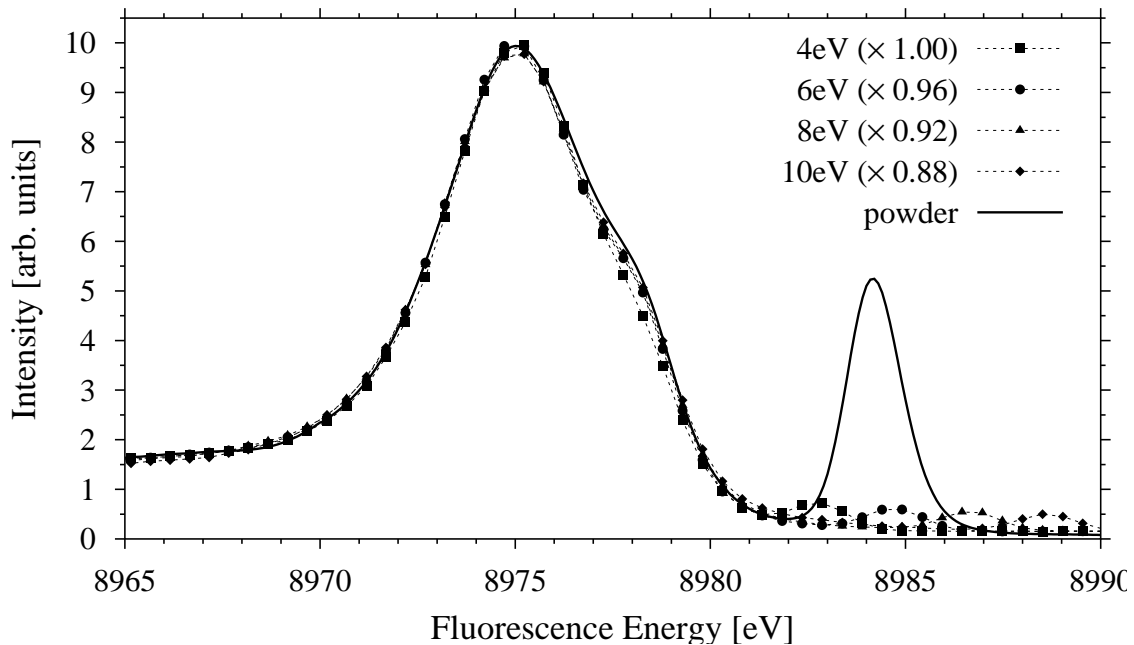shows $\vec{k}$-unselective valence fluorescence spectra of Cu obtained by the two different
methods.

Figure 4.2: Bloch $\vec{k}$-unselective RIXS spectra from valence electrons of Cu. The
spectra drawn with dotted lines have been calculated by averaging sets of
measured $\vec{k}$-selective spectra. The respective incident energies relativ to the 1s
binding energy of 8979 eV and the scaling factors are indicated in the key. Drawn
with a solid line is a spectrum obtained from a powder sample.

In the calculation of the four averaged spectra 8 different values of $\vec{q}$ have been accounted for. The complete set of measured Bloch $\vec{k}$-selective RIXS spectra from Cu is shown in App. D. For details of the experimental conditions see Chapter 8. To compensate for the increasing fluorescence intensity as the incident energy is raised the spectra have been scaled as indicated in the figure.

The powder spectrum has been measured at the HARWI beamline of the HASYLAB using the 511 Si sagittally focussing double crystal monochromator and the Rowland spectrometer [Wohl00] using a spherically bent 553 Si analyzer crystal with a bending radius of 1 m, resulting in an over-all energy resolution of about 1 eV. As can be seen from the position of the quasi-elastic line, the powder spectrum has been measured at 5 eV above the absorption threshold, i.e. within the energy range where RIXS spectra from single crystal samples show the Bloch $\vec{k}$-selectivity. To suppress the statistical noise and due to the different energy resolutions of the two different data sets the powder spectrum has been convoluted by a Gaussian with a FWHM of 1eV.

Despite the difference of the two methods the spectra have identical shape, except for the averaged spectrum measured at 4 eV above the K edge. This can be attributed to the fact that the $\vec{k}$-selectivity of the spectra reduces with increasing incident energy, as described in Chapter 3. At 6 eV above the absorption threshold the whole irreducible wedge of the Brillouin zone is sampled by the $\vec{k}_f$ acessible by as few as 8 different values of $\vec{q}$. In contrast, at smaller incident energies the $\vec{k}$-selectivity of the spectra is so large, that 8 different values of $\vec{q}$ are not sufficient to yield a uniform distribution of the $\vec{k}_f$ within the first Brillouin zone.

Thus, RIXS spectra from a powder sample can considered to be completely $\vec{k}$-unselective.

4.2 $\vec{k}$-Conservation and $\vec{k}$-Selectivity

In extension to the nomenclature defined on Page 30 it is usefull to distinguish between $\vec{k}$-unselective and non-$\vec{k}$-conserving spectra. A $\vec{k}$-unselective spectrum is characterized by the fact that the whole first Brillouin zone contributes to the fluorescence process. It is not important, how the uniform distribtion of the $\vec{k}_f$ is accomplished, whether it is due to band structure features or due to a non-$\vec{k}$-conserving scattering process, e.g. due to interaction with phonons. Thus, a non-$\vec{k}$-conserving spectrum always is $\vec{k}$-unselective.

In contrast, a $\vec{k}$-conserving spectrum may be $\vec{k}$-selective (e.g. the spectra from NiAl excited at 1.7 eV above the Ni K edge, shown in Fig.3.2) or $\vec{k}$-unselective (e.g. the spectra from NiAl excited at 5.5 eV above the Ni K edge, shown in Fig.3.3), depending on the band structure and on the incident energy.

If for a certain fraction of the scattering processes the Bloch $\vec{k}$-conservation is destroyed, the resulting RIXS spectrum can be considered to be a combination of a non-$\vec{k}$-conserving and of a $\vec{k}$-conserving spectrum:

$$I_{\text{total}}(\hbar\omega_2) = (1 - f) \cdot I_{\text{non}-\vec{k}-\text{cons}}(\hbar\omega_2) + f \cdot I_{\vec{k}-\text{cons}}(\hbar\omega_2). \qquad (4.2)$$

Throughout the literature dealing with soft x-ray Bloch $\vec{k}$-selective RIXS, the pure $\vec{k}$-conserving contribution is obtained by subtracting the largest possible fraction of a $\vec{k}$-unselective spectrum from each spectrum, without resulting in negative intensities. Thus, for each incident energy a different $\vec{k}$-conserving fraction is obtained. The $\vec{k}$-unselective spectrum is usually obtained by measuring a fluorescence spectrum excited high above the absorption threshold [Eise00]. As pointed out above, satellites due to double ionization processes during the absorption of the incident photon must not be present in this high energy spectrum, calling for special attention.

However, this procedure is strictly speaking valid only, if the purely $\vec{k}$-conserving spectra strongly differ from the $\vec{k}$-unselective spectum. More precisely, each $\vec{k}$-conserving spectrum must exhibit a region of vanishing intensity within the valence band region. Otherwise, if even from a $\vec{k}$-conserving spectrum some fraction of the $\vec{k}$-unselective spectrum can be subtracted. Then the $\vec{k}$-conserving fraction is underestimated and the extracted $\vec{k}$-conserving spectrum is not correct. This is demonstrated by the calculated RIXS spectra from NiAl (see Figs. 3.1, 3.2, and 3.3 in Chapter 3). Although these spectra are $\vec{k}$-conserving, large fractions of a $\vec{k}$-unselective spectrum can be subtracted. Moreover, from Ni spectra and from Cu spectra (see App. D) measured at the same incident energy but at different momentum transfer vectors, different fractions of the $\vec{k}$-unselective spectrum can be subtracted, clearly indicating that this approach fails in this case.

As can be observed in all series of Bloch $\vec{k}$-selective RIXS spectra, the $\vec{k}$-selective fraction of a RIXS spectrum (i.e. what remains after the subtraction of the largest possible $\vec{k}$-unselective fraction) decreases with increasing incident energy (see for example [Lüni97, Eise00]). According to [Eise00], this behaviour is due to the electron-phonon scattering rate which increases with the energy of the excited electron. In fact, in the case of Si the incident energy dependence of the $\vec{k}$-conserving fraction calculated from the electron-phonon scattering rate agrees qualitatively with the fraction obtained from the measured spectra [Eise00].

According to [Ma94] the $\vec{k}$-conserving fraction f can be estimated from the energetic lifetime broadening of the intermediate state Γ_c and the Debye energy $\hbar\omega_{\mathrm{D}}$:

$$f \approx e^{-\frac{\hbar\omega_{\mathrm{D}}}{\Gamma_c}} \tag{4.3}$$

Table 4.1 compares values of f calculated according to Eq. 4.3 to measured ones for some substances. Despite the simplicity of the relation used, the calculated values agree fairly good in the case of diamond and Si. If one assumes that Eq. 4.3 yields the upper limit for the $\vec{k}$-conserving fraction, this would imply, that the $\vec{k}$-unselective fraction measured at the absorption edge is solely due to electron-phonon scattering and that no band structure effects contribute to the $\vec{k}$-unselective fraction. As a consequence, if this was perfectly true, the $\vec{k}$-selective fraction would equal the $\vec{k}$-conserving spectrum.

However, the agreement between the calculated and the measured $\vec{k}$-conserving fraction is bad for the case of SiC, indicating that either Eq. 4.3 fails or that the $\vec{k}$-conserving fraction cannot be determined by the subtraction of a $\vec{k}$-unselective spectrum. In the light of the above considerations, it is unclear to which extent the

Subst	edge	E [eV]	Γ_c [eV]	θ_D [K]	$\hbar\omega_D$ [eV]	$f_{cal.}$	$f_{meas.}$	
diam	C K	285	0.16	2230	0.19	0.3	0.4	[John94]
SiC	C K	285	0.16	1270	0.11	0.5	0.3 - 0.1	[Lüni97]
	Si L$_{2,3}$	100	0.10	1270	0.11	0.3	0.6 - 0.1	[Lüni97]
Si	Si L$_{2,3}$	100	0.10	645	0.055	0.6	0.7 - 0.4	[Eise00]
	Si K	1841	0.48	645	0.035	0.9	-	
Cu	Cu K	8971	1.55	343	0.030	0.98	-	

Table 4.1: Measured and calculated $\vec{k}$-selective fractions

$\vec{k}$-unselective fraction obtained from the measured spectra is due to electron phonon scattering and to which extent it is merely stemming from the increasing number of bands present at higher energies above E_F, as it is the case for NiAl and Cu. Certainly more investigations are necessary in this field.

Despite the above limitations it is possible to extract part of the band structure from RIXS spectra of SiC [Lüni97]. As a rule of thumb, the above procedure is expected to work best if there are few bands in the valence region and if the core hole broadening is small.

4.3   Determination of the $\vec{k}$-Conserving Fraction

According to Eq. 4.3 a $\vec{k}$-conserving fraction of nearly 100% is expected for Cu, if only electron-phonon interactions are considered to destroy the $\vec{k}$-momentum conservation. Accounting for the increase of electron-phonon scattering rate with increasing incident energy, a reduction of the $\vec{k}$-conserving fraction is expected at higher incident energies.

The electron-phonon interaction can result in the creation as well as in the annihilation of a phonon. Of course, the phonon annihilation rate is proportional to the number of phonons present and thus depends on the temperature of the sample. Accordingly, Eq. 4.3 is transformed into

$$I_{total}(T) = (1 - f(T)) \cdot I_{non-\vec{k}-cons} + f(T) \cdot I_{\vec{k}-cons}. \tag{4.4}$$

Thus, it is possible to determine the phonon contribution to the non-$\vec{k}$-conserving fraction, independent of the loss of $\vec{k}$-selectivity due to the increasing number of bands, by performing a temperature dependent experiment. Although only the non-$\vec{k}$-conserving contribution due to the annihilation of phonons is thereby obtained, at least the order of magnitude of the total phonon contribution can be gained.

A $\vec{k}$-selective RIXS spectrum from Cu has been measured at two different temperatures under otherwise identical experimental conditions. The spectrum measured at room temperature then can be calculated as the weighted sum of the purely $\vec{k}$-conserving spectrum measured at 10 K and of the purely $\vec{k}$-unselective spectrum
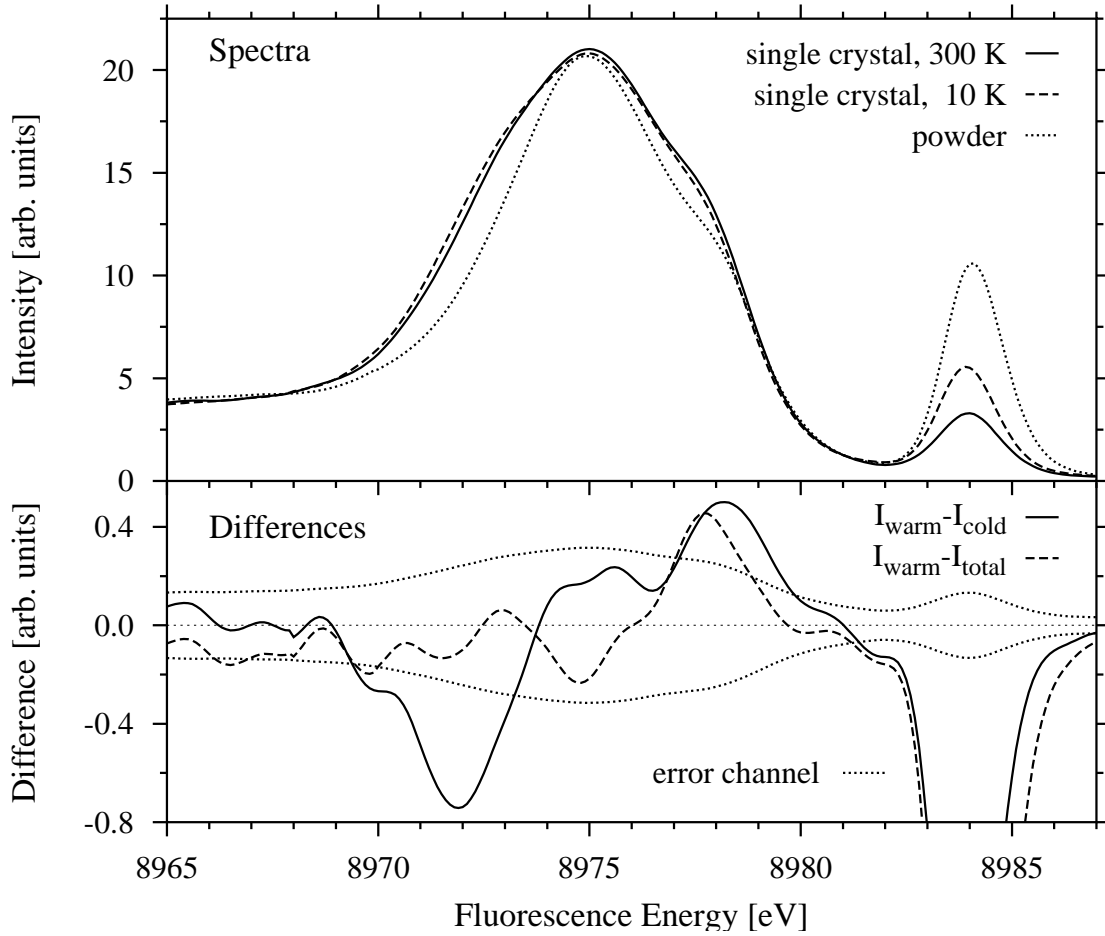
Figure 4.3: Measured $\vec{k}$-selective RIXS spectra from Cu at room temperature (solid line) and at 10 K (dashed line) together with the $\vec{k}$-unselective spectrum obtained from a powder sample (dotted line). The spectra have been convoluted with a Gaussian with a FWHM of 1 eV. In the lower panel difference spectra are shown, as decribed in the text.

obtained from the powder sample:

$$I_{\text{warm}} \overset{!}{=} I_{\text{total}} = (1 - f'(300K)) \cdot I_{\text{powder}} + f'(300K) \cdot I_{\text{cold}}. \tag{4.5}$$

The variational parameter f', denoting the $\vec{k}$-conserving fraction when only phonon annihilation processes are accounted for by the $\vec{k}$-unselective fraction, is determined by means of a fit procedure demanding $I_{\text{warm}} \overset{!}{=} I_{\text{total}}$.

The incident energy $\hbar\omega_1 = E_K + 5$ eV $= 8984$ eV and the momentum transfer $\vec{q}_{\text{abs}} = 3.0 \cdot \langle 100 \rangle \frac{2\pi}{a} \Leftrightarrow \vec{q}_{\text{red}} = 1.0 \cdot \langle 100 \rangle \frac{2\pi}{a}$, corresponding to $\Theta = 70°$, were chosen to yield a $\vec{k}$-selective RIXS spectrum that significantly differs from the $\vec{k}$-unselective spectrum. The $\vec{k}$-selective spectrum from the single crystal sample has been measured at room temperature and at 10 K and is shown in Fig. 4.3, in comparison to the spectrum obtained from the powder sample. To facilitate the comparison of the three spectra they have been convoluted with a Gaussian of a FWHM of 1 eV, suppressing the

statistical noise of the spectra. As shown in the upper panel, the valence spectrum obtained from the powder (non-$\vec{k}$-conserving RIXS) differs significantly from the spectra obtained from the single crystal ($\vec{k}$-conserving RIXS), whereas latter spectra are quite similar to each other. In the lower panel the differences of the spectra are depicted. The difference between the two single crystal spectra (solid line) shows a asymmetry that is larger than the statistical error, as indicated by the error channel (dotted lines), and thus is significant. Drawn with a dashed line is the difference remaining after the fit according to Eq. 4.5, yielding $f' = 75$ %. Although smaller than the difference $I_{\mathrm{warm}} - I_{\mathrm{cold}}$ a significant asymmetry is still present, which will be discussed in what follows.

4.4   Thermal Expansion of the Sample

The residuum of the difference $I_{\mathrm{warm}} - I_{\mathrm{total}}$ may stem from the change of the valence band width due to the thermal expansion of the sample, that has been neglected so far. If the temperature is reduced from 300 K to 10 K the lattice constant reduces by 0.345 % from $a_{T=300\mathrm{K}} = 3.6044$ Å to $a_{T=10\mathrm{K}} = 3.6022$ Å, as can be determined from a direct measurement (-0.35 %) and from the integration of the temperature dependent thermal expansion coefficient (-0.34 %) [LandBö].

Using a = 3.6022 Å a band structure calculation of Cu has been performed, to determine the influence of thermal expansion on the shape of the valence band. The resulting calculated $\vec{k}$-selective valence spectrum at 10 K is compared to the respective spectrum calculated at 300 K in Fig. 4.4. As in the experiment the
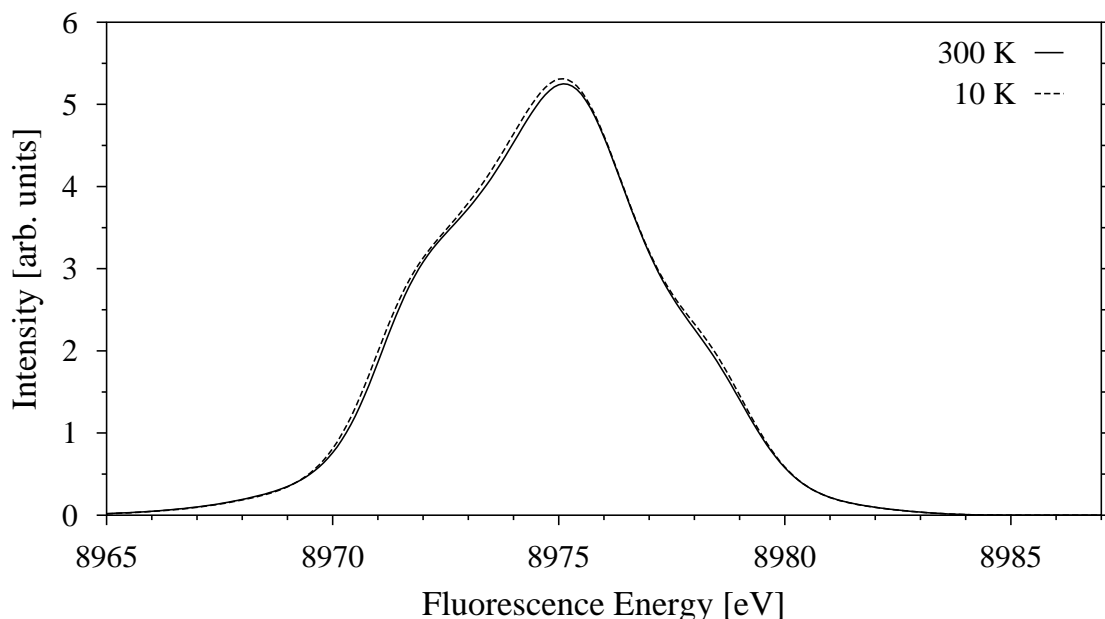

Figure 4.4: Calculated $\vec{k}$-selective RIXS spectra from Cu at room temperature (solid line) and at 10 K (dashed line). The radiative Auger satellite has been omitted.

spectrum at low temperature is broader than the spectrum at room temperature. This is due to the fact that at low temperatures the lattice constant is smaller, the overlap between neighbouring atoms is larger and thus the band width is larger at lower temperatures. In the case of the calculated spectra good agreement between the 10 K and the 300 K spectrum can be obtained, if the energy axis of the 10 K spectrum is stretched by $c = 1.5$ % according to $E' = E + (1 + c)(E - 8979$ eV$)$. In analogy, the two different measured spectra can be made equal by applying a stretching factor of $c = 2.2$ % to the 10 K spectrum, beeing not too different from $c = 1.5$ % in the case of the calculated spectra.

Thus, the spectrum measured at room temperature can be obtained from the spectrum measured at 10 K either by acounting for the thermal expansion by means of a stretching factor to the energy axis or by considering a non-$\vec{k}$-conserving contribution due to electron-phonon interactions in the intermediate state. The corresponding difference spectra $I_{\mathrm{warm}} - I_{\mathrm{stretched}}$ and $I_{\mathrm{warm}} - I_{\mathrm{total}}$ are depicted in Fig. 4.5. The asymmetry that is present in the difference $I_{\mathrm{warm}} - I_{\mathrm{total}}$ is not present in the difference $I_{\mathrm{warm}} - I_{\mathrm{stretched}}$. This clearly indicates, that thermal expansion of the sample is the dominating effect in the temperatre dependence of Bloch $\vec{k}$-selective RIXS spectra.
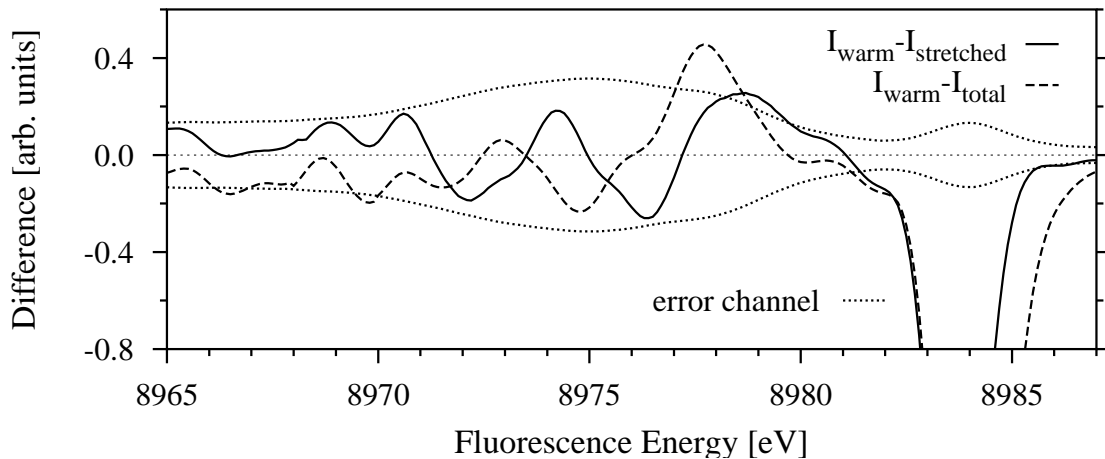

Figure 4.5: Differences of RIXS spectra from Cu. The spectrum at room temperature is obtained from the spectrum at 10 K either by acounting for the thermal expansion (solid line) or by considering a $\vec{k}$-unselective contribution (dashed line).

In the next step of investigation it is desirabel to account for both the thermal expansion and the non-$\vec{k}$-conserving processes in the calculation of the spectrum at 300 K from the spectrum measured at 10 K. Unfortunately the fit determining the stretch factor c and the $\vec{k}$-selective fraction simultaneously is highly unstable and thus does not yield any useful results. Moreover, if the fit according to Eq. 4.5 is performed with the stretch factor fixed at $c = 1.5$ % the difference still remains asymmetric. Therefore, within the statistical error of the present dataset, a non-$\vec{k}$-conserving fraction can neither be acertained nor be ruled out.

Conclusion

To date it is still unclear to what extent in the soft x-ray regime the electron-phonon interaction in the intermediate state contributes to the reduction of the Bloch $\vec{k}$-selectivity of RIXS spectra, if the incident energy is increased. More investigation is needed in this field.

In the hard x-ray regime the difference of shape between the $\vec{k}$-selective spectra measured at room temperature and at 10 K can be explained in terms of thermal expansion of the sample. The non-$\vec{k}$-conserving fraction, if any is present at all, amounts only to a few percent, as is expected from semiempirical considerations (see Eq. 4.3), but its precise determination is not possible from this dataset. In the following, the RIXS process in the hard x-ray regime will be considered to be purely $\vec{k}$-conserving.

Chapter 5

Screening of the Core Hole Investigated by a Supercell Calculation

As stated in Chapter 1, so far it has been assumed that in the scattering process only one electron is excited and another one is refilling the previously created core hole. All other electrons are assumed to remain 'frozen' in their states. In this case the ground state energy eigenvalues and wave functions can be used in the calculation of the scattering cross section. Indeed this picture is simplified too much, since the 1s hole present in the intermediate state is screened by the outer electrons, thereby changing their eigenvalues and wave functions. In a simplified treatment the ionized atom may be thought to have increased its atomic number by one, often treated in the so-called Z+1 approximation. Similarly the 4p hole in the final state is subject to screening, but since valence states are strongly delocalized their screening hardly affects the band stucture.

In the above considerations it has been implicitly assumed that the interaction time of the excited core electron with the photon is long enough to allow for the relaxation of the other electrons in the ionized atom and in the surrounding atoms. As a rule of thumb, the 'frozen core' or 'sudden' approximation[1] is valid if an excitation of an electron takes place to values high above its threshold energy, whereas the 'adiabatic' approximation has to be applied if relaxation effects become important, which is the case if the process occurs near its threshold. This is due to the fact that near the threshold energy the kinetic energy of the excited electron is small leaving sufficient time for the electron system to relax before the electron has left the vicinity of the ionized atom. Evidence for this assumption can be obtained e.g. from the X-ray satellites originating from double ionization processes during the absorption of a photon (see introductory section of Chapter 7). These processes show a characteristic onset energy and intensity saturation behaviour. In the saturation region, i.e. high above the threshold, the inensity of these satellites is properly accounted for by the sudden approximation, whereas in the onset region the adiabativ approximation is valid [Ster00]. Moreover, the onset energies and the energetic positions of

---

[1]A prominent example of the sudden approximation is the impulse approximation in the theory of Compton scattering, stating that the ground state momentum density is reflected in the Compton profile if the incident energy is much larger than the characteristic energies in the sample.

the satellites can be calculated within the Z+1 apprximation. Is the case of a RIXS process, the excitation takes place in the close vicinity of an absorption edge, thus justifying the assumption of total screening.

According to the final states rule the energy transferred in an absorption or emission process is determined by the electron configuration present in the respective final state. In the case of resonant inelastic scattering from valence electrons, the initial state is identical to the ground state of the electron system, the intermediate state is marked by the existence of a vacancy in a core level, and in the final state the core hole has been refilled and a hole state is present in the valence band (see Fig. 1.2). Since the intermediate state is the final state of the absorption part of the process, the absorption process is governed by the unoccupied DOS in the presence of a core hole. In analogy, the emission part of the scattering cross section is determined by the occupied DOS in the presence of a hole state in the valence band. Usually, due to its delocalization, the valence hole states are neglected, and a ground state band structure is used in the calculation of the emission energies.

In the framework of the density functional theory supercell calculations are widely used to account for the screening of core holes in crystalline samples. Within the supercell concept, the core vacancy of the ionized atom positioned in a finite crystal is approximated by an infinite number of periodically arranged core vacancies in an infinite crystal. The unit cell of this crystal, i.e. the supercell, consists of several primitive cells of the standard lattice. It contains only one ionized atom and several neutral ones. The fraction of ionized atoms in the supercell is reduced by the formation of unit cells containing more and more neutral atoms until the distance between neighbouring ionized atoms is so large that no interaction beween them is perceivable. In this limit, the supercell describes one single core state in an otherwise perfect single crystal. In the actual calculation, the supercells are increased step by step, until no further changes of DOS are observed.

Due to the localization of the core state involved in the RIXS process, only the partial DOS of the atom whose core electron is excited plays a role in the absorption and the emission process (see Section 6.4). In the RIXS process at the Cu K edge the core hole can be accounted for by calculating the partial 4p-DOS of the ionized atom together with its corresponding $1s \rightarrow 4p$ matrix element, and by the consideration of both in the absorption part of the scattering process.

In this chapter the application of the supercell method to the 1s core hole in Cu, occuring in the RIXS process from valence electrons at the Cu K edge, is presented. After describing the geometry of the considered supercells the influence of the core hole on the DOS of the ionized atom and on the neighbouring atoms is described. Then a detailed description of the convergence of the DOS with inreasing cell size is given, observing various parameters such as the DOS of the ionized and of the neutral atoms, the energy of core states, and the number of iterations needed to obtain a self-consistent charge distribution. Finally, the influence of the core hole on the K-XANES is discussed.

5.1   Geometry of the Supercells

Supercells with total numbers of 4, 8, 32, and 108 atoms have been accounted for. However, some of these atoms are equivalent to each other since they have the same distance from the ionized atom, which is demonstrated in Fig. 5.1. This twodimensional supercell contains a total number of four atoms but only three of them are inequivalent ones. Atom A has the vacancy in the 1s orbital, whereas the other three atoms are in their ground states. The two atoms labeled B are equivalent to each other, since their four nearest neighbours are two ionized atoms and two neutral atoms, whereas atom C has only neutral atoms on its nearest neighbour sites. Accordingly, the atoms in the three-dimensional supercells are subdivided into groups of equivalent atoms.

Figure 5.1: Nonequivalent and equivalent atoms. In this twodimensional supercell the unit cell, marked by the dashed line, consists of four atoms. Of these only three are inequivalent ones. The two atoms labeled B are equivalent to each other.
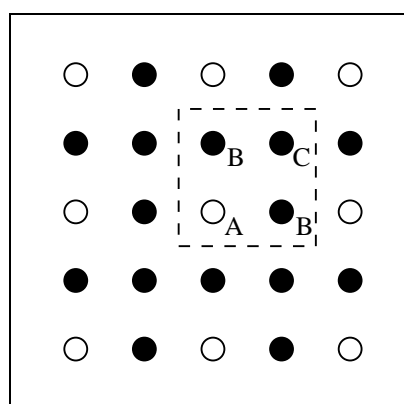
The atomic positions within the three smallest cells is depicted in Fig. 5.2. From left to right the cells contain a total number of 4, 8, and 32 atoms and have 2, 3, and 6 inequivalent positions, respectively, which are labeled A to F. The ionized atom is placed at position A. The cells containing 8 and 32 atoms are represented by an 8th of their simple cubic unit cells. Each color denotes a different class of equivalent atoms.

The supercells containing 4, 32, and 108 atoms have a simple cubic lattice, whereas
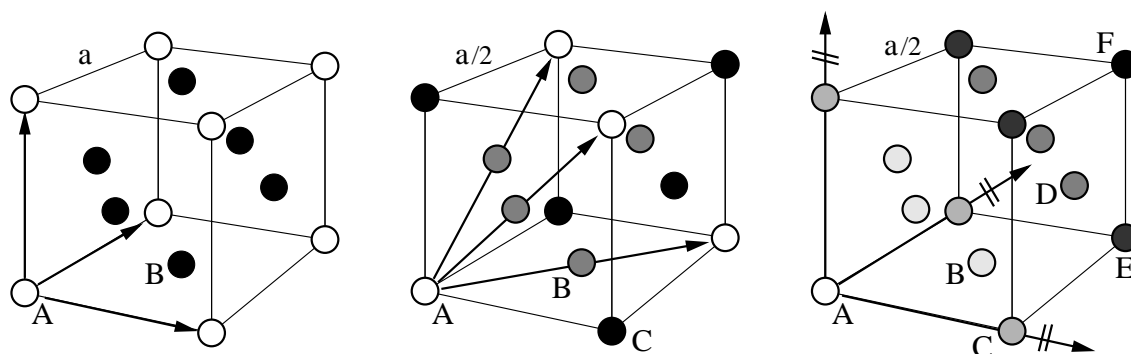
Figure 5.2: Atomic positions within the three smallest supercells of Cu. The primitive basis cells are spanned by three vectors as indicated. In the case of the cell containing 32 atoms the vectors have the length $\overline{AC} \cdot 2$.

N_{atom}	SG	a [Å]	a_{rel}	N_{ineq}	d_{ii} [Å]
1	fcc	3.61	1	1	2.55
4	sc	3.61	1	2	3.61
8	fcc	7.22	2	3	5.11
32	sc	7.22	2	6	7.22
108	sc	10.83	3	10	10.83

Table 5.1: Geometric parameters of the supercells for the consideration of the 1s core hole in Cu. The paramters are explained in the text.

the cell containing 8 atoms is based on a fcc lattice. The positions, equivalencies and distances of all atoms are given in Appendix A. Table 5.1 summarizes the basic geometric parameters of the supercells. Therein the total number of atoms in the supercell N_{atom}, the space group SG, the lattice constant a, the relative lattice constant a_{rel}, the number of inequivalent atoms in the supercell N_{ineq}, and the nearest neighbour distance between the ionized atoms d_{ii} are specified. d_{ii} increases linearly with the lattice constant, where in case of a fcc lattice a has to be divided by $\sqrt{2}$. The total number of atoms is calculated as $N_{\text{atom}} = a_{\text{rel}}^3 \cdot f$, where $f_{\text{fcc}} = 1$ and $f_{\text{sc}} = 4$, and the number of inequivalent atoms N_{ineq} increases like $\sqrt{N_{\text{atom}}}$.

Fortunately, the number of iterations N_{ite} required to obtain a self-consistent charge distribution does not rise proportional to N_{atom} but increases only slightly with the increase of N_{ineq} (see Table 5.2). However, in the case of the 108-atomic supercell $N_{\text{ite}} \approx 30$ is expected from the other cells, and the observed number of 50 iterations is surprisingly high. This finding will be discussed in Section 5.5.

Nevertheless, the total time t_{tot} needed to reach self-consistency dramatically increases with increasing cell size. This is due to the fact that the time $t_{\vec{k}}$ required to solve the eigenvalue problem for one $\vec{k}$-point depends on the number of plane waves N_{PW} used in the expansion and grows like $N_{\text{PW}}^{2\cdots3}$. Since the number of the plane waves is proportional to the total number of atoms in the unit cell, $t_{\vec{k}}$ shows the same rapid growth. On a PentiumII 233 MHz processor $t_{\vec{k}}$ ranges from a few seconds to many hours. However, the number of $\vec{k}$-points in the irreducible wedge of the Brillouin zone can be reduced as the supercell becomes larger, since the corresponding reciprocal unit cells becomes smaller and less $\vec{k}$-points are sufficient to

N_{atom}	N_{ineq}	N_{ite}	$N_{\vec{k}}$	$t_{\vec{k}}$	t_{ite}	t_{tot}	S_{RAM}
1	1	12	286	1.5 s	5 m	1 h	0.2 MB
4	2	14	165	7.8 s	21 m	5 h	1 MB
8	3	18	72	45 s	54 m	16 h	5 MB
32	6	23	20	63 m	21 h	21 d	75 MB
108	10	50	4	16 h	2.6 d	130 d	900 MB

Table 5.2: Computational requirements of the supercells.

create a grid of a given point distance. Thus, the time t_{ite} required to perform one cycle of the iteration process ranges from a few minutes to some hours, and the total time t_{tot} needed for the supercell calculation ranges from one hour in the case of the standard calculation to 130 days in the case of $N_{atom} = 108$.

To complete such a demanding calculation within reasonable time, one starts with a small set of $\vec{k}$-points that is extended as the charge density converges. Additionally, the calculation can be distributed to several machines, based on the splitting of the $\vec{k}$-mesh into smaller subsets. Moreover, the work space S_{RAM} required within the LAPW algorithm grows quadratic with the number of plane waves and thus is proportional to N_{atom}^2. In the case of the 108-atomic cell 1GB of work space was required.

5.2 Supercells without a Core Hole

To ensure that no artefacts occur due to the use of supercells, one can specify the ground state electron configuration for all atoms while retaining the classes of inequivalent atoms. This has been performed for the supercells with 4 and 8 atoms. The resulting partial densities of the p and d electrons are shown in Fig. 5.3. In
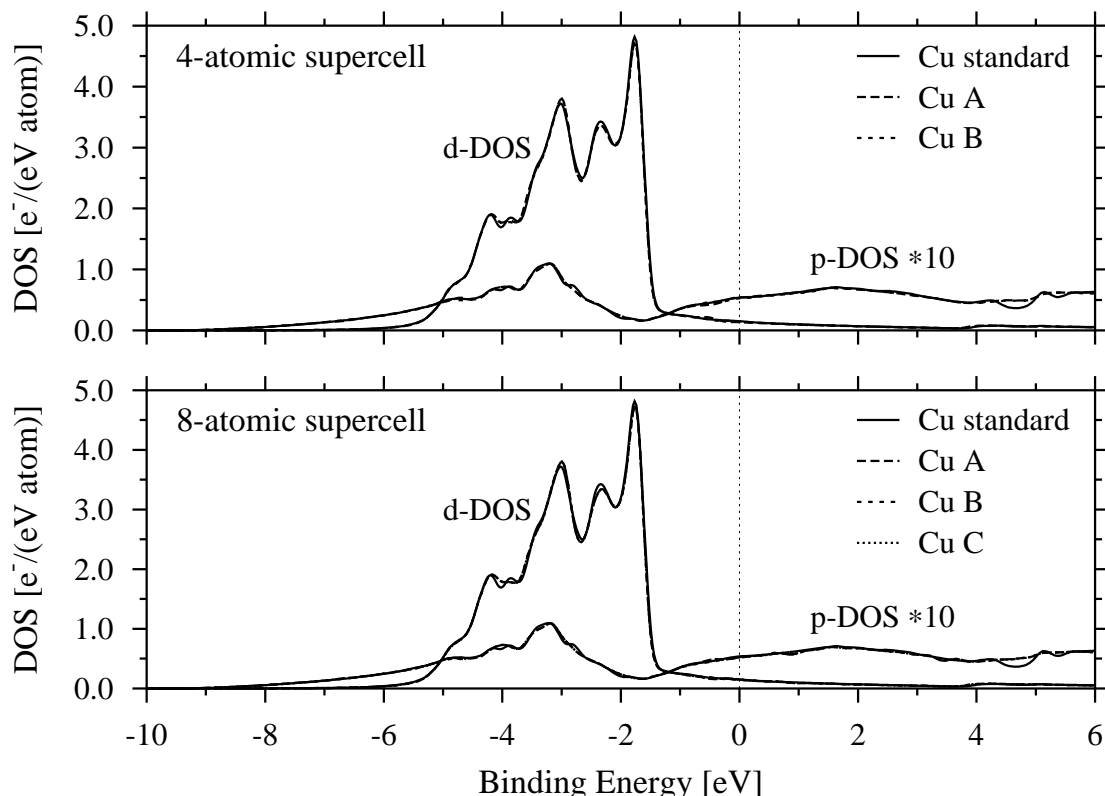

Figure 5.3: The Cu d- and p-DOS of 4 atomic and 8 atomic supercells without a core hole. The DOS of both supercells (dashed lines) are identical to the respective DOS of the standard calculation (solid lines). A, B, C denote the different inequivalent atoms.

both supercells the DOS of the inequivalent Cu atoms are identical to each other and agree well with the standard calculation of Cu. Artefacts due to the finite number of $\vec{k}$-points available in the $\vec{k}$-space integration have been suppressed by a convolution with a Gaussian with a FWHM of 0.2 eV.

The supercells without a core hole show an extremely slow convergence. Due to the absence of a force that pulls the charge into a certain direction, the charge oscillates indifferently between the identical but inequivalent atoms. Since these oscillations exhibit no damping, very small mixing parameters like $\alpha = 0.01$ and smaller together with the direct mixing scheme (see Section 2.3.4 Page 23) are required. To converge the charge distribution to the usual level, up to 100 steps of iteration are necessary. The convergence behaviour of the supercells containing 8 atoms with and without a core hole is shown in Fig. 5.4.
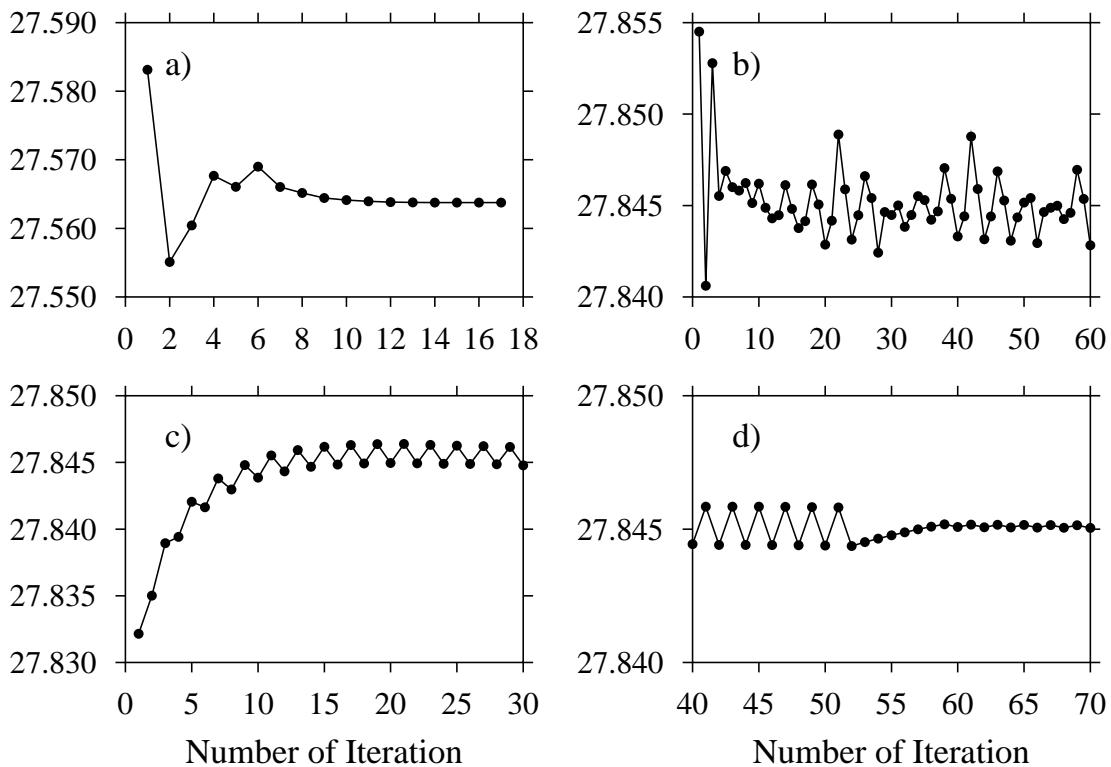

Figure 5.4: *The convergence behaviour of 8 atomic supercells with and without a core hole. The total charge within the atomic sphere at position A is plotted as a function of the number of iterations.*

The supercell with a core hole has reached convergence after 18 iterations (panel a), whereas the charge of the supercell without a core hole shows a quasiperiodic oscillation, if Broyden's mixing scheme (see Page 23) is used (panel b). In the case of direct mixing with a mixing parameter $\alpha = 0.1$ the oscillation is smaller (panel c), but to reach a level of convergence as in the case with core hole α had to be reduced to $\alpha = 0.01$ after the 52th iteration step (panel d).

5.3 Influence of the 1s Core Hole on the DOS

To demonstrate the general effect of the 1s core hole on the valence DOS in Cu, smallest supercell with $N_{\mathrm{atom}} = 4$ is regarded. It has 2 inequivalent atoms, of which the atom at position A contains the 1s vacancy (see left panel in Fig. 5.2). As can be seen from Fig. 5.3 the valence band of Cu (atomic electron configuration [Ar]$4s^1$ $3d^{10}$) is dominated by the 3d-states with small admixtures of 4s- and 4p-states. Thus, the total DOS is widely identical to the 3d-DOS. Figure 5.5 compares the total DOS of the two inequivalent atoms in the 4-atomic supercell to the total DOS of Cu and Zn.
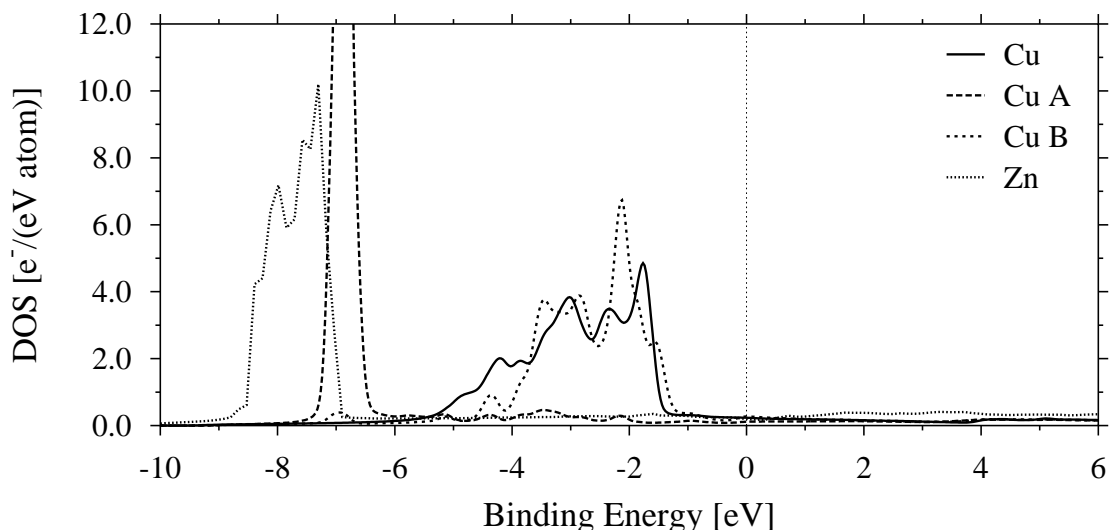
Figure 5.5: The total DOS of the two inequivalent atoms in the 4-atomic cell with core hole together with the total DOS of Cu and Zn.

The neutral atom in the supercell (position B) has a total DOS similar to the total DOS of standard Cu. This indicates that the screeening is strong and that the atomic neighbours of the ionized atom remain widely unaffected by the 1s core hole. The ionized atom in the supercell (postion A) in contrast has a DOS similar to the DOS of Zn, as is expected from the Z+1 approximation.

5.4 Treatment of the Excited Electron

The excited 1s electron can be treated in two different ways. It either can be thought to be removed from the crystal, leading to a charged supercell, or the electron can be promoted into a bound state at E_{F}, resulting in a neutral supercell. Neutral cells have one valence electron per unit cell more than charged ones. Therefore, in neutral cells the binding energies are larger than in charged ones, since E_{F} is slightly shifted to higher energies. This can be demonstrated by observing the total DOS of atoms without a core hole (see Fig. 5.6). In charged supercells the total DOS of the neutral atoms retain their positions relative to the Fermi energy (corresponding to 0 eV binding energy in the figures) if the size of the cell increases. In neutral cells
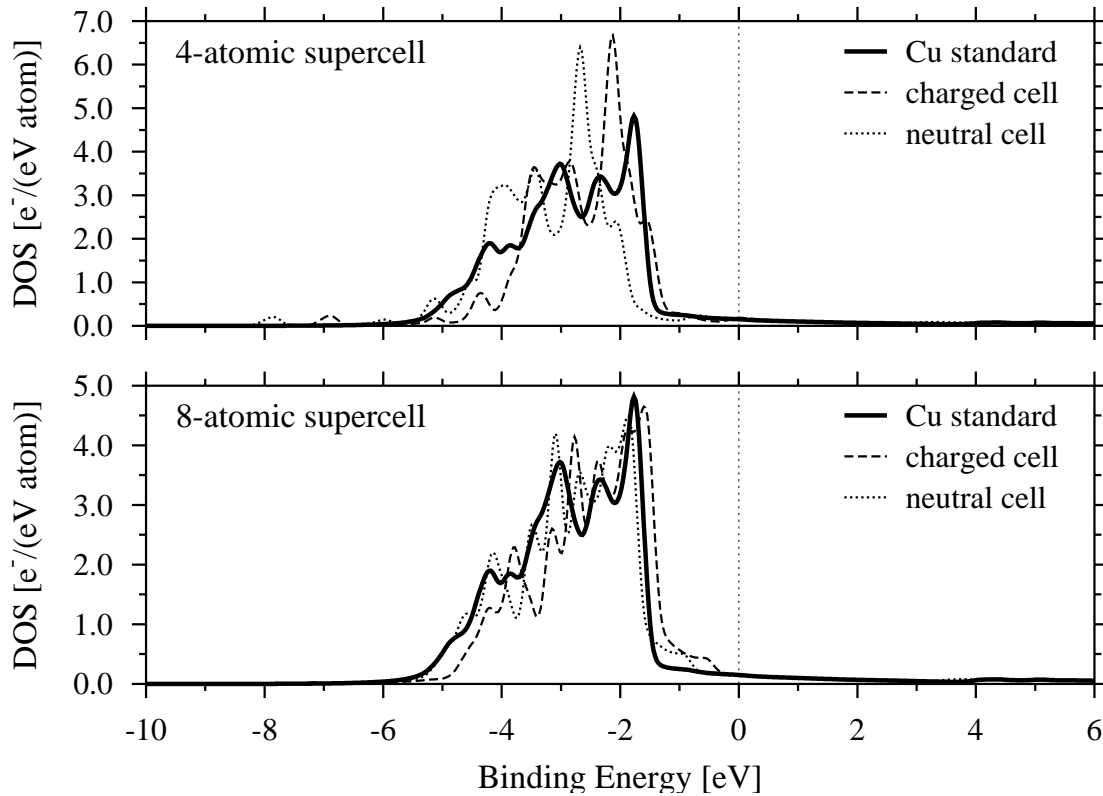
Figure 5.6: d-DOS of the neutral atoms with the largest distane to the ionized atoms in charged and neutral cells with 4 and 8 atoms.

on the other hand, the total DOS of the neutral atoms exhibits shifts towards lower binding energies with increasing cell size, since the additional electron is subdivided beween more atoms. For infinitively large cells the difference between charged and neutral supercells vanishes. Aside from the shift, the DOS of charged and neutral cells containing 8 atoms have identical shape, whereas in the supercell with 4 atoms the shape of the DOS exhibits only minor differences.

In reality, the excited electron is delocalized and therefore it is distributed over the whole crystal. Thus, in the case of small supercells a charged cell is more realistic than a neutral cell. Therefore, in what follows the considerations are restricted to charged cells.

5.5   Convergence of the DOS with Increasing Size of the Supercell

As was shown in Section 5.3 the 3d-DOS of the ionized atom shifts from a binding energy of -3 eV to an energy of -7 eV upon the appearance of the core hole. With increasing size of the charged supercell the 3d-DOS of the ionized atom further shifts to higher binding energies, as shown in Fig. 5.7. Moreover, the width of the 3d band decreases, since the 3d-states become more core-like as they shift to larger binding
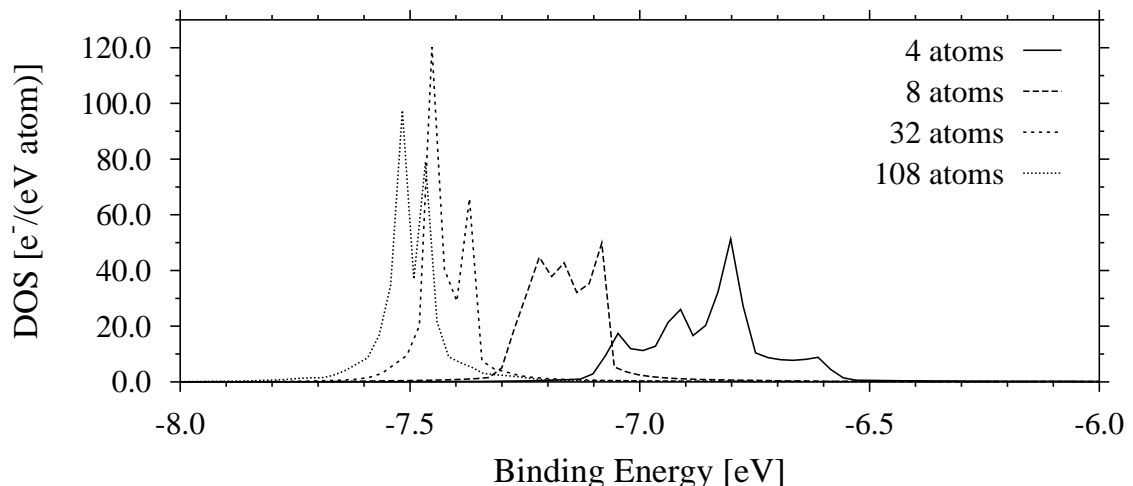
Figure 5.7: 3d-DOS of ionized atoms in charged supercells.

energies. The 3d amplitude increases simultaneously, keeping the total number of 3d-states constant. The energetic positions, the width, and the occupation of the 3d-DOS for the supercells with 4, 8, 32, and 108 atoms are summarized in Tab. 5.3. The marginal difference between the two largest supercells indicates that convergence is reached at a cell size of 108 atoms.

Compared to the 3d-DOS (see Fig. 5.5), the 4p- and 4s-DOS of the ionized atom are relatively unaffected by the presence of the 1s core hole, as shown in Fig. 5.8. However, concerning the size of the supercell, the 4p- and 4s-DOS show the same convergence behavior, as the 3d-states. In the case of the 4s- ans 4p-states the energetic shifts result in a change of the shape, which for the s-DOS is much stronger than for the p-DOS due to the larger delocalization of the latter. Remarkably, above E_F both partial DOS show only minor changes.

This convergence behaviour found for the DOS of the ionized atom can also be observed in the partial DOS of the neutral atoms in the supercell. As the size of the supercell increases, the DOS of different neutral atoms become more similar. In the case of the larger cells they perfectly resemble the respective DOS of the standard Cu. Apparently the screening of the core hole is completed at the ionized atom. The d-DOS of the neutral atoms are depicted in Fig. 5.9, whereas the p- and s-DOS are reproduced in Appendix A. To eliminate the spikes due to the small number of $\vec{k}$-points in the irreducible wedge of the Brillouin zone, the DOS have

supercell	pos [eV]	width [eV]	occupation [e$^-$/atom]
4 atoms	-6.85	0.46	9.01
8 atoms	-7.16	0.21	9.05
32 atoms	-7.41	0.13	9.04
108 atoms	-7.48	0.10	9.04

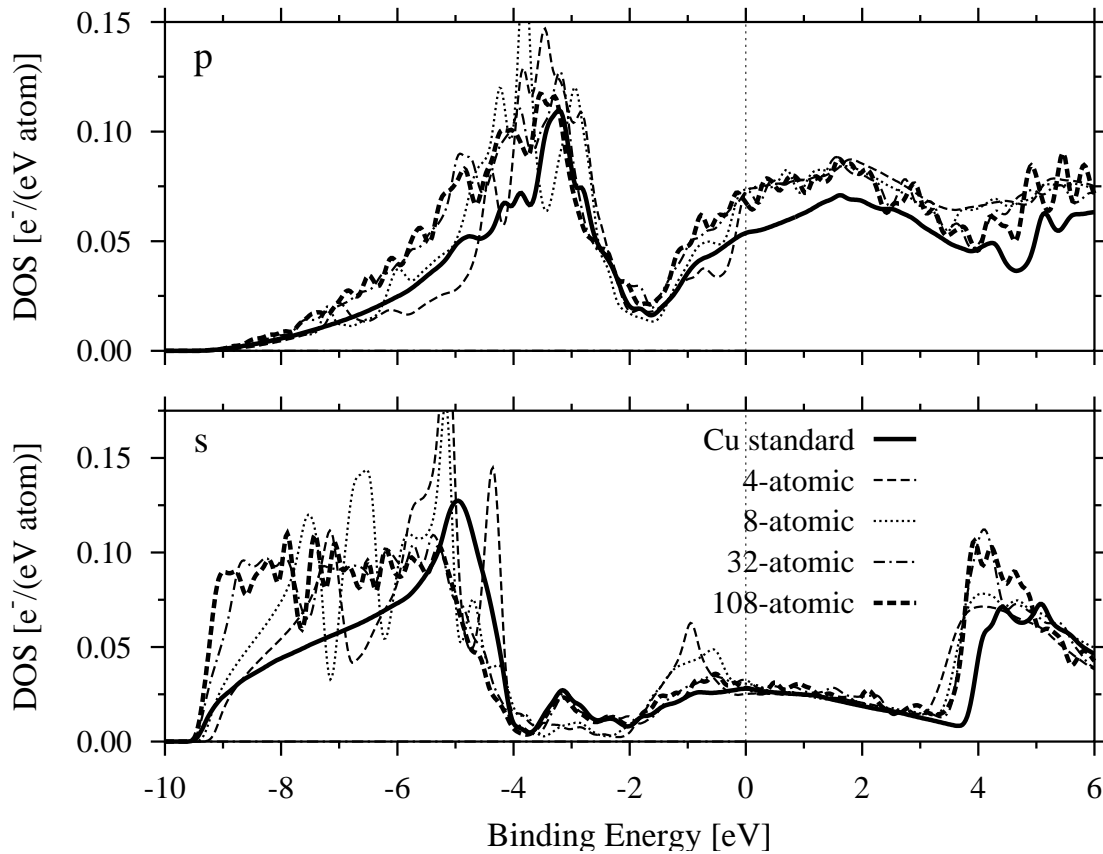Table 5.3: Parameters of the 3d-DOS of ionized atoms in charged supercells.

Figure 5.8: The 4p- and 4s-DOS of the ionized atom in charged supercells. The oscillations in the DOS of the supercell containing 108 atoms are due to the small number of $\vec{k}$-points available for the integration over the Brillouin zone.

been broadened by a Gaussian of a FWHM of 0.2 eV. Apparently the differences between the supercells containing 32 and 108 atoms are almost negligible, indicating that 108 atoms in a supercell are sufficient to treat the screening of the 1s core hole in Cu.

Moreover, the small peaks at about -7 eV, originating from the hybridization between 3d-orbitals of the ionized atom with its nearest neighbour atoms, becomes weaker as the supercell becomes larger. The same behaviour is observed in the 4p- and 4s-orbitals (see App. A).

Finally, the dramatic increase of the number of iterations from 23 in the case of 32 atoms to 50 in the case of 108 atoms in the supercell indicates the arrival at convergence. Within the supercell containing 108 atoms the distance between the ionized atoms is so large, that the attractive force of the core hole does not reach the neutral atoms that are most distant from the ionized ones. This gives rise to instabilities of the convergence process similar to the charge fluctuations in the case of supercells without a core hole. These fluctuations result in an extraordinary increase of the number of iterations needed to reach convergence, as described in Section 5.1.
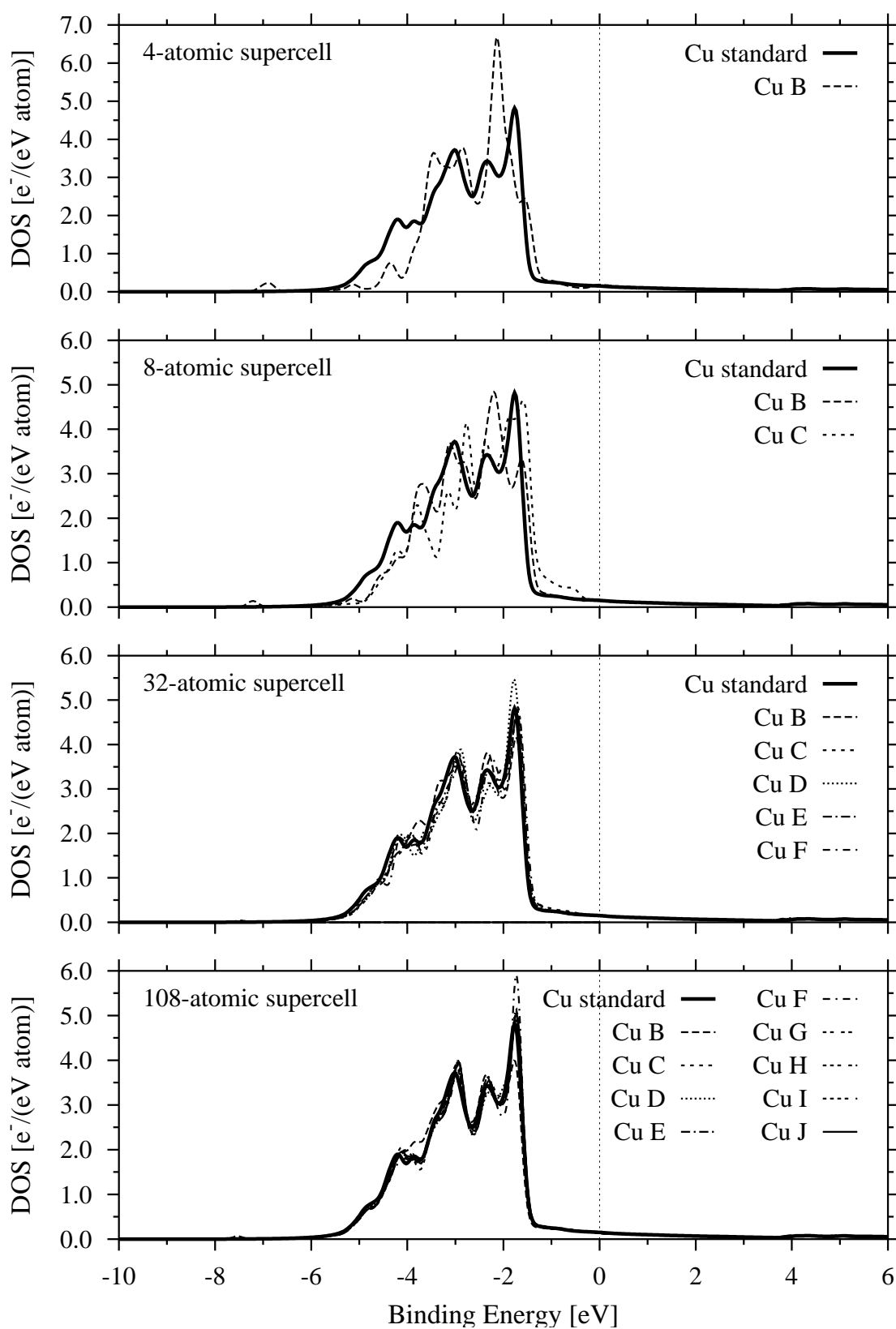
Figure 5.9: 3d-DOS of neutral atoms in charged supercells. The small peaks at about -7 eV are due to hybridization with 3d-states of the ionized atom.

5.6 Influence of the 1s Core Hole on the other Core States

The shift of the electronic states to higher binding energies due the screening of the core hole cannot only be observed in the 3d-states dominating the valence band, but also in the core states. The 1s core hole is mainly screened by the innermost shells of the atom, indicated by the large energy shifts induced by the core hole. Table 5.4 summarizes the binding energies as obtained from the standard calculation of Cu and compares them to the values found for the supercells. For the latter, the energetic shifts with respect to the standard calculation are given for both the ionized atom and for the most distant neutral atom. All energies are in Rydberg units. The energies of the spin-orbit split states 2p and 3p have been obtained from a weighted average of the two sub-states.

	1s	2s	2p	3s	3p	
standard	650.262	77.965	67.278	8.297	5.160	E [Ry]
4 atoms	24.394	4.960	6.028	0.652	0.670	ΔE [Ry]
8 atoms	24.412	4.980	6.049	0.673	0.691	of the
32 atoms	24.426	4.996	6.064	0.688	0.707	ionized
108 atoms	24.430	5.000	6.068	0.693	0.711	atom
4 atoms	-0.053	-0.056	-0.055	-0.060	-0.059	ΔE [Ry]
8 atoms	-0.031	-0.033	-0.033	-0.034	-0.031	of the most
32 atoms	-0.017	-0.018	-0.018	-0.019	-0.018	distant
108 atoms	-0.013	-0.014	-0.014	-0.015	-0.015	neutral atom

Table 5.4: Binding energies of the core states in the standard calculation and in charged supercells. The upper and lower panel contain the energies of the ionized atom and of the most distant neutral atom, respectively. The energies are given as eneregy differences with respect to the Cu standard calculation. All energies are given in Rydberg units.

The binding energies for the ionized atoms are shifted towards larger values and show a convergence behaviour, as expected, whereas the orbital energies of the most distant neutral atom converge towards the energies of the standard Cu calculation.

As in the case of the valence DOS, not only the parameters of the most distant neutral atom converge towards the values of the standard calculation. Indeed, the binding energies in all neutral atoms converge towards the standard values, as is depicted in Fig. 5.10. A similar convergence behaviour is found for the other core orbitals.

Moreover, from the difference of the total energies per atom the ionization energy E_{io} of the 1s electron can be calculated:

$$E_{\mathrm{io}}(1s) = E_{\mathrm{tot}}(\text{supercell})/N_{\mathrm{atom}} - E_{\mathrm{tot}}(\text{standard}). \qquad (5.1)$$

Figure 5.10: Convergence of the 1s orbital energies in neutral atoms with increasing cell size.
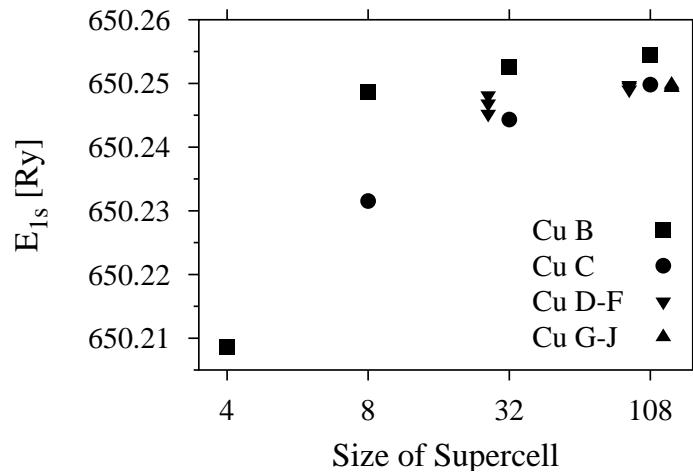
All supercells yield the same 1s ionization energy $E_{io}(1s) = 9006$ eV, which is 0.3 % larger than the actual value of 8979 eV. In contrast, the 1s orbital energy is 8843 eV which is 1.6 % smaller than 8979 eV. Thus, the consideration of screening effects within a supercell approach gives a better result than the frozen core approximation.

5.7 XANES Calculated from Supercells

To estimate the influence of the core hole on the RIXS process, the XANES of the Cu K edge is calculated from the DOS of the ionized atom as obtained in the supercell calculation.

As will be shown in the next chapter, the dipolar 1s→4p and the quadrupolar 1s→3d processes may contribute to the absorption process. The absorption intensity is proportional to the partial DOS multiplied by the repective matrix element ME. Since the p- and d-DOS are of similar size in the region of the unoccupied states, while quadrupolar transitions are roughly two orders of magnitude smaller than dipolar transtitions, only the dipolar 1s→4p contribution has to be considered. To account for the finite lifetime of the intermediate state the absorption spectrum $\text{DOS} \cdot \text{ME}$ is convoluted with a Lorentzian of FWHM $= \Gamma_0 = 1.55$ eV [Zsch89].

For excitation energies high above the absorption edge, the additional broadening due to the finite lifetime of the excited electron has to be accounted for. According to Müller *et al.* [Müll82] this can be done by means of an energy dependent width of the Lorentzian:

$$\Gamma(E) = \Gamma_0 + 0.1E\,[\text{eV}], \tag{5.2}$$

where E is the difference between the incident energy $\hbar\omega_1$ and the energy of the absorption edge.

In Fig. 5.11 the Cu K XANES spectra obtained from the standard calculation and from the charged supercell with 108 atoms are compared to the measured K XANES of Cu. The agreement of both the calculated spectra and the measured spectrum is satisfying. However, the second peak at about 6 eV (marked by the arrow),
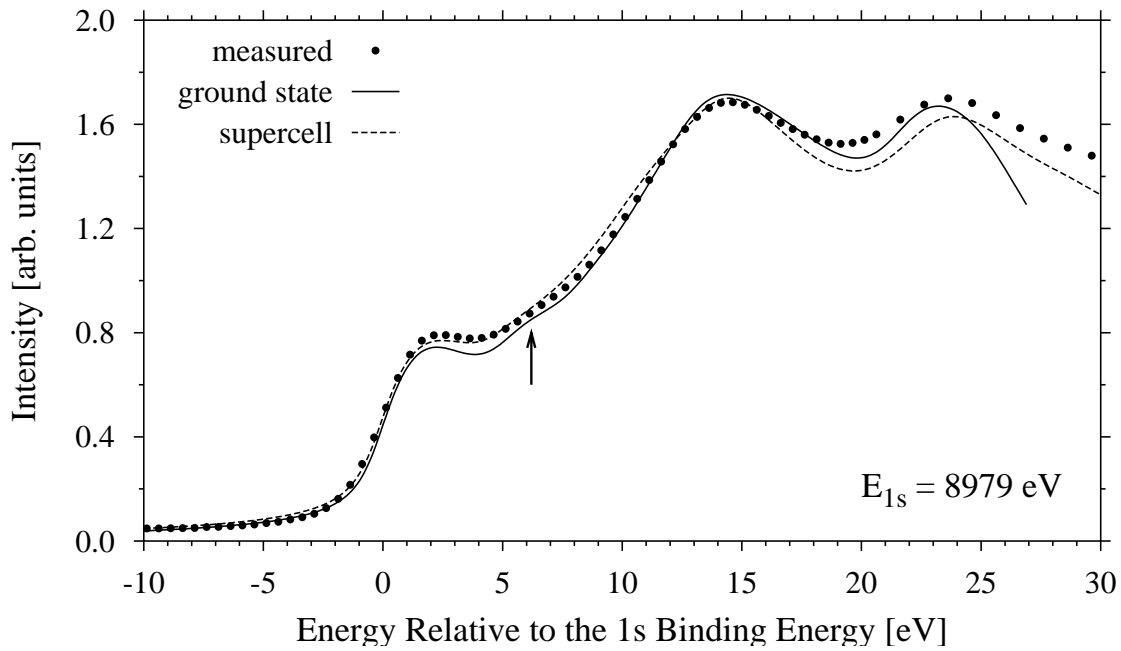
Figure 5.11: XANES spectrum of the Cu K edge obtained from the standard calculation and from the charged supercell with 108 atoms compared to the measured XANES spectrum of Cu.

which is overestimated in the calculation from the ground state DOS, is damped in the spectrum obtained from the supercell. Thus, the agreement with the measured XANES is only slightly affected by the consideration of the core hole.

Conclusion

In this chapter the supercell method for the consideration of core holes was described in detail. Special attention was paid to the convergence behaviour of the DOS with increasing cell size. It was demonstrated that the 1s core hole of 3d elements is mainly screened by the core states (see Tab. 5.4) and by the 3d-electrons of the ionized atom (see Fig. 5.5), due to their strong localization. The 4p and the 4s-DOS of the ionized atom exhibit only minor changes due to the core hole (see Fig. 5.8), whereas the DOS of the neighbouring atoms remain largely unaffected (see Fig. 5.9). Since the K-XANES predominantly monitors the 4p-DOS, the core hole has only little influence on the shape of the Cu K edge.

Thus, only a small effect of the core hole on RIXS is to be expected. Therefore in the absorption part of RIXS the core hole will be neglected from now on and the ground state band structure will be used in the calculation of both the emission and the absorption part of the RIXS process.

Chapter 6

The Contribution of Quadrupolar Transitions

So far the $\vec{A} \cdot \vec{p}$ scattering operator has been accouted for within the dipole approximation. However, in the case of the 3d transition metals, as already mentioned in Chapter 3, also quadrupolar transitions have to be considered. In Cu for example the eleven valence electrons subdivide into 10 3d, 0.6 4p, and 0.4 4s electrons, as was found out from the band structure calculation by integrating the occupied partial densities of states. If one assumes a quadrupolar transition matrix element to be two orders of magnitude smaller than a dipolar matrix element, the 3d→1s quadrupolar transition in the valence fluorescence line is only a factor of six less intense than the 4p→1s dipolar transition. Due to their different degree of localization, the 3d- and 4p-states give rise to densities of states that strongly differ in shape (see Chapter 5). Therefore, the relative intensity of dipolar and quadrupolar transitions influences the shape of valence fluorescence spectra, and thus must be properly accounted for. However, the absorption process in the case of Cu is not influenced by quadrupolar transitions, since in the conduction band the 3d-DOS is not large enough to compensate the small quadrupolar matrix element.

Moreover, radiative transitions show a characteristic angular behaviour. In the case of a dipolar transition the intensity depends on the orientation of the photon's polarization vector relative to the crystal axes of the sample. Quadrupolar transitions additionally depend on the orientation of the photon wave vector with respect to the crystal axes [Dräg84, Dräg88]. However, in the case of a cubic crystal lattice the angular dependence of dipolar transitions involving a core state with $l = 0$ vanishes, since the p-states are degenerate in a cubic system. Only the angular dependence of the quadrupolar transitions persists. This will be discussed in Section 6.7.

In the case of the 3d transition metals the 4p- and 3d-states are indistinguishably mingled in the valence fluorescence line. Fortunately, as the atomic number Z is increased from 29 (Cu) to 33 (As), the binding energy of the 3d states increases from a few eV to several tens of electron volts. Therefore, the quadrupolar fluorescence line more and more separates from the valence line with increasing atomic number, as is shown in Fig. 6.1. Due to the separation of the 3d→1s quadrupolar peak from the 4p→1s dipolar peak both transitions can be measured independently in As, Ge, and Ga. This offers the opportunity to calculate the relative fluorescence intensities of the quadrupolar transitions and to compare them to the measured

spectra. Then the quadrupolar contribution to the valence fluorescence spectra of Cu can be properly accounted for, improving the agreement between measured and calculated spectra.
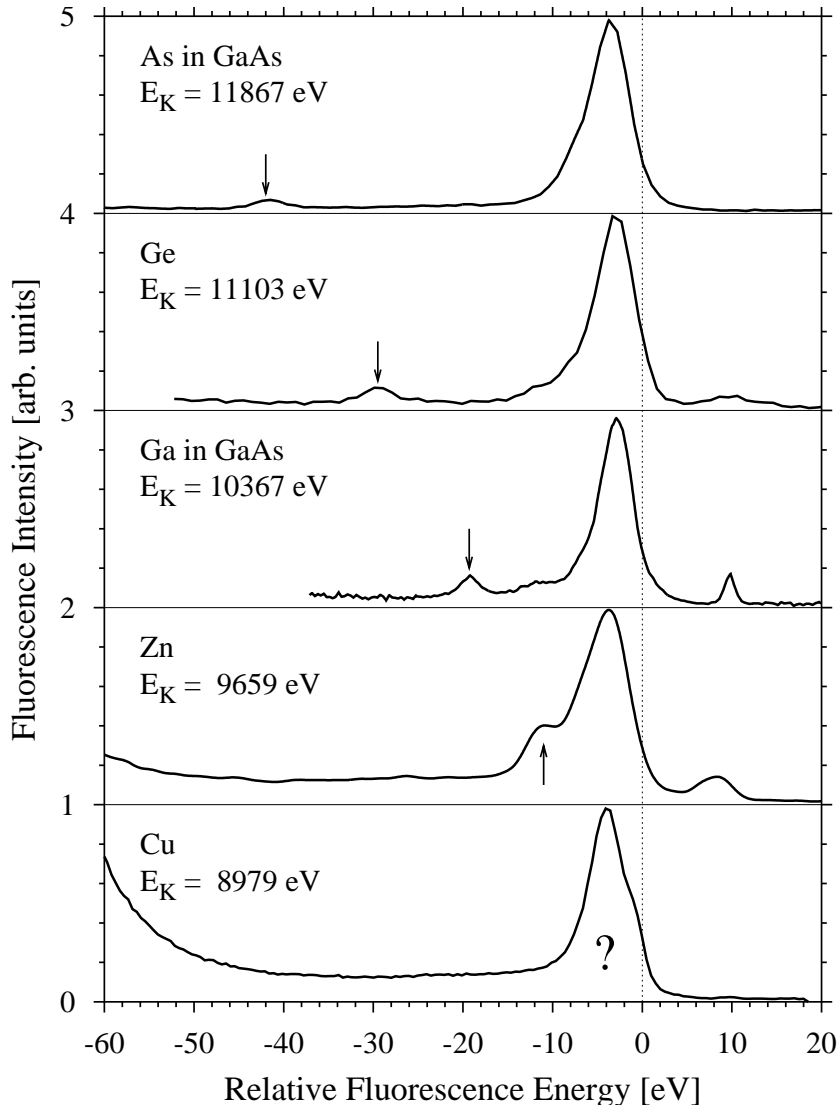

Figure 6.1: Measured dipolar and quadrupolar valence fluorescence lines. The fluorescence energies are relative to the respective 1s binding energy E_K, indicated for each element. The valence fluorescence lines are found in the range of -10 to 0 eV. The peaks at energies above zero are due to quasi elastic scattering, except for Ge where it is a satellite due to a double electron excitation during the absorption process [Ster00]. For the elements Cu and Zn the high energy tail of the $K\beta_{1,3}$ line is visible at low energies. The dispersing low energy feature from As to Zn marked by the arrow is due to the 3d→1s quadrupolar transition. In the case of Cu the quadrupolar line is mingled into the dipolar fluorescence line. The spectra have been measured at beamlines ID16 (Ga, As, Cu) and ID28 (Ge) of the ESRF and at beamline G3 of the HASYLAB (Zn).

6.1 Dipole and Quadrupole Operator

First the dipole and the quadrupole operator will be derived from the $\vec{A} \cdot \vec{p}$ term of the interaction Hamiltonian (see for example Eq. 1.15). Expansion of the exponential up to first order in $\vec{k} \cdot \vec{r}$ yields

$$
\begin{aligned}
\langle f| \, e^{i\vec{k} \cdot \vec{r}} (\hbar \hat{\epsilon} \cdot \vec{\nabla}) \, |i\rangle &\simeq \langle f| \, (1 + i\vec{k} \cdot \vec{r})(\hbar \hat{\epsilon} \cdot \vec{\nabla}) \, |i\rangle \\
&= \langle f| \, \hbar \hat{\epsilon} \cdot \vec{\nabla} \, |i\rangle + \langle f| \, i\hbar \, \vec{k} \cdot \vec{r} \, \hat{\epsilon} \cdot \vec{\nabla} \, |i\rangle .
\end{aligned} \tag{6.1}
$$

To obtain the electric dipole operator, only the zeroth order is needed. Making use of the equation of motion of $\vec{p}$

$$
\vec{p} = -i\hbar \vec{\nabla} = \frac{m}{i\hbar} [\vec{r}, H_0] \tag{6.2}
$$

the momentum operator $\vec{p}$ in the matrix element can be replaced by $\vec{r}$:

$$
\begin{aligned}
\langle f| \, \hbar \hat{\epsilon} \cdot \vec{\nabla} \, |i\rangle &= \frac{m}{\hbar} \langle f| \, \hat{\epsilon} \cdot (\vec{r} H_0 - H_0 \vec{r}) \, |i\rangle \\
&= -\frac{m(E_f - E_i)}{\hbar} \langle f| \, \hat{\epsilon} \cdot \vec{r} \, |i\rangle \\
&= -m\omega \, \langle f| \, \hat{\epsilon} \cdot \vec{r} \, |i\rangle .
\end{aligned} \tag{6.3}
$$

Similarly the first order part of the expansion can be treated using the identity [Brou90]

$$
\hbar \, \vec{k} \cdot \vec{r} \, \hat{\epsilon} \cdot \vec{\nabla} = \frac{m}{2\hbar} \left[\hat{\epsilon} \cdot \vec{r} \, \vec{k} \cdot \vec{r}, H_0 \right] + \frac{i}{2} (\vec{k} \times \hat{\epsilon}) \cdot \vec{L}, \tag{6.4}
$$

leading to the transition amplitude $A_{i,f}$ up to first order as

$$
A_{i,f} = -m\omega \, \langle f| \, \hat{\epsilon} \cdot \vec{r} \, |i\rangle - i\frac{m\omega}{2} \langle f| \, \hat{\epsilon} \cdot \vec{r} \, \vec{k} \cdot \vec{r} \, |i\rangle - \frac{1}{2} \langle f| \, (\vec{k} \times \hat{\epsilon}) \cdot \vec{L} \, |i\rangle . \tag{6.5}
$$

The third term, that contributes to magnetic dipole transitions, does not contain a radial variable. It therefore vanishes if $|i\rangle$ and $|f\rangle$ are orthogonal as it is the case for x-ray emission and absorption. Thus, only the first and second term persist. Further there are no interference terms between the first and the second term since $(a + ib)(a + ib)^* = a^2 + b^2$. Hence the intensity I of the transition is given by

$$
I = A_{i,f} A_{i,f}^* \propto |\langle f| \, \hat{\epsilon} \cdot \vec{r} \, |i\rangle|^2 + \frac{1}{4} \left| \langle f| \, \hat{\epsilon} \cdot \vec{r} \, \vec{k} \cdot \vec{r} \, |i\rangle \right|^2 , \tag{6.6}
$$

where the first and second part describe the electric dipole and the electric quadrupole transitions, respectively. By means of this formula the relative intensities of the dipole and the quadrupole transitions between the states $|i\rangle$ and $|f\rangle$ can be calculated.

6.2 Radial and Angular Part of the Matrix Elements

Assuming that the wave functions $|i\rangle$ and $|f\rangle$ can be described by atomic wave functions, consisting of a radial function $R(r)$ and of a spherical harmonic $Y_l^m(\hat{r})$,

$$|i\rangle = R_{l_0}(r)Y_{l_0}^{m_0}(\hat{r}) \quad \text{and} \quad |f\rangle = R_l(r)Y_l^m(\hat{r}), \tag{6.7}$$

the dipole matrix element M_D can be split into an angular integral M_D^A and a radial integral M_D^R:

$$
\begin{aligned}
M_D &= \langle f| \,\hat{\epsilon} \cdot \vec{r}\,|i\rangle = \int d\vec{r}\, R_l(r)Y_l^{m*}(\hat{r})\, \hat{\epsilon} \cdot \vec{r}\, R_{l_0}(r)Y_{l_0}^{m_0}(\hat{r}) \\
&= \underbrace{\int d\Omega\, Y_l^{m*}(\hat{r})\, \hat{\epsilon} \cdot \hat{r}\, Y_{l_0}^{m_0}(\hat{r})}_{M_\mathrm{D}^\mathrm{A}}\ \underbrace{\int r^2 dr\, R_l(r)\, r\, R_{l_0}(r)}_{M_\mathrm{D}^\mathrm{R}}.
\end{aligned}
\tag{6.8}
$$

The same splitting applies to the quadrupole matrix element M_Q:

$$
\begin{aligned}
M_\mathrm{Q} &= \langle f| \,\hat{\epsilon} \cdot \vec{r}\, \vec{k} \cdot \vec{r}\,|i\rangle = \int d\vec{r}\, R_l(r)Y_l^{m*}(\hat{r})\, \hat{\epsilon} \cdot \vec{r}\, \vec{k} \cdot \vec{r}\, R_{l_0}(r)Y_{l_0}^{m_0}(\hat{r}) \\
&= \underbrace{\int d\Omega\, Y_l^{m*}(\hat{r})\, \hat{\epsilon} \cdot \hat{r}\, \hat{k} \cdot \hat{r}\, Y_{l_0}^{m_0}(\hat{r})}_{M_\mathrm{Q}^\mathrm{A}}\ k \underbrace{\int r^2 dr\, R_l(r)\, r^2\, R_{l_0}(r)}_{M_\mathrm{Q}^\mathrm{R}}.
\end{aligned}
\tag{6.9}
$$

Then the total transition intensity is given by

$$
\begin{aligned}
I &= M_\mathrm{D}M_\mathrm{D}^* + \frac{1}{4}M_\mathrm{Q}M_\mathrm{Q}^* \\
&= M_\mathrm{D}^\mathrm{A}M_\mathrm{D}^{\mathrm{A}*}\,(M_\mathrm{D}^\mathrm{R})^2 + \frac{k^2}{4}M_\mathrm{Q}^\mathrm{A}M_\mathrm{Q}^{\mathrm{A}*}\,(M_\mathrm{Q}^\mathrm{R})^2.
\end{aligned}
\tag{6.10}
$$

From the angular integrals the selection rules and the angular dependencies of the transitions arise, whereas the radial integrals, containing the radial wave functions, determine the intensity of the transition.

In the following sections the angular and the radial integral will be calculated separately to yield the intensity of the 3d→1s quadrupolar transition relative to the 4p→1s dipolar transition.

6.3 The Angular Integrals

Although it is possible to express the spherical harmonics Y_l^m in terms of the polar coordinates θ and ϕ (see Fig. 6.6) and to calculate the respective integrals, it is more concise and easier to use the formalism of the spherical harmonics. This derivation is based on the detailed article by C. Brouder [Brou90]. First, the necessary formulae are listed.

1. The orthonormality of the spherical harmonics, Eq. 3.139 of [Bied81]:

$$\int d\Omega \, Y_{l_1}^{m_1*}(\hat{r}) \, Y_{l_2}^{m_2}(\hat{r}) = \delta_{l_1,l_2} \, \delta_{m_1,m_2}. \tag{6.11}$$

2. The scalar product expressed in terms of spherical harmonics:

$$\hat{a} \cdot \hat{b} = \frac{4\pi}{3} \sum_\lambda Y_1^{\lambda*}(\hat{a}) Y_1^\lambda(\hat{b}). \tag{6.12}$$

3. Gaunt's integral over three spherical harmonics, Eq. 3.192 of [Bied81] or Eq. 4.34 of [Rose57]:

$$\int d\Omega \, Y_l^{m*}(\hat{r}) \, Y_{l_1}^{m_1}(\hat{r}) \, Y_{l_2}^{m_2}(\hat{r})$$

$$= \left[\frac{(2l_1+1)(2l_2+1)}{4\pi(2l+1)}\right]^{\frac{1}{2}} (l_1 0 \, l_2 0|l0) \; (l_1 m_1 l_2 m_2|lm) \tag{6.13}$$

$$= \langle l\|l_1\|l_2\rangle \, (l_1 m_1 l_2 m_2|lm) \tag{6.14}$$

$$= C^{l \; m}_{l_1 m_1 \; l_2 m_2}. \tag{6.15}$$

Therein denote:

$(l_1 0 \, l_2 0 \, |l0)$ and $(l_1 m_1 l_2 m_2|lm)$ the Wigner or Clebsch-Gordan coefficients,
$\langle l\|l_1\|l_2\rangle$ the reduced matrix element, and
$C^{l \; m}_{l_1 m_1 \; l_2 m_2}$ the Gaunt coefficient.

4. The expansion of a product of spherical harmonics in terms of spherical harmonics, Eq. 3.436 of [Bied81] or Eq. 4.32 of [Rose57]:

$$Y_1^\lambda(\hat{r}) \, Y_1^\mu(\hat{r}) = \sum_{n\nu} C^{n \, \nu}_{1\lambda \; 1\mu} \, Y_n^\nu(\hat{r})$$

$$= \sum_\nu C^{2 \, \nu}_{1\lambda \; 1\mu} \, Y_2^\nu(\hat{r}) + C^{0 \, 0}_{1\lambda \; 1\mu} \, Y_0^0(\hat{r}) \tag{6.16}$$

$$Y_1^{\lambda*}(\hat{r}) \, Y_1^{\lambda'}(\hat{r}) = \sum_{a\alpha} C^{1\lambda}_{1\lambda' \; a\alpha} \, Y_a^{\alpha*}(\hat{r})$$

$$= \sum_\alpha C^{1\lambda}_{1\lambda' \; 2\alpha} \, Y_2^{\alpha*}(\hat{r}) + C^{1\lambda}_{1\lambda' \; 00} \, Y_0^{0*}(\hat{r}) \tag{6.17}$$

Here the triangle condition of the Gaunt coefficients for l_1, l_2, l has been used:

$$C^{lm}_{l_1 m_1 \, l_2 m_2} = 0 \quad \begin{array}{ll} \text{unless} & l \in \{l_1 + l_2, l_1 + l_2 - 1, \ldots, |l_2 - l_1|\} \\ \text{and} & l_1 + l_2 + l = \text{even}, \end{array} \tag{6.18}$$

(see Eq. 3.191 and Eq. 3.195 in [Bied81]).

The Wigner coefficients can be calculated by means of Eq. 3.171 in [Bied81].

6.3.1   The Angular Integral of the Dipole Operator

First the scalar product $\hat{\epsilon} \cdot \hat{r}$ is expressed in terms of the spherical harmonics (see Eq. 6.12), leading to an integral over three spherical harmonics:

$$
\begin{aligned}
M_{\mathrm{D}}^{\mathrm{A}} &= \int d\Omega \, Y_l^{m*}(\hat{r}) \, \hat{\epsilon} \cdot \hat{r} \, Y_{l_0}^{m_0}(\hat{r}) \\
&= \frac{4\pi}{3} \sum_\lambda \int d\Omega \, Y_l^{m*}(\hat{r}) \, Y_1^{\lambda*}(\hat{\epsilon}) \, Y_1^{\lambda}(\hat{r}) \, Y_{l_0}^{m_0}(\hat{r}),
\end{aligned} \tag{6.19}
$$

which can be evaluated using Gaunt's Integral (6.15):

$$
M_{\mathrm{D}}^{\mathrm{A}} = \frac{4\pi}{3} \sum_\lambda C_{l_0 \, m_0 \, 1\, \lambda}^{l \ m} \, Y_1^{\lambda*}(\hat{\epsilon}) \ . \tag{6.20}
$$

Now one can calculate the square of the matrix element

$$
|M_{\mathrm{D}}^{\mathrm{A}}|^2 = M_{\mathrm{D}}^{\mathrm{A}} M_{\mathrm{D}}^{\mathrm{A}*} = \left(\frac{4\pi}{3}\right)^2 \sum_{lm} \sum_{l'm'} \sum_{\lambda\lambda'} C_{l_0 \, m_0 \, 1\, \lambda}^{l \ m} \, C_{l_0 \, m_0 \, 1\, \lambda'}^{l' \ m'} \, Y_1^{\lambda*}(\hat{\epsilon}) \, Y_1^{\lambda'}(\hat{\epsilon}), \tag{6.21}
$$

and expand the product of the spherical harmonics of $\hat{\epsilon}$ making use of (6.17):

$$
\begin{aligned}
|M_{\mathrm{D}}^{\mathrm{A}}|^2 &= \left(\frac{4\pi}{3}\right)^2 \sum_{lm} \sum_{l'm'} \sum_{\lambda\lambda'} C_{l_0 \, m_0 \, 1\, \lambda}^{l \ m} \, C_{l_0 \, m_0 \, 1\, \lambda'}^{l' \ m'} \sum_{a\alpha} C_{1\,\lambda' \, a\,\alpha}^{1\,\lambda} \, Y_a^{\alpha*}(\hat{\epsilon}) \\
&= \left(\frac{4\pi}{3}\right)^2 \sum_{lm} \sum_{l'm'} \sum_{\lambda\lambda'} C_{l_0 \, m_0 \, 1\, \lambda}^{l \ m} \, C_{l_0 \, m_0 \, 1\, \lambda'}^{l' \ m'} \, C_{1\,\lambda' \, 0\,0}^{1\,\lambda} \, Y_0^{0*}(\hat{\epsilon}) \\
&\quad + \left(\frac{4\pi}{3}\right)^2 \sum_{lm} \sum_{l'm'} \sum_{\lambda\lambda'} C_{l_0 \, m_0 \, 1\, \lambda}^{l \ m} \, C_{l_0 \, m_0 \, 1\, \lambda'}^{l' \ m'} \sum_{\alpha} C_{1\,\lambda' \, 2\,\alpha}^{1\,\lambda} \, Y_2^{\alpha*}(\hat{\epsilon}). \tag{6.22}
\end{aligned}
$$

The first and second addend of Eq. 6.22 describe the isotropic and the polarization dependent part of the dipole transition intensity, respectively. For case in question here, i.e. RIXS at the K edge of a cubic substance, the anisotropic part of the transition probability vanishes (see Section 6.7). Therefore, only the first addend is considered further.

Now one can apply the triangle condition of the Gaunt coefficients for m_1, m_2, m :

$$
C_{l_1 \, m_1 \, l_2 \, m_2}^{l \, m} = 0 \quad \text{unless} \quad m_1 + m_2 = m \tag{6.23}
$$

to the third Gaunt coefficient in Eq. 6.22. It follows that λ must equal λ'. Since in every l, m-pair $|m| \leq l$, λ can take only the values $-1, 0, 1$.

With $C_{1\,\lambda' \, 0\,0}^{1\,\lambda} = \frac{1}{\sqrt{4\pi}} \ \forall \lambda$ and $Y_0^{0*}(\hat{\epsilon}) = \frac{1}{\sqrt{4\pi}}$ one finds that

$$
C_{1\,\lambda' \, 0\,0}^{1\,\lambda} \, Y_0^{0*}(\hat{\epsilon}) = \frac{1}{4\pi} \delta_{\lambda,\lambda'}. \tag{6.24}
$$

Moreover, from $\lambda = \lambda'$ it follows, by applying the triangle conditions, that $l = l'$ and $m = m'$ thus reducing Eq. 6.22 to:

$$
\begin{aligned}
|M_{\mathrm{D}}^{\mathrm{A}}|^2 &= \left(\frac{4\pi}{3}\right)^2 \sum_{lm} \sum_{\lambda\lambda'} C^{l\ m}_{l_0\,m_0\,1\,\lambda}\, C^{l\ m}_{l_0\,m_0\,1\,\lambda'}\, \frac{1}{4\pi}\delta_{\lambda,\lambda'} \\
&= \left(\frac{4\pi}{3}\right)\frac{1}{3}\sum_{lm}\sum_{\lambda}\left(C^{l\ m}_{l_0\,m_0\,1\,\lambda}\right)^2.
\end{aligned}
\tag{6.25}
$$

Applying the triangle conditions to the remaining Gaunt coefficient, the dipole selection rules can be easily deduced, yielding

$$
l = l_0 \pm 1 \qquad \text{and} \qquad m = \begin{cases} m_0 \\ m_0 \pm 1. \end{cases}
\tag{6.26}
$$

6.3.2 The Angular Integral of the Quadrupole Operator

By analogy to the treatment of the dipole operator both scalar products $\hat{\epsilon} \cdot \hat{r}$ and $\hat{k} \cdot \hat{r}$ are expressed in terms of spherical harmonics (see Eq. 6.12):

$$
\begin{aligned}
M_{\mathrm{Q}}^{\mathrm{A}} &= \int d\Omega\, Y_l^{m*}(\hat{r})\, \hat{\epsilon} \cdot \hat{r}\, \hat{k} \cdot \hat{r}\, Y_{l_0}^{m_0}(\hat{r}) \\
&= \left(\frac{4\pi}{3}\right)^2 \sum_{\lambda\mu} \int d\Omega\, Y_l^{m*}(\hat{r})\, Y_1^{\lambda*}(\hat{\epsilon})\, Y_1^{\lambda}(\hat{r})\, Y_1^{\mu*}(\hat{k})\, Y_1^{\mu}(\hat{r})\, Y_{l_0}^{m_0}(\hat{r}).
\end{aligned}
\tag{6.27}
$$

In this case one has to deal with an integral over four spherical harmonics depending on $\hat{r}$. Since only integrals over three spherical harmonics are covered by Gaunt's integral, one has to reduce the number of spherical harmonics. This can be done by using Eq. 6.16, i.e. by expanding a product of two spherical harmonics in terms of a sum of spherical harmonics:

$$
Y_1^{\lambda}(\hat{r})\, Y_1^{\mu}(\hat{r}) = \sum_{\nu} C^{2\,\nu}_{1\,\lambda\,1\,\mu}\, Y_2^{\nu}(\hat{r}) + C^{0\,0}_{1\,\lambda\,1\,\mu}\, Y_0^0(\hat{r}).
\tag{6.28}
$$

Considering the second term and imposing the triangle condition for m_1, m_2, m one finds similar to 6.24:

$$
C^{0\,0}_{1\,\lambda\,1\,\mu}\, Y_0^{0*}(\hat{r}) = \frac{1}{4\pi}\delta_{\lambda,-\mu}.
\tag{6.29}
$$

Therefore the only remaining factors containing λ and μ in Eq. 6.27 are:

$$
\begin{aligned}
\sum_{\lambda\mu} Y_1^{\lambda*}(\hat{\epsilon})\, Y_1^{\mu*}(\hat{k})\frac{1}{4\pi}\delta_{\lambda,-\mu} &= \sum_{\lambda} Y_1^{\lambda*}(\hat{\epsilon})\, Y_1^{-\lambda*}(\hat{k}) = \sum_{\lambda} Y_1^{\lambda*}(\hat{\epsilon})\, Y_1^{\lambda}(\hat{k}) \\
&= \frac{3}{4\pi}\hat{\epsilon} \cdot \hat{k} = 0 \quad \text{(with Eq. 6.12),}
\end{aligned}
\tag{6.30}
$$

since the polarization vector $\hat{\epsilon}$ is perpendicular to the wave vector $\hat{k}$ of the photon. Thus, only the first term remains and Eq. 6.27 reduces to

$$
M_{\mathrm{Q}}^{\mathrm{A}} = \left(\frac{4\pi}{3}\right)^2 \sum_{\lambda\mu\nu} \int d\Omega\, Y_l^{m*}(\hat{r})\, Y_{l_0}^{m_0}(\hat{r})\, Y_2^{\nu}(\hat{r})\, C^{2\,\nu}_{1\,\lambda\,1\,\mu}\, Y_1^{\lambda*}(\hat{\epsilon})\, Y_1^{\mu*}(\hat{k}),
\tag{6.31}
$$

which can be evaluated using Gaunt's integral (see Eq. 6.15) resulting in:

$$M_Q^A = \left(\frac{4\pi}{3}\right)^2 \sum_{\lambda\mu\nu} C^{l\ m}_{l_0\ m_0\ 2\nu}\ C^{2\nu}_{1\lambda\ 1\mu}\ Y_1^{\lambda*}(\hat{\epsilon})\ Y_1^{\mu*}(\hat{k})\ . \tag{6.32}$$

Now the square of the matrix element can be calculated:

$$
\begin{aligned}
|M_Q^A| &= M_Q^A M_Q^{A*} = \left(\frac{4\pi}{3}\right)^4 \sum_{lm}\sum_{l'm'}\sum_{\nu\nu'} C^{l\ m}_{l_0\ m_0\ 2\nu}\ C^{l'\ m'}_{l_0\ m_0\ 2\nu'} \\
&\quad \times \sum_{\lambda\lambda'}\sum_{\mu\mu'} C^{2\nu}_{1\lambda\ 1\mu}\ C^{2\nu'}_{1\lambda'\ 1\mu'} Y_1^{\lambda*}(\hat{\epsilon})\ Y_1^{\lambda'}(\hat{\epsilon})\ Y_1^{\mu*}(\hat{k})\ Y_1^{\mu'}(\hat{k})\ , \tag{6.33}
\end{aligned}
$$

whereon Eq. 6.17 can be applied. In Section 6.7 it will be shown, that for the case of the 3d→1s transitions of As, Ge, Ga, and Cu no polarization effects are to be expected. Thus, as in the case of the dipole operator, only the Y_0^0 parts of the expansions are kept and Eq. 6.24 is used to get Kronecker δ-functions for λ, λ' and μ, μ' resulting in:

$$
\begin{aligned}
|M_Q^A| &\approx \left(\frac{4\pi}{3}\right)^4 \sum_{lm}\sum_{l'm'}\sum_{\nu\nu'} C^{l\ m}_{l_0\ m_0\ 2\nu}\ C^{l'\ m'}_{l_0\ m_0\ 2\nu'} \\
&\quad \times \sum_{\lambda\lambda'}\sum_{\mu\mu'} C^{2\nu}_{1\lambda\ 1\mu}\ C^{2\nu'}_{1\lambda'\ 1\mu'}\ C^{1\lambda}_{1\lambda'\ 00}\ Y_0^{0*}(\hat{\epsilon})\ C^{1\mu}_{1\mu'\ 00}\ Y_0^{0*}(\hat{k}) \\
&= \left(\frac{4\pi}{3}\right)^4 \sum_{lm}\sum_{l'm'}\sum_{\nu\nu'} C^{l\ m}_{l_0\ m_0\ 2\nu}\ C^{l'\ m'}_{l_0\ m_0\ 2\nu'} \sum_{\lambda\lambda'}\sum_{\mu\mu'} C^{2\nu}_{1\lambda\ 1\mu}\ C^{2\nu'}_{1\lambda'\ 1\mu'}\ \frac{\delta_{\lambda,\lambda'}}{4\pi}\frac{\delta_{\mu,\mu'}}{4\pi} \\
&= \left(\frac{4\pi}{3}\right)^2 \frac{1}{9} \sum_{lm}\sum_{l'm'}\sum_{\nu\nu'} C^{l\ m}_{l_0\ m_0\ 2\nu}\ C^{l'\ m'}_{l_0\ m_0\ 2\nu'} \sum_{\lambda\mu} C^{2\nu}_{1\lambda\ 1\mu}\ C^{2\nu'}_{1\lambda\ 1\mu}\ . \tag{6.34}
\end{aligned}
$$

Again the triangle condition on m_1, m_2, m can be used to get rid of the sums over ν', m', and l', successively ending up with:

$$|M_Q^A| \approx \left(\frac{4\pi}{3}\right)^2 \frac{1}{9} \sum_{lm}\sum_{\lambda\mu\nu} \left(C^{l\ m}_{l_0\ m_0\ 2\nu}\ C^{2\nu}_{1\lambda\ 1\mu}\right)^2\ . \tag{6.35}$$

As in the case of the dipole operator the first Gaunt coefficient contains the selection rules:

$$l = \begin{cases} l_0 \\ l_0 \pm 2 \end{cases} \quad \text{with } l = l_0 = 0 \text{ forbidden and} \quad m = \begin{cases} m_0 \\ m_0 \pm 1 \\ m_0 \pm 2. \end{cases} \tag{6.36}$$

6.3.3 The Weighting Factors

With the Equations 6.25 and 6.35 the angular integrals between the states $|l_0 m_0\rangle$ and $|lm\rangle$ can be calculated for the dipole and the quadrupole operator, respectively. This yields the weighting factors $W_{l_0 m_0, lm}$ as shown in Table 6.1. They are within

| $W_D \cdot 3$ | | l_0 | 0 | 1 | 1 | 1 | 2 | 2 | 2 | 2 | 2 |
		m_0	0	-1	1	1	-2	-1	0	1	2
l	m										
0	0			$1/3$	$1/3$	$1/3$					
1	-1		$1/3$				$6/15$	$3/15$	$1/15$		
1	0		$1/3$					$3/15$	$4/15$	$3/15$	
1	1		$1/3$						$1/15$	$3/15$	$6/15$
2	-2			$6/15$							
2	-1			$3/15$	$3/15$						
2	0			$1/15$	$4/15$	$1/15$					
2	1				$3/15$	$3/15$					
2	2					$6/15$					
3	-3						$15/35$				
3	-2						$5/35$	$10/35$			
3	-1						$1/35$	$8/35$	$6/35$		
3	0							$3/35$	$9/35$	$3/35$	
3	1								$6/35$	$8/35$	$1/35$
3	2									$10/35$	$5/35$
3	3										$15/35$

| $W_Q \cdot 9$ | | l_0 | 0 | 1 | 1 | 1 | 2 | 2 | 2 | 2 | 2 |
		m_0	0	-1	1	1	-2	-1	0	1	2
l	m										
0	0						$2/15$	$2/15$	$2/15$	$2/15$	$2/15$
1	-1			$2/75$	$6/75$	$12/75$					
1	0			$6/75$	$8/75$	$6/75$					
1	1			$12/75$	$6/75$	$2/75$					
2	-2		$2/15$				$8/147$	$12/147$	$8/147$		
2	-1		$2/15$				$12/147$	$2/147$	$2/147$	$12/147$	
2	0		$2/15$				$8/147$	$2/147$	$8/147$	$2/147$	$8/147$
2	1		$2/15$					$12/147$	$2/147$	$2/147$	$12/147$
2	2		$2/15$						$8/147$	$12/147$	$8/147$
3	-3			$30/175$							
3	-2			$20/175$	$10/175$						
3	-1			$12/175$	$16/175$	$2/175$					
3	0			$6/175$	$18/175$	$6/175$					
3	1			$2/175$	$16/175$	$12/175$					
3	2				$10/175$	$20/175$					
3	3					$30/175$					

Table 6.1: Weighting factors $W_{l_0 m_0, lm}$ for dipolar (upper table) and for quadrupolar transitions (lower table).

l_0	0	1	2	3
l				
0		**1**	$^2/_3$	
1	$^1/_{\mathbf{3}}$	$^4/_{15}$	$^{\mathbf{2}}/_{\mathbf{3}}$	$^2/_5$
2	$^2/_{15}$	$^{\mathbf{2}}/_{\mathbf{5}}$	$^4/_{21}$	$^{\mathbf{3}}/_{\mathbf{5}}$
3		$^6/_{35}$	$^{\mathbf{3}}/_{\mathbf{7}}$	$^8/_{45}$

Table 6.2: Reduced weighting factors $W_{l_0,l}$ for dipolar (bold) and for quadrupolar transitions (thin).

the range of 0 to 1 if the transition is allowed and they are zero if the transition is forbidden. The weight factors for the dipole transitions also can be found in [Neck75]. The $W_{l_0 m_0, lm}$ are invariant if l and l_0 are interchanged. Thus, one is free to assign l_0 and m_0 to the core state involved in the radiative process.

If the core states with angular momentum quantum number l_0 are $2l_0 + 1$-fold degenerate, the magnetic quantum number m_0 of the core hole is not known. Hence, one has to sum over m_0 leading to weight factors $W_{l_0,lm}$ which turn out to be independent of m as well. This results in the reduced weight factors $W_{l_0,l}$ that are summarized in Table 6.2.

6.4　The Radial Integrals

According to Equations 6.8 and 6.9 the radial parts of the dipolar and the quadrupolar transition matrix elements are calculated from

$$M_{\mathrm{D}}^{\mathrm{R}} = \int r^2 \, dr \, R_l(r) \, r \, R_{l_0}(r) \quad \text{and} \quad M_{\mathrm{Q}}^{\mathrm{R}} = \int r^2 \, dr \, R_l(r) \, r^2 \, R_{l_0}(r), \qquad (6.37)$$

respectively, wherein $R_l(r)$ and $R_{l_0}(r)$ are the radial functions of the valence and of the core state, respectively. However, in the LAPW algorithm the single electron valence states are linear combinations of plane waves that within the atomic spheres are expanded in terms of atomic like wave functions with different orbital quantum numbers l as defined by Eq. 2.7 and 2.19:

$$\varphi_{i,\vec{k}}(\vec{r}) = \sum_{\vec{G}} c_{i,\vec{k},\vec{G}} \phi_{\vec{k},\vec{G}}(\vec{r})$$

$$\phi_{\vec{k},\vec{G}}(\vec{r}) = \begin{cases} \frac{1}{\sqrt{\Omega}} e^{i(\vec{k}+\vec{G})\cdot\vec{r}} & \vec{r} \in \mathbf{Interstitial} \\ \sum_{lm} \left(a_{\vec{k}\vec{G}lm} u_l(r) + b_{\vec{k}\vec{G}lm} \dot{u}_l(r) \right) Y_{lm}(\hat{r}) & \vec{r} \in \mathbf{Spheres.} \end{cases} \qquad (6.38)$$

Therein the expansion coefficients $c_{i,\vec{k},\vec{G}}$ and the matching coefficients $a_{\vec{k}\vec{G}lm}$ and $b_{\vec{k}\vec{G}lm}$ give rise to the partial density of states $\mathrm{DOS}_{l,m}(E)$, the spherical harmonics $Y_{lm}(\hat{r})$ are treated within the angular integral, and the radial functions $u_l(r)$ and $\dot{u}_l(r)$ have to be considered within the radial integral of the transition matrix element.

In the general case, the integrals in the Equations 6.37 have to be extended over the whole unit cell, which would require the expansion of the plane waves in terms of

spherical harmonics. However, since the radial function of the core state $R_{l_0}(r)$ is strictly confined to the atomic sphere, the radial integrals only have to be calculated up to the muffin tin radius R_{MT} (see Page 23).

Due to the fact that $u_l(r)$ and $\dot{u}_l(r)$, apart from the potential, only depend on the expansion energy E_l, and since the same radial functions are used for all $\vec{k}$ and $\vec{G}$, the radial integrals give rise to the energy dependent radial matrix elements $M_{\mathrm{D}}^{\mathrm{R}}(E)$ and $M_{\mathrm{Q}}^{\mathrm{R}}(E)$ that are valid for all states $\vec{k}$ and $\vec{G}$ having the energy E. The code for the calculation of M_{D} used in the WIEN package [Wien97] was modified to yield M_{Q} as well.

Thus, the ingredients for the calculation of the radiative transition probability are the partial densitiy of states $\mathrm{DOS}_{lm}(E)$ multiplied by the respective radial matrix elements $M_{lm}(E)$ and weighted with the respective factors $W_{l_0,l}$ from the angular integrals. In the case of quadrupolar transitions additionally the factor $k^2/4$ has to be accounted for (see Eq. 6.10).

6.5   Comparison with Measured Spectra

In order to verify the above given procedure, fluorescence spectra of As, Ge, and Ga have been calculated, including both the dipolar and the quadrupolar transitions. They are compared to the measured spectra in Fig. 6.2.

The intensity of the quadrupolar transition turns out to be underestimated by a factor of 1.2 common to all elements considered here. Moreover, the 3d peaks as calculated from the ground state band structures (dashed lines) occure at higher energies than in the measured spectra (solid lines). This is due to the screening of the 3d hole present in the final state of the quadrupolar transition which is not considered in the ground state band structure. The screening of the 4p hole created in a dipolar transition apparently has no significant effect, since the shape of the dipolar valence fluorescence line is nicely reproduced by the ground state band structure.

To account for the screening of the 3d hole the band structures of Ga, Ge, and As have been calculated with a $3d^9$ configuration. In order to enforce the nine-fold occupation within the WIEN package, the 3d-states have to be treated as core electrons. This treatment is justified by the strong localization of the 3d-states, emphasized by the fact that less than 0.05 core electrons leak out of the muffin tin radii in all three cases (see Page 23). Moreover, calculations of the $3d^{10}$ configurations with the 3d-states treated as core states have been performed, yielding exactly the same spectra as with the 3d-states in the valence band.

The quadrupolar fluorescence lines obtained from the $3d^9$ configurations are depicted with dotted lines in Fig. 6.2. The intensity of the quadrupolar peaks has not changed significantly, but the positions of the peaks are shifted towards lower energies, as expected. Indeed they now occur at lower energies than in the measured spectra. Apparently for this case the screening effects are overestimated roughly by a factor of two.
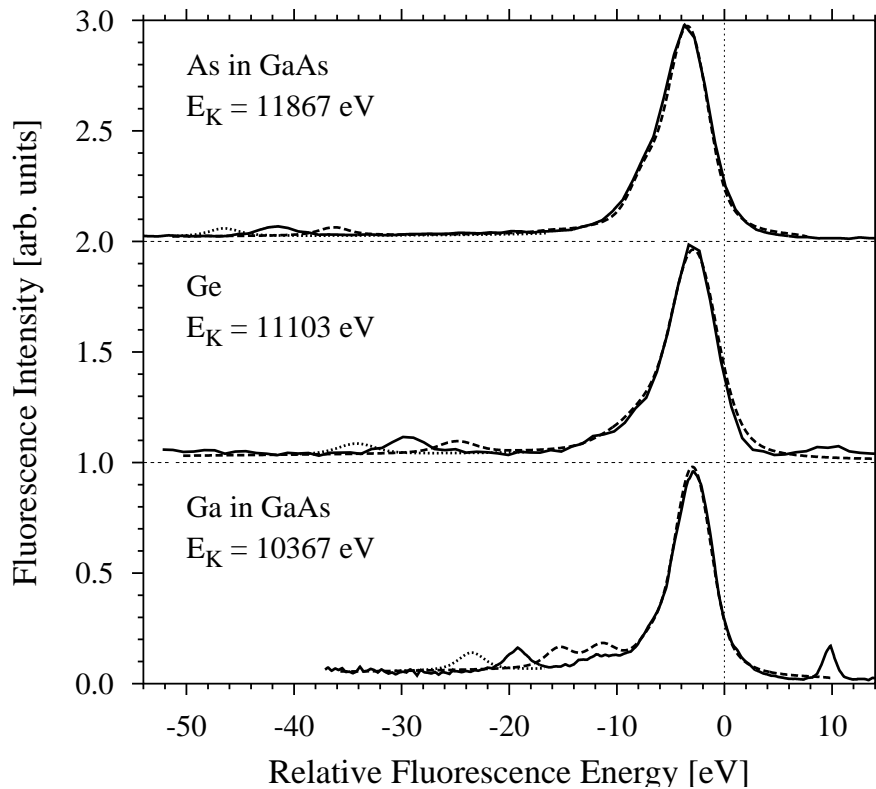
Figure 6.2: Measured and calculated dipolar and quadrupolar fluorescence lines. The fluorescence energies are relative to the respective 1s binding energy E_K, indicated for each element. The measured spectra are drawn with solid lines. Spectra calculated from the $3d^{10}$ configurations are given with dashed lines, whereas spectra from the $3d^9$ configurations are plotted with dotted lines.

To bring the 3d peaks calculated from the ground state band structure to the positions they show in the measurements they have to be shifted by -5.5 eV, -4.6 eV, and -4.0 eV in the case of As, Ge, and Ga, respectively, and for Zn a shift of -2.4 eV was determined in the same way. For Ni the shift is expected to be significantly smaller since the 3d electrons in Ni, due to their smaller binding energy, are more
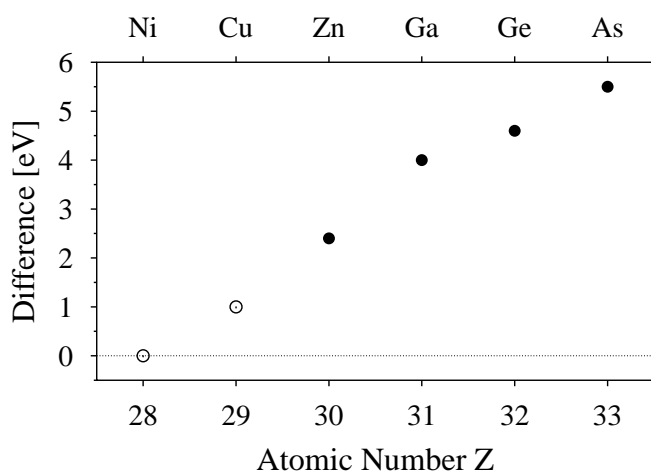
Figure 6.3: Differences between the measured and calculated energetic positions of quadrupolar transitions. For Z from 30 to 33 the differences could be determined directly from fluorescence spectra (filled circles). The other two data points have been deduced indirectly.

delocalized than the d electrons in Ga, Ge, and As. From the good agreement between measured and calculated Bloch $\vec{k}$-selective spectra of NiAl (see Chapter 3) one concludes that in that case no noteworthy shift is present. Therefore, it seems to be justified to assume a shift of -1 eV for Cu. These findings are summarized in Fig. 6.5.

From these results it is concluded that in the case of Cu the energetic position of the 3d-states, as obtained from a calculation of the electronic ground state, has to be shifted by -1 eV towards lower energies if quadrupolar transitions into the 1s states are to be considered. Moreover, the intensity of the quadrupolar contribution is correctly accounted for within the scheme described above, if an additional factor of 1.2 is introduced.

6.6   Dipolar and Quadrupolar Emission in Cu

The interplay of the DOS and the matrix elements determining the shape and the intensity of the valence fluorescence line of Cu is demonstrated in Fig. 6.4. Although the valence band is dominated by the 3d electrons, the emission spectrum mainly
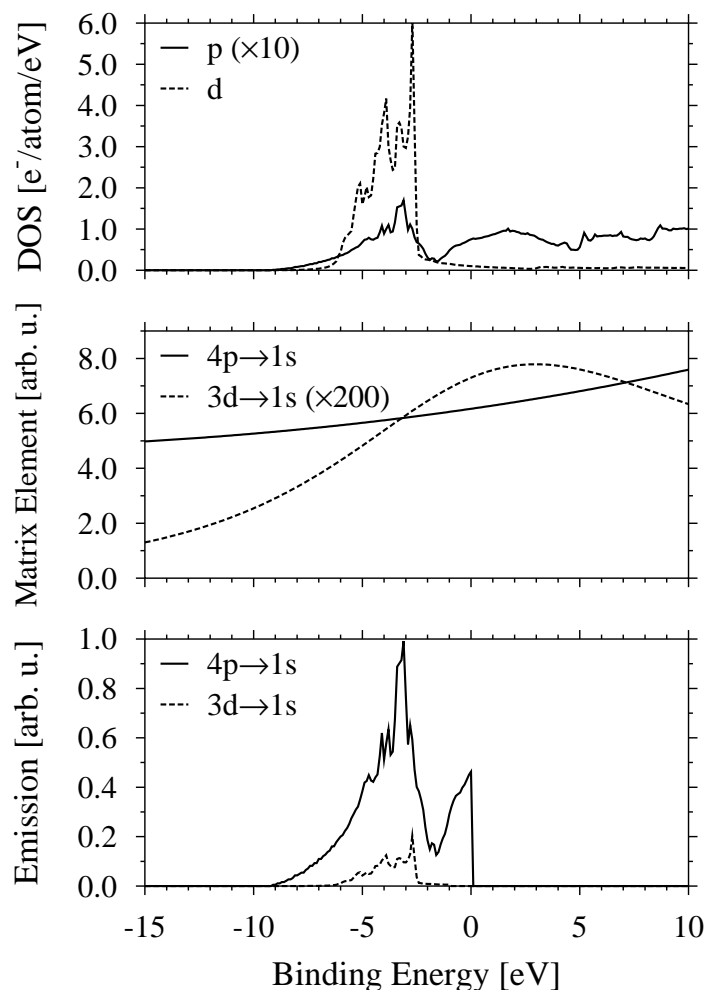
Figure 6.4: DOS, matrix elements, and emission intensity at the valence fluorescence line of Cu. In the emission spectrum the broadening due to the finite lifetime of the intermediate state has not been accounted for.
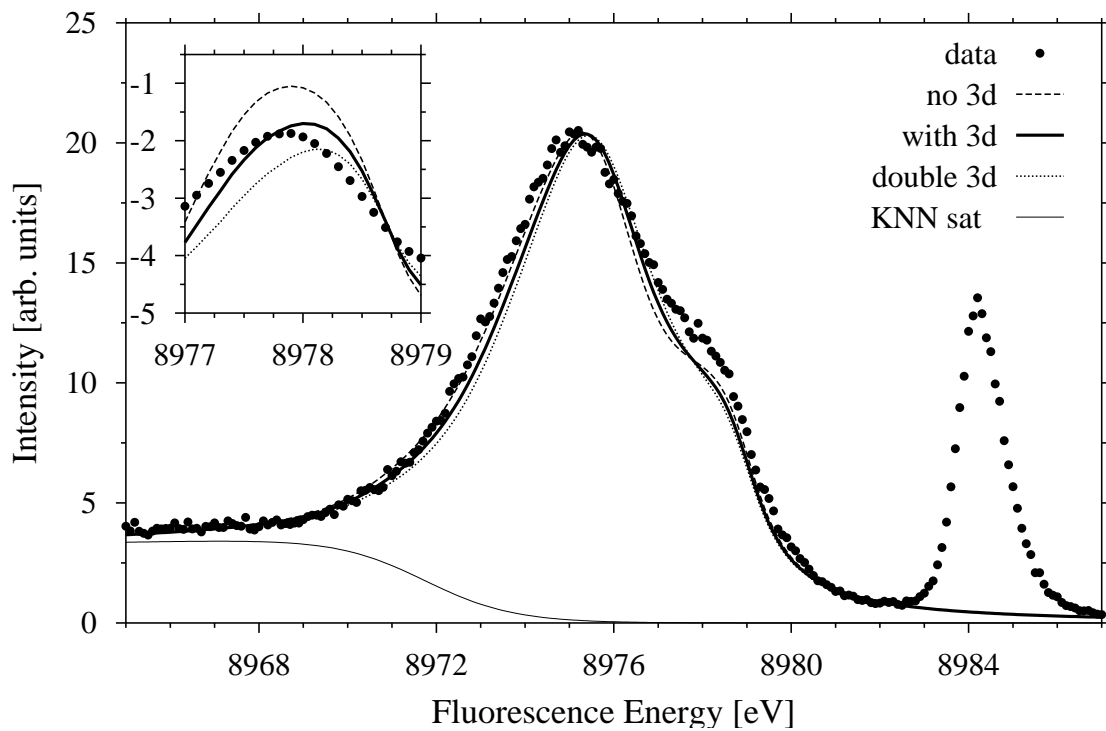
Figure 6.5: Influence of the quadrupolar transition on the valence fluorescence spectrum of Cu. The calcuated fluorescence spectrum (thick solid line) is confronted with a measured spectrum (dots) obtained from a powder sample and thus showing no Bloch $\vec{k}$-selective features. The radiative Auger satellite (thin solid line) is calculated as described in Chapter 7. The dashed and the dotted lines represent calculated spectra were the 3d contribution has been neglected and doubled, respectively. The peak at 8984 eV is due to quasi-elastic scattering. In the inset the first derivatives are shown.

reflects the 4p electrons since the matrix element for the quadrupolar transition is a factor of 200 smaller than the dipolar matrix element.

The corresponding valence fluorescence spectrum, including the core hole Lorentzian with a FWHM of 1.55 eV is shown in Fig. 6.5. The calcuated fluorescence spectrum (thick solid line) is confronted with a measured spectrum (dots) obtained from a powder sample and thus showing no Bloch $\vec{k}$-selective features. The thin solid line is the radiative Auger satellite which will be considered in the next Chapter. The dashed and the dotted lines represent calculated spectra where the 3d contribution has been omitted (dashed line) and where the 3d contribution is assumed to be twice as large (dotted line). In the inset the first derivatives of the spectra are depicted. They clearly show that the slope of the high energy shoulder is described best by the spectrum taking into account the 3d contribution as described in this chapter.

6.7 The Angular Dependence of the 3d→1s Quadrupolar Transition

So far the angular dependence of the quadrupolar contribution has been neglected. If the core state has s-symmetry, the intensities of the dipolar and quadrupolar transitions have the following angular dependence [Boch98]:

$$I_{\mathrm{D}} \quad \propto \quad p_x \epsilon_x^2 + p_y \epsilon_y^2 + p_z \epsilon_z^2 \tag{6.39}$$

$$I_{\mathrm{Q}} \quad \propto \quad d_{xy} \left(\epsilon_x k_y + \epsilon_y k_x \right)^2 + d_{yz} \left(\epsilon_y k_z + \epsilon_z k_y \right)^2 + d_{xz} \left(\epsilon_z k_x + \epsilon_x k_z \right)^2$$

$$+ \quad d_{x^2-y^2} \left(\epsilon_x k_x - \epsilon_y k_y \right)^2 + 3 d_{z^2} \left(\epsilon_z k_z \right)^2 . \tag{6.40}$$

Therein $p_x, \ldots$ and $d_{xy}, \ldots$ are the partial densities of states, while $\epsilon_x^2, \ldots$ and $\left(\epsilon_x k_y + \epsilon_y k_x \right)^2, \ldots$ are the corresponding so-called partial spectral weights (see for example [Boch98]). The partial spectral weights express the angular dependence of the transitions and contain the cartesian coordinates of the polarization vector $\hat{\epsilon}$ and of the wave vector $\hat{k}$. These formulae can be derived from the equations shown in Section 6.3, as well as from a different approach which is given in Appendix B. Apparently the dipole transitions are independent of $\hat{\epsilon}$ if the partial densities of states p_x, p_y, and p_z are degenerate as it is the case for cubic crystals.

In a cubic system the d-orbitals are split into the e_{g} and $t_{2\mathrm{g}}$ symmetries according to $e_{\mathrm{g}} = d_{x^2-y^2} + d_{z^2}$ and $t_{2\mathrm{g}} = d_{xy} + d_{yz} + d_{xz}$, respectively (see for example [Atki97]). The orientation of $\hat{\epsilon}$ and $\hat{k}$ with respect to the coordinate system of the crystal can be defined in terms of the three angles θ, ϕ, and ψ, as depicted in Fig. 6.6.

$$k_x = \sin \theta \, \cos \phi$$
$$k_y = \sin \theta \, \sin \phi$$
$$k_z = \sin \phi$$

$$\epsilon_x = \cos \theta \, \cos \phi \, \cos \psi - \sin \phi \, \sin \psi$$
$$\epsilon_y = \cos \theta \, \sin \phi \, \cos \psi - \cos \phi \, \sin \psi$$
$$\epsilon_z = - \sin \theta \, \cos \psi$$

Figure 6.6:
Orientation of $\hat{\epsilon}$ and $\hat{k}$ in terms of θ, ϕ, and ψ.
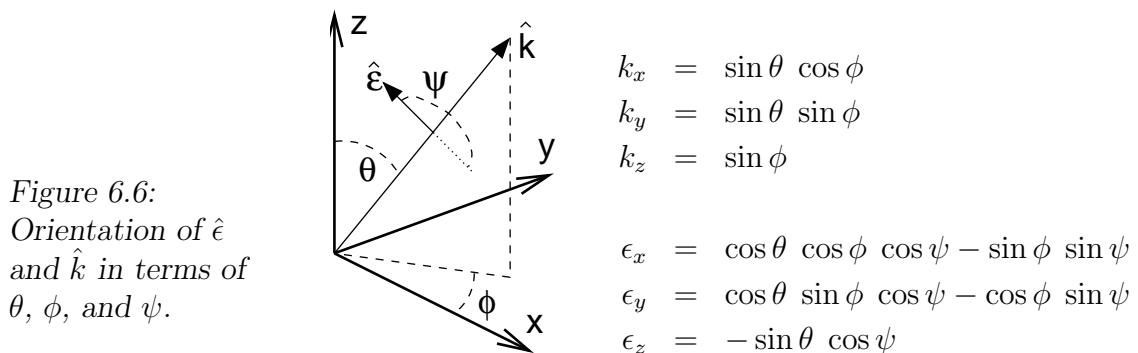
In the case of a fluorescence process the polarization of the outgoing photon usually is not known. Therefore the two possible orientations of $\hat{\epsilon}$ corresponding to $\psi = 0°$ and $\psi = 90°$ have to be considered. Moreover, in the experiments to be discussed here $\vec{k}$ was perpendicular to the crystal z-axis of the sample, corresponding to $\theta = 90°$. The resulting dependence on ϕ, being proportional to the scattering angle Θ, of the e_{g} and $t_{2\mathrm{g}}$ partial spectral weights is shown in Fig. 6.7

The scattering angle was close to $90°$ in the experiments in question here, corresponding to $\phi = 45°$. If the polarization vector $\hat{\epsilon}$ of the outgoing photon is perpendicular to the scattering plane (which is spanned by $\vec{k}_1$ and $\vec{k}_2$), ψ is equal to $0°$. In this
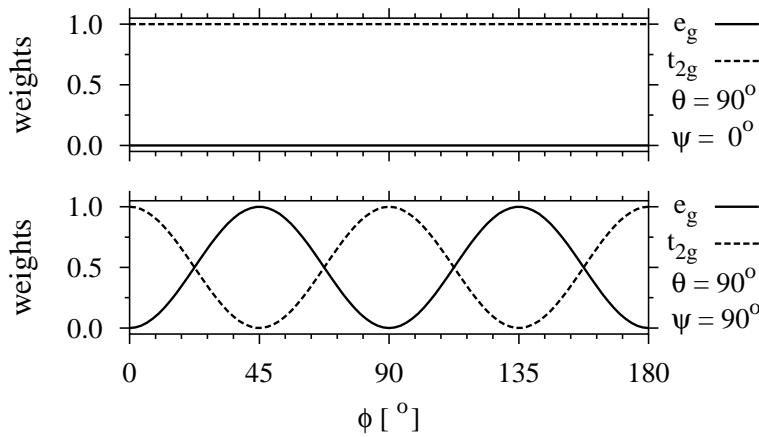
Figure 6.7: Angular dependence of the e_g and t_{2g} partial weights.

case the 3d→1s fluorescence radiation originates exclusively from the t_{2g}-states. If on the other hand the polarization vector $\hat{\epsilon}$ is parallel to the scattering plane, ψ is equal to 90° and only the e_g-states are reflected in the quadrupolar fluorescence spectrum. Thus, under the experimental conditions of the experiment in quesiton here, equal contributions from the e_g- and t_{2g}-states are to be expected.

Moreover, even large fluctuations of the partial spectral weights would have only marginal influence on the shape of the fluorescence spectra, since the e_g and t_{2g} DOS of Cu have similar shape, as shown in Fig. 6.7. In the case of Ga, Ge, and As no effect at all is to be expected, since there the width of the 3d bands is much smaller than the energetic lifetime broadening due to the core hole.
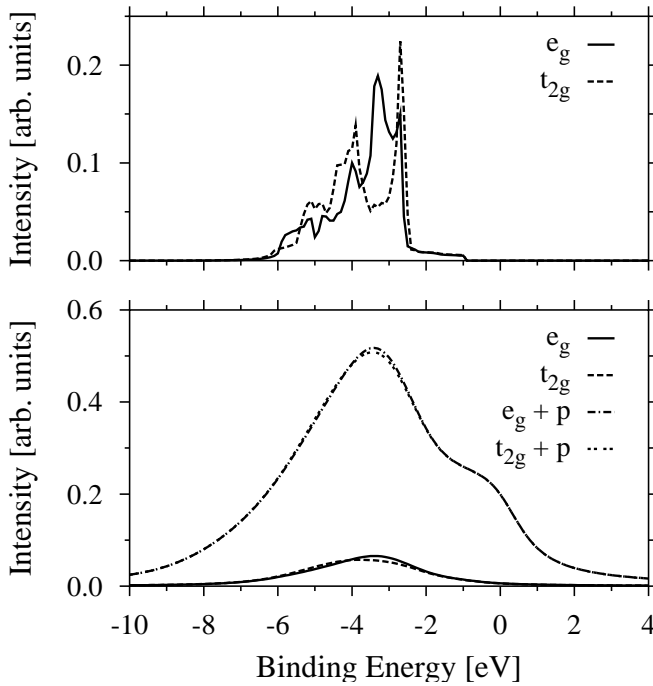
Figure 6.8: Angular dependence of the e_g and t_{2g} partial contributions to the non Bloch $\vec{k}$-selective fluorescence emission without (upper panel) and with the broadening due to the lifetime of the core hole (lower panel).

Conclusion

The relative intensity of the 4p→1s dipolar and the 3d→1s quadrupolar fluorescence radiation can be properly accounted for by the calculation of the respective matrix elements along the described lines. Moreover, the energetic position of the 3d-states, as obtained from a calculation of the electronic ground state, has to be shifted by -1 eV towards lower energies for the case of Cu, if 3d→1s transitions are to be considered. Angular dependence effects can be neglected for the case of Cu.

Chapter 7

The Radiative Auger Satellite of the Valence Fluorescence Line

Apart from the the so-called diagram lines such as the $K\alpha_{1,2}$ and $K\beta_{1,3}$ lines for example, a variety of satellite structures is visible in x-ray fluorescence spectra. Despite their low intensity many have been observed as early as in the 1920s (see for example [Druy27]). The low energy feature obscuring the valence fluorescence line as described in Chapter 3, can be assigned to one of these satellites. If calculated valence fluorescence spectra are to be compared to measured ones, this satellite line has to be properly accounted for. Therefore knowledge of its shape is essential.

Within this chaper, the low energy satellite of the valence fluorescene line of Cu is accounted for by means of a semiempirical model function, that is derived from the resonant term of the DDSC. The applicability of this model function is confirmed at another satellite line which is influenced by the Cu $K\beta_{1,3}$ fluorescene line. Therefore this chapter is organized as follows. In the first sections the fundamentals of the x-ray satellites are resumed. Then the intensity of the valence satellite as a function of the atomic number Z is investigated. In the subsequent sections the shape of resonantly excited fluorescence lines and the shape of the low energy satellites are derived from the DDSC. The resulting formulae are then applied to the Cu $K\beta_{1,3}$ fluorescene line and to its low energy satellite line. Finally the shape of the low energy satellite of the valence line is investigated.

The x-ray satellites cannot be explained within the frozen core approximation. They rather originate from the rapid change of the potential during the creation or annihilation of a core hole. The change of the potential leads to a rearrangement of the electronic states and gives rise to double ionization processes. In such a shake process, figuratively speaking the rearranging electrons 'shake' away one electron.

Shake processes during the *absorption* of an electron or a photon can occur if the energy of the incoming particle is large enough to excite two or more electrons of the same atom into the formerly unoccupied states. These multi-ionization processes during the absorption of a particle therefore show a characteristic onset at a certain incident energy. The x-rays emitted during the subsequent radiative relaxation can be thought of as ordinary fluorescence lines from atoms having additional vacancies, the so-called spectator hole states. Consequently, the resulting satellite lines have linewidths similar to the respective diagram lines.

Usually, but not always, these satellites occur at higher energies than their parent lines since the screening of the nuclear charge is reduced due to the absence of an inner shell electron. Within the Z+1 approximation the energetic position of the satellite is equal to the energy of the diagram line added to the difference of the ionization energies of the second ejected electron in the element considered and in the Z+1 element. Recent studies of satellite lines due to a shake process during the absorption of a photon are the Cu K$\alpha_{3,4}$ satellites [Frit98], the Cu K$^{\mathrm{h}}\alpha_{1,2}$ hypersatellites [Diam00], the Ge Kβ''' satellites [Ster00], and the Cu Kβ' and Kβ'' satellites [Deut95]. The latter are also discussed in Appendix C.

7.1   The Radiative Auger Effect

X-ray satellites that occur due to shake processes during the *emission* of a photon are referred to as radiative Auger satellites (RAS) since the underlying process is complementary to the nonradiative Auger effect (AE).

An Auger process consists of a radiationless deexcitation of an electron into a previously generated core hole together with the simultaneous excitation of another electron into the unoccupied states. Thus, the initial state of this process contains one inner shell vacancy, whereas in the final state two vacancies are present. The energy difference between the final and the initial state is carried away by the excited electron, the so-called Auger electron, by its kinetic energy E_{e^-}:

$$E_{\mathrm{e}^-} = \Delta E = E_i - E_f. \tag{7.1}$$

In many cases the kinetic energy is large enough to let the Auger electron escape from the sample. The energy distribution of the Auger electrons can then be measured and gives rise to the Auger electron spectroscopy, which has proven to be a valuable tool for the elemental analysis of gases and surfaces.

In a radiative Auger process only part of the energy difference ΔE is transferred to the Auger electron whereas the rest of the energy is emitted as a photon. From another point of view, a fluorescence photon suffers an energy loss due to the simultaneous excitation of another electron into unoccupied states. The energy difference ΔE thereby is arbitrarily subdivided between the photon and the Auger electron:

$$\hbar\omega_2 + E_{\mathrm{e}^-} = \Delta E = E_i - E_f. \tag{7.2}$$

Therefore, in contrast to satellites originating from shake processes during the absorption of a photon, the resulting satellite feature is situated on the low energy side of its corresponding parent line. Radiative Auger satellites can extend over hundreds of electron volts, and usually they show only little fine structure. The fluorescence energy corresponding to the minimal energy loss, where $E_{\mathrm{e}^-} = 0$ and thus $\hbar\omega_2 = \Delta E = E_i - E_f$, is the onset energy of the radiative Auger satellite.

The radiative Auger satellite to a K$\beta_{1,3}$ line shown in Fig. 7.1 is due to secondary ionization of the 3p level during relaxation of a 3p electron into the 1s level. Thus, the onset energy of the satellite is equal to the K$\beta_{1,3}$ fluorescence energy minus the

Figure 7.1: Schematic diagram of the radiative Auger satellite to a $K\beta_{1,3}$ line.
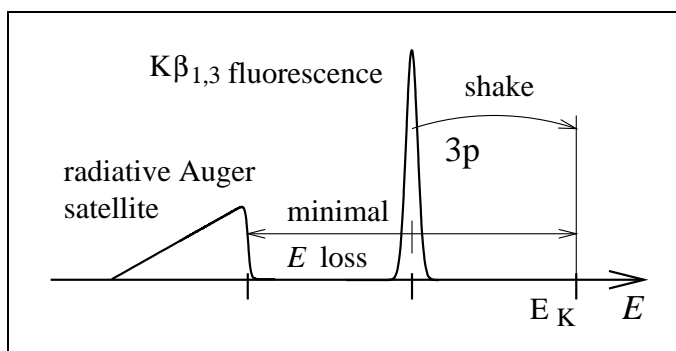
binding energy of the 3p state. This onset energy is identical to the energy of the Auger electron in the complementary Auger process (see Fig. 7.2).

At the onset energy, the satellite shows a sharp rise. Towards lower photon energies, i.e. larger energy losses, the intensity of the satellite slowly decreases, since small energy losses are more likely to occur than large energy losses. This is due to the fact that the overlap between the orbitals involved in the secondary excitation rapidly decreases with increasing energy difference (see for example [Pire64, Livi88]). Therefore, radiative Auger satellites exhibit a shape similar to a shark fin.

The nomenclature for the radiative Auger satellites is identical to the nomenclature for the Auger lines. It consists of three letters: the first labels the principal quantum number of the hole present in the initial state, and the two other letters label the
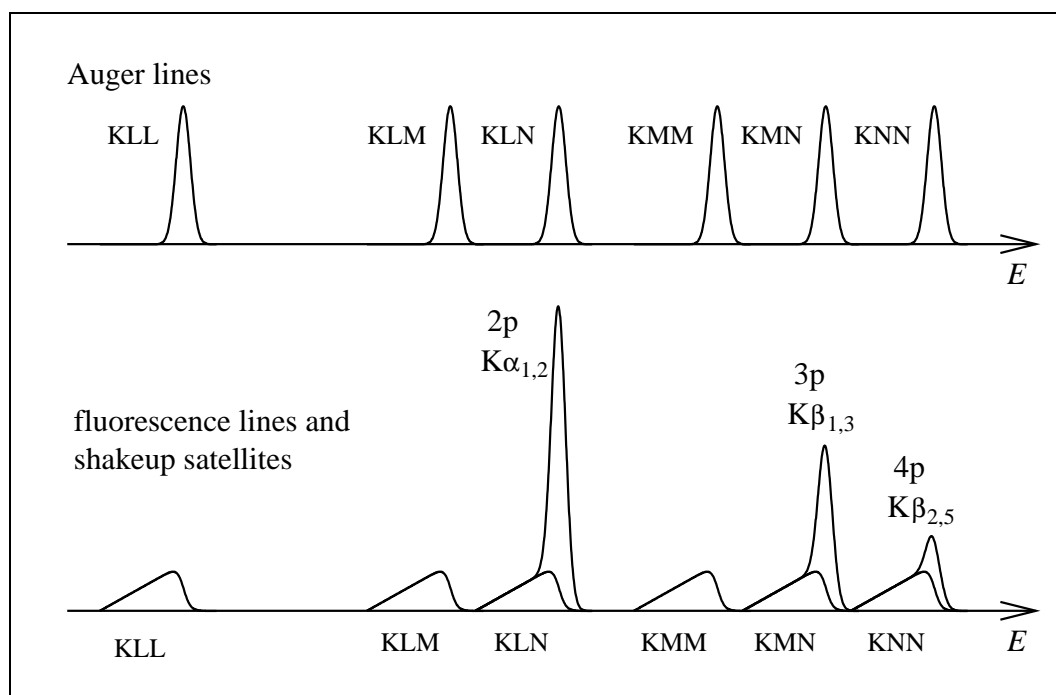
Figure 7.2: Schematic diagram of the K series of Auger lines (upper panel) and the respective radiative Auger satellites together with the fluorescence emission lines (lower panel) possible for the 4th row elements.

vacancies present in the final states.

Since the initial and final state of the Auger and of the radiative Auger process are the same, each Auger line has a corresponding radiative Auger satellite in the x-ray spectrum. The variety of radiative Auger and nonradiative Auger lines possible for 4th row elements is shown in Fig. 7.2. The satellites originating from a valence electron excitation KLN, KMN, and KNN are widely obscured by their respective parent lines $K\alpha_{1,2}$, $K\beta_{1,3}$, and $K\beta_{2,5}$, whereas the other satellites KLL, KLM, and KMM are separated from their parent lines and thus can be measured independently.

7.2 The Onset Energies of Radiative Auger Satellites

In the case of the KLL satellite the energies E_i and E_f are the total energies of the electron system in the presence of one 1s hole and two 2p holes, respectively. If the emission of the fluorescence photon and the simultaneous excitation of another electron are treated as two independent processes the total energy released in the shake process is

$$\Delta E = E_{\mathrm{K}} - (E_{\mathrm{L}} + E_{\mathrm{L}}'), \tag{7.3}$$

where E_{K} and E_{L} are binding energies of the K shell and the L shell in a neutral atom, respectively, whereas E_{L}' is the binding energy of an L electron in the presence of a hole in the L shell. To this formula several approximations can be applied.

- **Frozen core approximation:** The change of the binding energies upon the creation and annihilation of core holes is neglected, as is shown in Fig. 7.1. Then the total energy released equals:

$$\Delta E = E_i - E_f = E_{\mathrm{K}} - E_{\mathrm{L}} - E_{\mathrm{L}}. \tag{7.4}$$

  The shift of eigenstates towards lower energies due to the screening of the hole in the L shell is neglected. Thus, the onset energies calculated within this approximation are too large.

- **$Z+1$ approximation:** The binding energy of an electron in an atom with atomic number Z in the presence of a hole in another shell is assumed to equal its respective binding energy in an atom with atomic number $Z+1$:

$$\Delta E = E_{\mathrm{K}}(Z) - (E_{\mathrm{L}}(Z) + E_{\mathrm{L}}(Z+1)). \tag{7.5}$$

  In this case the band shifts due to screening are overestimated, yielding onset energies that are too small in comparison with the experiment.

- **ΔZ approximation:** This is a compromise between the two approximations described above by using fractional nuclear charges:

$$\Delta E = E_{\mathrm{K}}(Z) - (E_{\mathrm{L}}(Z) + E_{\mathrm{L}}(Z+\Delta Z)), \tag{7.6}$$

where

$$E_{\mathrm{L}}(Z + \Delta Z) = (1 - \Delta Z)E_{\mathrm{L}}(Z) + \Delta Z E_{\mathrm{L}}(Z + 1). \qquad (7.7)$$

The fractional charge $\Delta Z(Z) \in [0, 1]$ has to be determined empirically.

In addition, the splitting of states due to spin orbit coupling has to be accounted for in the calculation of the onset energies. Each combination of hole states, e.g. L_3L_3, L_3L_2, L_2L_2, and so on in the L shell, gives rise to a separate satellite line, resulting in a fine structure in the high energy region of the radiative Auger satellites, close to their onset energies. However, a more detailed calculation of the onset energies requires knowledge of the coupling between the two unfilled shells in the final state. For light elements the coupling scheme is pure $L-S$, for heavy atoms it is $j-j$, and for elements in the middle of the periodic table intermediate coupling has to be considered (see for example [Carl75]). Fig. 7.3 shows the Auger transitions that can arise from KLL processes, as a function of the atomic number Z.
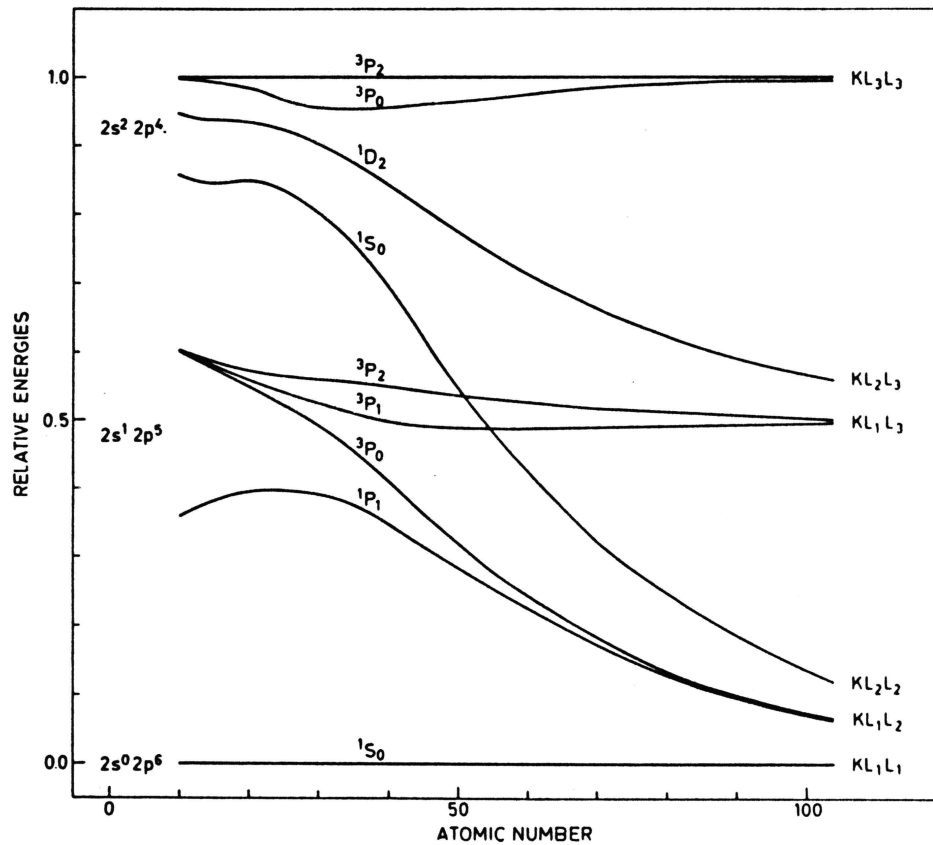
Figure 7.3: *Spin orbit coupling schemes: relative Auger energies of KLL transitions as a function of Z, reproduced from [Carl75]. At low Z pure $L-S$ coupling gives rise to six Auger lines. For high Z nearly pure $j-j$ coupling also yields six lines. In the region of intermediate coupling nine transitions are possible. Similar coupling applies to the KMM transitions.*

Though the characteristic energies of the Auger and of the radiative Auger effect are identical, since they can be calculated from the same total energy considerations, the two processes originate from different transition operators. Therefore they have different transition matrix elements and thus are governed by different selection rules.

The nonradiative Auger effect is due to a Coulomb interaction whereas, the radiative Auger effect arises from a fluorescence photon that virtually photoejects another electron. The Coulomb operator $\mathcal{H}_{\text{int}} \propto \frac{e^2}{r}$ leads to $\Delta l = \Delta s = \Delta j = 0$ which is fulfilled for arbitrary combinations of any three subshells. Thus, the energy conservation is the only restriction to the occurence of the nonradiative Auger effect.

In contrast, the dipole operator $\mathcal{H}_{\text{int}} \propto \vec{A} \cdot \vec{p}$ governing the radiative Auger effect introduces the dipole selection rules $\Delta l = \pm 1, \Delta s = 0, \Delta j = \pm 1$. This difference is demonstrated by the existence of a 1s to 2s2s nonradiative Auger transition which does not occur in the radiative Auger spectrum (see for example [Carl75]).

More light is shed on the nature of the radiative Auger effect, if the transition probability is actually calculated. This was done by Åberg [Åber71] using formulae given by Löwdin [Löwd55]. These allow to calculate the transition matrix elements of Slater determinants that are built up from nonorthogonal basis sets. This yields

$$I \propto \left| \langle \Psi_1 | \vec{A} \cdot \vec{p} | \Phi_1 \rangle \langle \Psi_2 | \hat{\mathbf{1}} | \Phi_2 \rangle \right|^2 = |M_{\text{D}} M_{\text{M}}|^2 \,, \tag{7.8}$$

where $\hat{\mathbf{1}}$ is the one-operator, defined by $\hat{\mathbf{1}} |\Phi\rangle = |\Phi\rangle$. The matrix element $|\Phi_1\rangle \rightarrow |\Psi_1\rangle$ describes the radiative annihilation of the core hole, while $|\Phi_2\rangle \rightarrow |\Psi_2\rangle$ accouts for the nonradiative shake excitation. Thus, the radiative Auger effect is due to a combined electric dipole and electric monopole transition. It is governed by dipole selection rules in the fluorescence part of the process and by monopole selection rules for the secondary excitation. As a result, some transitions allowed in an Auger process are forbidden in a radiative Auger process, e.g. KL_1L_1.

It is important to note that $|\Phi\rangle$ and $|\Psi\rangle$ are eigenstates of different Hamiltonians. The $|\Phi\rangle$ are eigenstates in the presence of the core hole, while the $|\Psi\rangle$ are eigenstates with no core hole present. Otherwise Ψ_2 and Φ_2 would be orthogonal and the monopole matrix element $M_{\text{M}} = \langle \Psi_2 | \hat{\mathbf{1}} | \Phi_2 \rangle$ would vanish. Reversely, the stronger the orbial emitting the shake electron changes upon the annihilation of the core hole, the larger is the overlap between the formerly orthogonal states Ψ_2 and Φ_2, and the larger is the intensity of the resulting radiative Auger satellite.

7.3   The Intensity of the Valence Auger Satellite

The intensity of radiative Auger satellites as a function of the atomic number Z has been studied both experimentally and theoretically. Especially the KLL and KMM satellite lines have been investigated extensively in the last decades. Experimental and theoretical results found in the literature are shown in Fig. 7.4. There the relative shake probability, i.e. the integrated intensity of the satellite line with respect to the integrated intensity of its parent line, $P_{sat} = I_{sat}/I_{parent\ line}$, is depicted for elements in the range of $Z = 10$ to 35. The intensity of the satellite lines decreases with increasing atomic number Z, and shake processes from outer shells are more likely to occur than shake processes involving inner shell electrons ($P_{KLL} < P_{KMM}$).
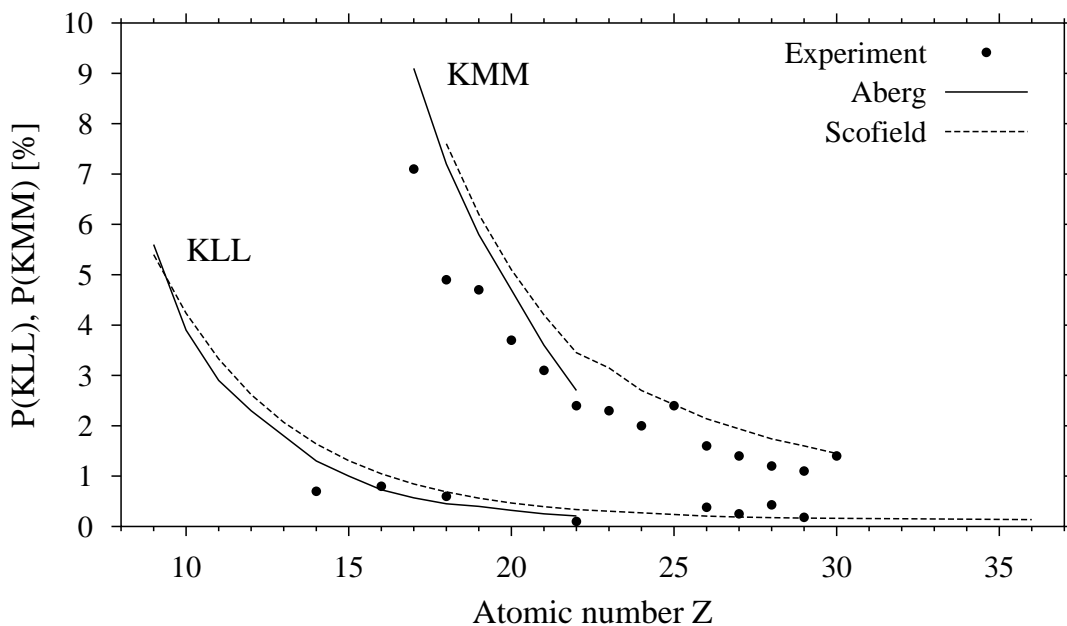
Figure 7.4: Measured relative intensities of KLL and KMM satellites compiled from the literature as a function of Z together with shake probabilities calculated by Åberg [Åber71] and Scofield [Scof74]. Measured KMM probabilities have been reproduced from [Kesk80]. The original articles are [Utri73], [Kesk74], [Serv75], [Kesk80]. The measured KLL probabilities are taken from [Åber71] and [Koo90].

However, the KNN satellite line of the 3d elements has not attracted attention so far. In the case of the 4th row elements, the KNN satellite stems from the valence fluorescence radiation with a simultaneous shake excitation of another valence electron. Spectra of the $K\beta_{2,5}$ valence fluorescence line together with its radiative Auger satellite are shown in Figure 7.5 for the elements from Co to As ($Z=27$ to $Z=33$).

The intensity of the KNN satellite line strongly decreases with Z as is expected from the results on the KLL and KMM satellites. However, at its onset energy the KNN satellite is partly obscured by the valence fluorescence line occuring at energies between -10 eV and the Fermi level. In the case of Co, Ni, Cu, and Zn the high energy tail of the $K_{\beta1,3}$ line also conceals the low energy tail of the KNN satellite.
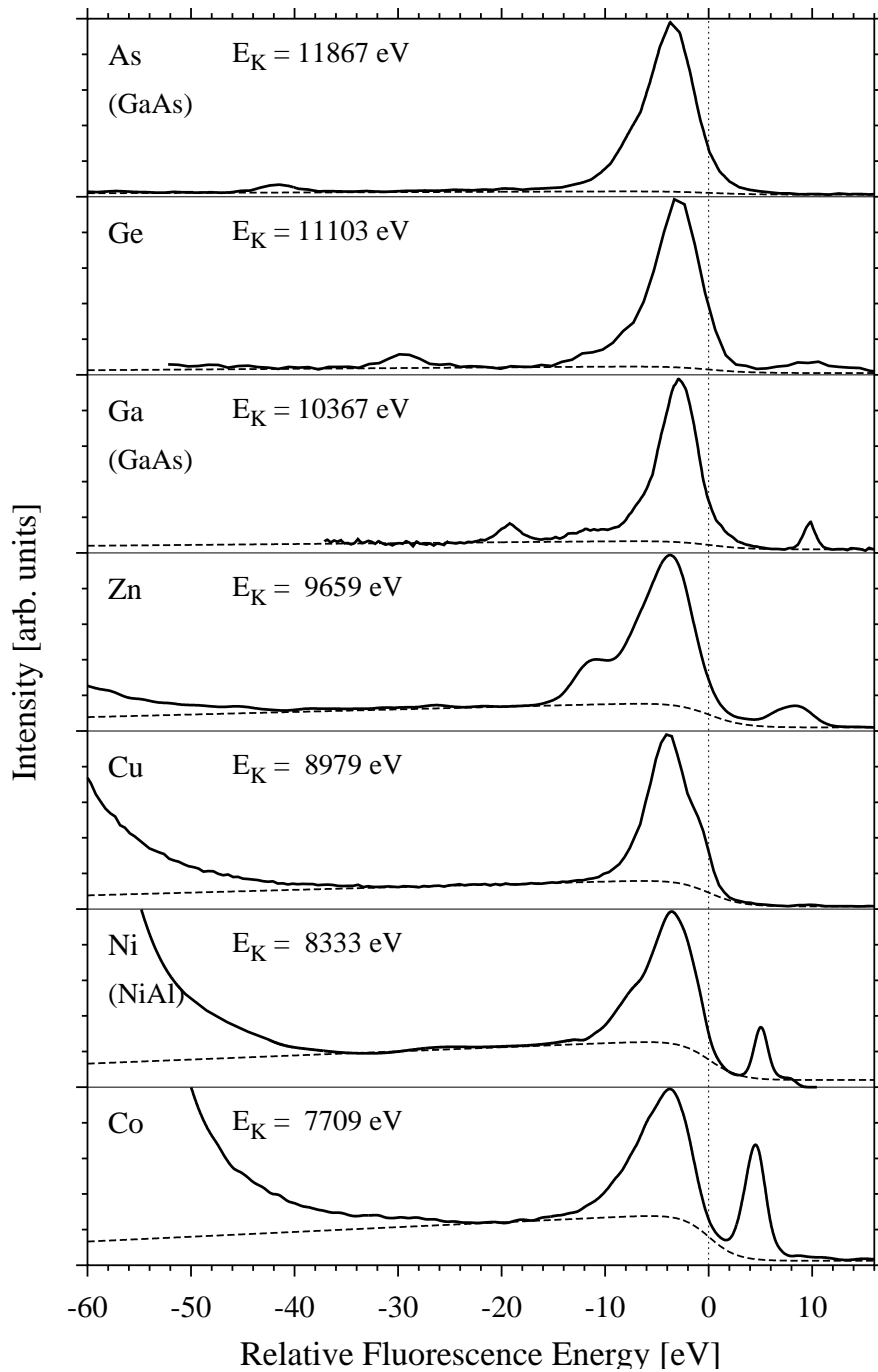
Figure 7.5: *Series of KNN valence satellite spectra (solid) together with the adapted satellite line (dashed). The energies are given relative to the respective 1s binding energy E_K, indicated for each element. The valence fluorescence lines are found in the range of -10 to 0 eV. The peaks at energies above zero are due to quasi elastic scattering, except for Ge where it is a satellite due to a double electron excitation during the absorption process [Ster00]. For the elements Co to Zn the high energy tail of the $K\beta_{1,3}$ line is visible at low energies. The dispersing low energy feature from Zn to As is due to the 3d→1s quadrupolar transition. The spectra have been measured at beamlines ID16 (Ga, As, Cu) and ID28 (Ge, Ni) of the ESRF and at beamline G3 of the HASYLAB (Co, Zn).*
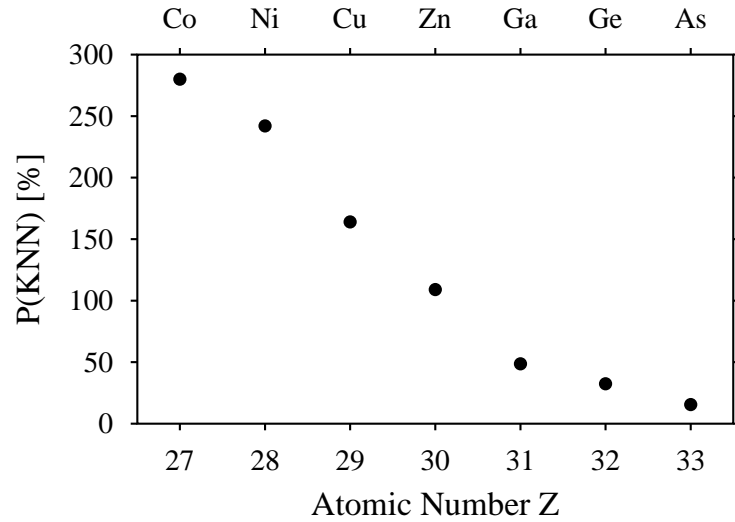
Figure 7.6: The relative intensity of the KNN valence satellite.

This makes it difficult to determine properly the shape as well as the intensity of the valence radiative Auger satellites.

Nevertheless, to estimate the relative shake probability for the KNN line P_{KNN} the line shape adopted for the satellite in Chapter 3 is applied again. It consists of a linearly rising function multiplied by an arctan function centered at the 1s binding energy:

$$I(E) = (1 + s(E - E_{\text{K}}))\, h \left[0.5 - \frac{1}{\pi} \arctan \left(\frac{2(E - E_{\text{K}})}{\Gamma} \right) \right] + b, \qquad (7.9)$$

where s, h, and Γ are the slope, the hight, and the width of the satellite, respectively, and where b accounts for a constant background. Γ has been set equal to the energetic width of the intermediate state, and the slope of the satellite line has been set to $s = 0.01$ to make the estimated satellite match all measured spectra. The dependence of P_{KNN} on Z is shown in Fig. 7.6.

As expected, one finds that $P_{\text{KNN}}(Z)$ shows the same dependence on Z as $P_{\text{KMM}}(Z)$ and $P_{\text{KLL}}(Z)$. However, the KNN satellite is much more intense than the KMM and the KLL satellite within the Z range considered here. P_{KNN} ranges from 10 % to 280 %, whereas P_{KMM} and P_{KLL} are about 1.5 % and 0.4 %, respectively. Although the absolute value of P_{KNN} strongly depends on the choice of s, the dependence of P_{KNN} on Z is not affected. Thus, the results shown here are at least qualitatively correct.

In order to properly account for the KNN radiative Auger satellite in the interpretation of Bloch $\vec{k}$-selective RIXS spectra the KMM satellite of Cu was measured. From its shape the shape of the KNN satellite line can be deduced. Due to its low intensity, the KMM line merely appears as a series of ripples on the low energy tail of the K$\beta_{1,3}$ fluorescence line, as can be seen from Figure 7.7. To obtain the pure KMM line from the measured spectrum, the low energy tail of the K$\beta_{1,3}$ fluorescence line has to be subtracted, which is done in what follows.

The rest of this chapter is organized as follows. In Section 7.4 a method for the calculation of resonantly excited fluorescence lines is derived, including the influence
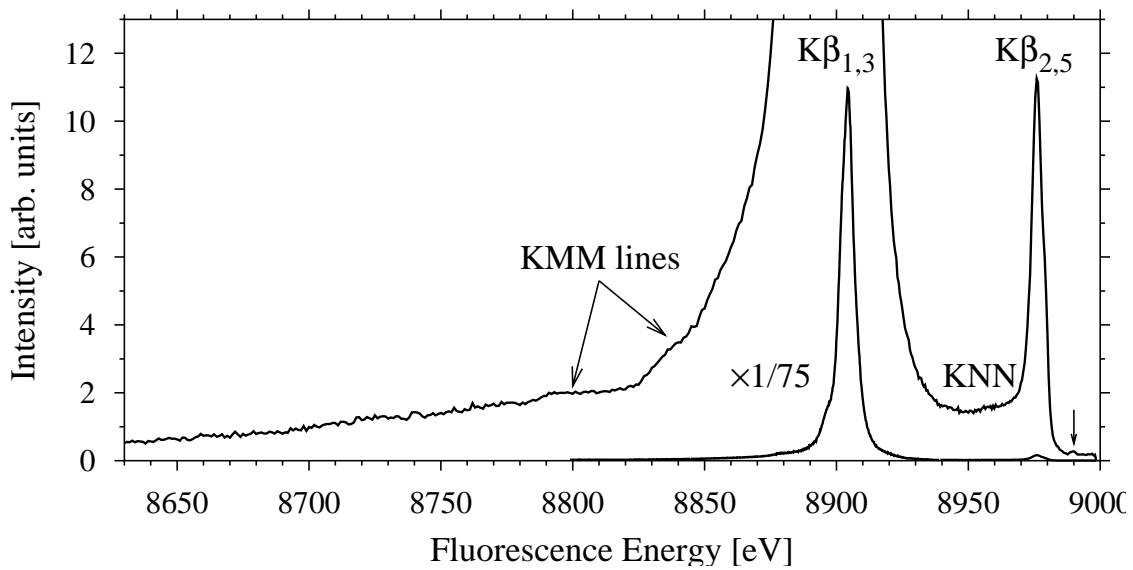
Figure 7.7: *The Cu K$\beta_{1,3}$ and K$\beta_{2,5}$ fluorescence lines together with the KMM and KNN radiative Auger satellites. The K$\beta_{1,3}$ line has been reduced by a factor of 75. Between the two diagram lines the KNN satellite is visible. The ripples on the low energy tail of the K$\beta_{1,3}$ line are the KMM lines. The faint peak at 8990 eV, marked by an arrow, is the quasi-elastic line.*

of the lifetime broadening of the intermediate state as well as the fine structure of the unoccupied DOS. Applying this method the K$\beta_{1,3}$ line of Cu is calculated, and is compared to measured spectra in Section 7.6. In Section 7.5 the shape of radiative Auger satellites is deduced from the shape of their parent lines. In Section 7.7 the KMM satellite is extracted and then compared to the shape predicted. Finally the results are applied to the KNN radiative Auger satellite in Section 7.8.

7.4 Influence of Core Lorentzian and Unoccupied DOS on the Fluorescence Line Shape

Starting from formula 1.25 in Chapter 1,

$$
\begin{aligned}
\frac{d^2\sigma}{d\omega_2\,d\Omega} \quad &\propto \quad \sum_{n_i\vec{k}_i} \sum_{n_f\vec{k}_f} \sum_{n_j} \left| M_1'(n_i, \vec{k}_i, n_j) \right|^2 \delta(E_{n_i\vec{k}_i} - E_{n_j} - \hbar\omega_1) \\
&\times \quad \delta_{\vec{G},(\vec{k}_1 - \vec{k}_2 - \vec{k}_i + \vec{k}_f)} \; \left| M_2'(n_f, \vec{k}_f, n_j) \right|^2 \delta(E_{n_i\vec{k}_i} - E_{n_f\vec{k}_f} - \hbar\omega_1 + \hbar\omega_2), \quad (7.10)
\end{aligned}
$$

the lifetime of the intermediate state is accounted for by replacing the first δ-function with the corresponding Lorentzian:

$$
\delta(E_{n_i\vec{k}_i} - E_{n_j} - \hbar\omega_1) \Rightarrow \frac{1}{(E_{n_i\vec{k}_i} - E_{n_j} - \hbar\omega_1)^2 + (\frac{\Gamma}{2})^2} = \mathrm{L}(E_{n_i\vec{k}_i} - E_{n_j} - \hbar\omega_1) \quad (7.11)
$$

$$
\begin{aligned}
\frac{d^2\sigma}{d\omega_2\,d\Omega} \quad &\propto \quad \sum_{n_i\vec{k}_i} \sum_{n_f\vec{k}_f} \sum_{n_j} \left| M_1'(n_i, \vec{k}_i, n_j) \right|^2 \mathrm{L}(E_{n_i\vec{k}_i} - E_{n_j} - \hbar\omega_1) \\
&\times \quad \delta_{\vec{G},(\vec{k}_1 - \vec{k}_2 - \vec{k}_i + \vec{k}_f)} \; \left| M_2'(n_f, \vec{k}_f, n_j) \right|^2 \delta(E_{n_i\vec{k}_i} - E_{n_f\vec{k}_f} - \hbar\omega_1 + \hbar\omega_2). \quad (7.12)
\end{aligned}
$$

To show the general influence of the incident energy on the shape of resonantly excited fluorescence lines one may assume a non Bloch $\vec{k}$-momentum conserving process and omit the Kronecker-δ. Moreover, it is usefull to restrict the considerations to experimental conditions where only one core state, e.g. the 1s level, is involved in the scattering process. Thus, the sum over n_j can be omitted:

$$
\begin{aligned}
\frac{d^2\sigma}{d\omega_2\,d\Omega} \quad &\propto \quad \sum_{n_i\vec{k}_i} \sum_{n_f\vec{k}_f} \left| M_1'(n_i, \vec{k}_i, 1\mathrm{s}) \right|^2 \mathrm{L}(E_{n_i\vec{k}_i} - E_{1\mathrm{s}} - \hbar\omega_1) \\
&\times \quad \left| M_2'(n_f, \vec{k}_f, 1\mathrm{s}) \right|^2 \delta(E_{n_i\vec{k}_i} - E_{n_f\vec{k}_f} - \hbar\omega_1 + \hbar\omega_2). \quad (7.13)
\end{aligned}
$$

Next one transforms the sums over the states $n_i\vec{k}_i$ and $n_f\vec{k}_f$ into integrals over E_i and E_f, thereby introducing the unoccupied and occupied densities of states N^{u} and N^{o}, respectively:

$$
\begin{aligned}
\frac{d^2\sigma}{d\omega_2\,d\Omega} \quad &\propto \quad \int dE_i \, |M_1'(E_i)|^2 \, N^{\mathrm{u}}(E_i) \mathrm{L}(E_i - E_{1\mathrm{s}} - \hbar\omega_1) \\
&\times \quad \int dE_f \, |M_2'(E_f)|^2 \, N^{\mathrm{o}}(E_f) \delta(E_i - E_f - \hbar\omega_1 + \hbar\omega_2). \quad (7.14)
\end{aligned}
$$

As shown in Chapter 6, the matrix elements can be evaluated, giving rise to the angular momentum selection rules from the angular part of the overlap integral. From the radial part of the integral an energy dependent radial matrix element for

each angular momentum quantum number l arises, governing the intensity of the respective transition. Accordingly the DOS is split up with respect to l into partial densities of states. Summation over all angular momentum quantum numbers yields the energy dependent intensity factors I^{u} and I^{o} for the unoccupied and the occupied bands, respectively, containing both the DOS and the matrix elements.

$$\frac{d^2\sigma}{d\omega_2\,d\Omega} \propto \int dE_i I^{\mathrm{u}}(E_i)\mathrm{L}(E_i - E_{1\mathrm{s}} - \hbar\omega_1) \int dE_f I^{\mathrm{o}}(E_f)\delta(E_i - E_f - \hbar\omega_1 + \hbar\omega_2). \quad (7.15)$$

By defining the 1s binding energy to be zero and by performing the integral over E_f one gets:

$$\frac{d^2\sigma}{d\omega_2\,d\Omega} \propto \int dE_i I^{\mathrm{u}}(E_i)\mathrm{L}(E_i - \hbar\omega_1)I^{\mathrm{o}}(E_i - \hbar\omega_1 + \hbar\omega_2). \quad (7.16)$$

The substitution $E_i - \hbar\omega_1 = \epsilon$ yields:

$$\frac{d^2\sigma}{d\omega_2\,d\Omega} \propto \int d\epsilon\, I^{\mathrm{u}}(\hbar\omega_1 + \epsilon)\mathrm{L}(\epsilon)I^{\mathrm{o}}(\hbar\omega_2 + \epsilon). \quad (7.17)$$

If now again it is assumed that $\Gamma = 0$ and thus $\mathrm{L}(E) = \delta(E)$ one finds that the shape of the emission spectrum depends solely on the DOS of the occupied states and that the shape is independent of the incident energy:

$$\frac{d^2\sigma}{d\omega_2\,d\Omega} \propto I^{\mathrm{u}}(\hbar\omega_1)I^{\mathrm{o}}(\hbar\omega_2). \quad (7.18)$$

The incident energy merely determines the over-all intensity of the fluorescence radiation via the factor $I^{\mathrm{u}}(\hbar\omega_1)$, as can be seen from panel a) of Figure 7.8. There it is assumed, that the unoccupied DOS, indicated by the dotted line, has no fine structure and that the fluorescence radiation arises from one single infinitely sharp state with the energy E_f. Since only one single state with the energy $E_i = \hbar\omega_1$ can be reached by the excited electron, the fluorescence spectrum consists of one single infinitely sharp line.

However, if one has to deal with a finite lifetime of the intermediate state, the shape of the emission line also depends on the incident energy. Due to the nonvanishing width of the Lorentzian, many states E_i corresponding to different values of ϵ can be reached in the absorption process, as shown in panel b) of Fig. 7.8. Via the conditions

$$\epsilon = E_i - \hbar\omega_1 \qquad \text{and} \qquad \hbar\omega_2 = E_f - \epsilon = E_f - E_i + \hbar\omega_1 \quad (7.19)$$

the state E_f gives rise to fluorescence photons with different energies. The respective intensity depends on the intensity of the Lorentzian at the energy $\epsilon = E_i - \hbar\omega_1$. This causes fluorescence lines to be of Lorentzian shape. If the incident energy is close to the Fermi energy E_{F}, only a part of the Lorentzian is covering unoccupied states. This leads to the asymmetry of fluorescence lines in the case of resonant excitation.

Moreover, if the incident energy is smaller than the binding energy of the core electron, i.e. $\hbar\omega_1 < E_{\mathrm{F}}$, only the low energetic tail of the fluorescence line is present.
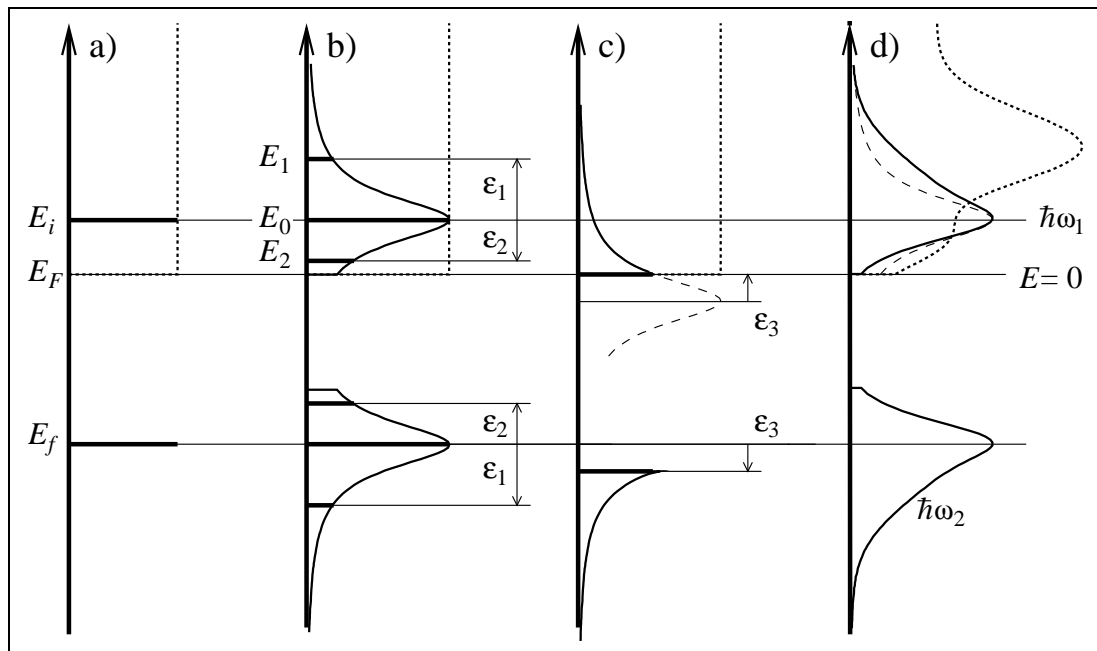
Figure 7.8: Broadening of fluorescence lines due to the lifetime of the intermediate state (see text).

This case is depicted in panel c) of Fig. 7.8, where the thin dashed line indicates the energetic position of the Lorentzian. The cutoff energy $\hbar\omega_2 = E_f - E_F + \hbar\omega_1$ (see Eq. 7.19), determined by the energetic distance ϵ_3, depends linearly on the incident energy, causing the positions of fluorescence lines to shift linearly with the incident energy. This behaviour is called the Raman shift of the fluorescence lines.

So far the shape of the unoccupied DOS has been neglected. If one now assumes the DOS to have a fine structure, as indicated by the dotted line in panel d) of Fig. 7.8, the absorption probability at a given energy ϵ does not only depend on the intensity of the Lorentzian at this energy. It also depends on the DOS via factor $I^{\mathrm{u}}(\hbar\omega_1 + \epsilon)$ in Eq. 7.17. Consequently, features of the unoccupied DOS are reflected in the shape of the fluorescence line, as indicated in panel d).

To obtain a more compact description, one can rewrite Eq. 7.17 by substituting $\epsilon \to -\epsilon$ and by defining the product of the Lorentzian with the unoccupied DOS as the absorption intensity $I_{\mathrm{abs}}(-\epsilon) \equiv I^{\mathrm{u}}(\hbar\omega_1 - \epsilon)L(-\epsilon)$, given by the solid line in Fig. 7.8. Further defining the absorption intensity mirrored at zero $\tilde{I}_{\mathrm{abs}}(\epsilon) \equiv I_{\mathrm{abs}}(-\epsilon)$ one gets:

$$\begin{aligned} \frac{d^2\sigma}{d\omega_2\,d\Omega} &\propto \int d\epsilon\; I^{\mathrm{u}}(\hbar\omega_1 - \epsilon)\; \mathrm{L}(-\epsilon)\; I^{\mathrm{o}}(\hbar\omega_2 - \epsilon) \\ &= \int d\epsilon\; \tilde{I}_{\mathrm{abs}}(\epsilon)\; I^{\mathrm{o}}(\hbar\omega_2 - \epsilon). \end{aligned} \tag{7.20}$$

Thus, the emission line has the shape of the occupied DOS convoluted with the mirrored product of the core hole Lorentzian and the unoccupied DOS. However, in case of incident energies $\hbar\omega_1$ well above the binding energy of the core electron the

influence of the DOS is not visible since well above E_F the DOS shows only small oscillations of about 10%.

This correlation, as stated by Eq. 7.20, between the unoccupied DOS and the shape of resonantly excited fluorescence spectra, not only allows one to calculate the shape of non $\vec{k}$-selective RIXS spectra, but it also permits to extract the shape of the unoccupied DOS from RIXS spectra if the DOS of the occupied states is known [Magd01].

7.5   The Line Shape of Radiative Auger Satellites

In the last section the shape of resonantly excited florescence lines has been calculated by taking into account the occupied and unoccupied DOS together with the corresponding transition matrix elements. Along similar lines the shape of radiative Auger satellites can be obtained. The states involved in the combined dipole monopole transition during the emission process giving rise to the radiative Auger satellites are depicted in Fig. 7.5. To calculate the line shape of the satellite line one extends Eq. 7.13 by introducing a third matrix element describing the monopole transition, according to Eq. 7.8:

$$M'_3 = \int d\vec{r}' \, u_{n'\vec{k}'}(\vec{r}') \, \hat{\mathbf{1}} \, u_{n\vec{k}}(\vec{r}'),\tag{7.21}$$

where $u_{n\vec{k}}(\vec{r}')$ and $u_{n'\vec{k}'}(\vec{r}')$ denote the lattice periodic parts of the corresponding Bloch wave functions (compare with Equations 1.20 and 1.21). This yields:

$$
\begin{aligned}
\frac{d^2\sigma}{d\omega_2 \, d\Omega} \quad \propto \quad & \sum_{n_i\vec{k}_i}\sum_{n\vec{k}}\sum_{n'\vec{k}'}\sum_{n_f\vec{k}_f} \left|M'_1(n_i,\vec{k}_i,1\mathrm{s})\right|^2 \mathrm{L}(E_{n_i\vec{k}_i} - E_{1\mathrm{s}} - \hbar\omega_1) \\
\times \quad & \left|M'_3(n,\vec{k},n',\vec{k}')\right|^2 \left|M'_2(n_f,\vec{k}_f,1\mathrm{s})\right|^2 \\
\times \quad & \delta(E_{n_i\vec{k}_i} + E_{n\vec{k}} - E_{n'\vec{k}'} - E_{n_f\vec{k}_f} - \hbar\omega_1 + \hbar\omega_2),\tag{7.22}
\end{aligned}
$$
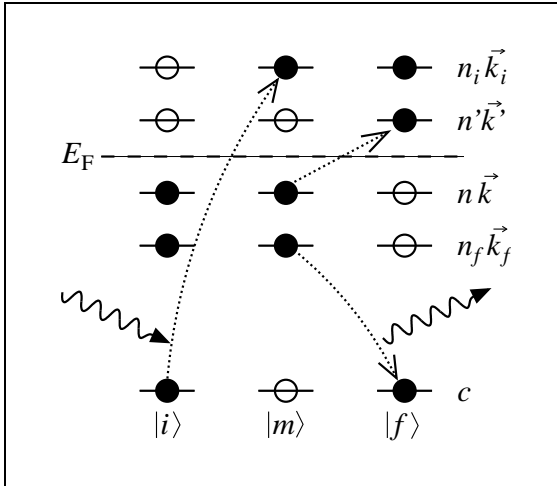
Figure 7.9: Single electron states involved in a radiative Auger process. The monopolar nonradiative secondary excitation occurs between $|n\vec{k}\rangle$ and $|n'\vec{k}'\rangle$. In the case of the KNN satellite, $|c\rangle$ is the 1s state, whereas $|n_f\vec{k}_f\rangle$ and $|n\vec{k}\rangle$ are valence states.

As in section 7.4 one transforms the sums into integrals, thereby introducing the densities of states $N^{\mathrm{o,u}}$, where the superscripts o and u denote occupied and unoccupied states, respectively. Additionally the states are split with respect to angular momentum:

$$
\begin{aligned}
\frac{d^2\sigma}{d\omega_2\,d\Omega} \;\propto\; & \int dE_i \int dE \int dE' \int dE_f \; \mathrm{L}(E_i - E_{1\mathrm{s}} - \hbar\omega_1) \\
& \times \; \sum_{l_i} |M_1'(E_i, l_i, 1\mathrm{s})|^2 \; N^{\mathrm{u}}(E_i, l_i) \\
& \times \; \sum_{l}\sum_{l'} |M_3'(E, l, E', l')|^2 \; N^{\mathrm{o}}(E, l) \; N^{\mathrm{u}}(E', l') \\
& \times \; \sum_{l_f} |M_2'(E_f, l_f, 1\mathrm{s})|^2 \; N^{\mathrm{o}}(E_f, l_f) \\
& \times \; \delta(E_i + E - E' - E_f - \hbar\omega_1 + \hbar\omega_2).
\end{aligned}
\tag{7.23}
$$

Treating the $\vec{A}\cdot\vec{p}$ operators of M_1' and M_2' in dipole approximation, the angular integrals of the matrix elements yield $\delta_{l_i,\mathrm{p}}$ and $\delta_{l_f,\mathrm{p}}$, respectively, whereas the $\hat{\mathbf{1}}$ operator in M_3' (see Eq. 7.21) results in $\delta_{l,l'}$. The radial integrals of M_1', M_2', and M_3' lead to the energy dependent radial matrix elements $M_{l_i}^{\mathrm{R}}(E_i)$, $M_{l_f}^{\mathrm{R}}(E_f)$, and $M_{l,l'}^{\mathrm{R}}(E, E')$ respectively, giving:

$$
\begin{aligned}
\frac{d^2\sigma}{d\omega_2\,d\Omega} \;\propto\; & \int dE_i \int dE \int dE' \int dE_f \; \mathrm{L}(E_i - E_{1\mathrm{s}} - \hbar\omega_1) \\
& \times \; \sum_{l_i} \left|M_{l_i}^{\mathrm{R}}(E_i)\right|^2 \delta_{l_i,\mathrm{p}} \; N^{\mathrm{u}}(E_i, l_i) \\
& \times \; \sum_{l}\sum_{l'} \left|M_{l,l'}^{\mathrm{R}}(E, E')\right|^2 \delta_{l,l'} \; N^{\mathrm{o}}(E, l) \; N^{\mathrm{u}}(E', l') \\
& \times \; \sum_{l_f} \left|M_{l_f}^{\mathrm{R}}(E_f)\right|^2 \delta_{l_f,\mathrm{p}} \; N^{\mathrm{o}}(E_f, l_f) \\
& \times \; \delta(E_i + E - E' - E_f - \hbar\omega_1 + \hbar\omega_2).
\end{aligned}
\tag{7.24}
$$

Performing the sums over l_i, l_f, and l' one gets:

$$
\begin{aligned}
\frac{d^2\sigma}{d\omega_2\,d\Omega} \;\propto\; & \int dE_i \int dE \int dE' \int dE_f \; \mathrm{L}(E_i - E_{1\mathrm{s}} - \hbar\omega_1) \\
& \times \; \left|M_{\mathrm{p}}^{\mathrm{R}}(E_i)\right|^2 N_{\mathrm{p}}^{\mathrm{u}}(E_i) \\
& \times \; \sum_{l} \left|M_{l,l}^{\mathrm{R}}(E, E')\right|^2 N_l^{\mathrm{o}}(E) \; N_l^{\mathrm{u}}(E') \\
& \times \; \left|M_{\mathrm{p}}^{\mathrm{R}}(E_f)\right|^2 N_{\mathrm{p}}^{\mathrm{o}}(E_f) \\
& \times \; \delta(E_i + E - E' - E_f - \hbar\omega_1 + \hbar\omega_2).
\end{aligned}
\tag{7.25}
$$

Now the radial matrix elements and the DOS depending on E_i and E_f can be combined into the energy dependent intensity factors $I_{\mathrm{p}}^{\mathrm{u}}(E_i)$ and $I_{\mathrm{p}}^{\mathrm{o}}(E_f)$, respectively.

Furthermore, the 1s binding energy E_{1s} is defined to be zero, and the integral over E_f is performed:

$$
\begin{aligned}
\frac{d^2\sigma}{d\omega_2\,d\Omega} \;\propto\;& \int\!dE_i \int\!dE \int\!dE' \int\!dE_f \; \mathrm{L}(E_i - E_{1s} - \hbar\omega_1)\, I_\mathrm{p}^\mathrm{u}(E_i)\, I_\mathrm{p}^\mathrm{o}(E_f) \\
\times\;& \sum_l \left| M_{l,l}^\mathrm{R}(E, E') \right|^2 N_l^\mathrm{o}(E)\, N_l^\mathrm{u}(E') \\
\times\;& \delta(E_i + E - E' - E_f - \hbar\omega_1 + \hbar\omega_2) \tag{7.26} \\
=\;& \int\!dE_i \int\!dE \int\!dE' \; \mathrm{L}(E_i - \hbar\omega_1)\, I_\mathrm{p}^\mathrm{u}(E_i)\, I_\mathrm{p}^\mathrm{o}(E_i + E - E' - \hbar\omega_1 + \hbar\omega_2) \\
\times\;& \sum_l \left| M_{l,l}^\mathrm{R}(E, E') \right|^2 N_l^\mathrm{o}(E)\, N_l^\mathrm{u}(E'). \tag{7.27}
\end{aligned}
$$

Next one can introduce the deviation from the incident energy $\epsilon = \hbar\omega_1 - E_i$ and the energy loss $\epsilon' = E - E'$ leading to:

$$
\begin{aligned}
\frac{d^2\sigma}{d\omega_2\,d\Omega} \;\propto\;& \int\!d\epsilon \int\!d\epsilon' \; \underbrace{\mathrm{L}(-\epsilon)\, I_\mathrm{p}^\mathrm{u}(\hbar\omega_1 - \epsilon)}_{I_\mathrm{abs}(-\epsilon)}\, I_\mathrm{p}^\mathrm{o}(\hbar\omega_2 + \epsilon' - \epsilon) \\
\times\;& \underbrace{\sum_l \int\!dE \; \left| M_{l,l}^\mathrm{R}(E, E - \epsilon') \right|^2 N_l^\mathrm{o}(E)\, N_l^\mathrm{u}(E - \epsilon')}_{S(\epsilon')} \tag{7.28} \\
=\;& \int\!d\epsilon \int\!d\epsilon' \; \tilde{I}_\mathrm{abs}(\epsilon)\, I_\mathrm{p}^\mathrm{o}(\hbar\omega_2 + \epsilon' - \epsilon)\, S(\epsilon') \propto I(\hbar\omega_2), \tag{7.29}
\end{aligned}
$$

where again the absorption intensity $I_\mathrm{abs}(-\epsilon) \equiv I^\mathrm{u}(\hbar\omega_1 - \epsilon)\mathrm{L}(-\epsilon)$ and the absorption intensity mirrored at zero $\tilde{I}_\mathrm{abs}(\epsilon) \equiv I_\mathrm{abs}(-\epsilon)$ have been defined and where the energy loss function $S(\epsilon')$ describing the monopole transition has been introduced.

With the substitutions

$$
\epsilon = a \qquad \hbar\omega_2 + \epsilon' = b \qquad \hbar\omega_2 = c \qquad \text{one yields}
$$

$$
\begin{aligned}
I(c) \;=\;& \int\!db \int\!da \; \tilde{I}_\mathrm{abs}(a)\, I_\mathrm{p}^\mathrm{o}(b - a)\, S(c - b) \\
=\;& \int\!db \; I_\mathrm{fluo}(b)\, S(c - b). \tag{7.30}
\end{aligned}
$$

Thus, the radiative Auger satellite apparently is the convolution of an energy loss function with the corresponding fluorescence line, which is already described in Section 7.4. Since the energy loss function contains the unoccupied DOS $N_l^\mathrm{u}(E - \epsilon')$ the satellite has a fine structure showing a XANES like behavior in the vicinity of its onset energy, as was shown by Åberg and Utriainen [Åber75].

Formulae similar to those above previously have been derived, e.g. by Pirenne and Longe [Pire64], as well as by Livins and Schnatterly [Livi88]. However, the approach

presented here makes no far-reaching assumption about the actual wave functions and the corresponding transition matrix elements. Therefore it is well suited for the semiempirical calculation of the satellites. Moreover, the satellite and its parent line can be treated within the same framework.

Although all ingredients of this algorithm, namely the densities of states and the dipolar and monopolar matrix elements, can be obtained from ab initio calculations, the exact evaluation of Eq. 7.28 is complicated by the fact that the states $|i\rangle$, $|m\rangle$, and $|f\rangle$ contain zero, one, and two hole states, respectively. Thus, for each hole configuration one separate band structure calculation has to be performed, yielding the necessary densities of states. Moreover, matrix elements between states with different hole configurations have to be calculated. This is especially important in the case of the monopolar matrix element $M_{l,l}^{\mathrm{R}}$, which vanishes if the states involved have the same hole configuration.

Therefore, certain approximations are necessary. In the following the influence of the unoccupied DOS N_l^{u} on the energy loss function S is neglected and one single state for N_l^{o} is assumed. The monopolar matrix element $M_{l,l}^{\mathrm{R}}$ can be approximated by an exponential, which is supported by findings of Livins and Schnatterly [Livi88], Krause *et al.* [Krau68], and Pirenne and Longe [Pire64].

7.6 The Line Shape of the Resonantly Excited Cu K$\beta_{1,3}$ Fluorescence Line

A series of RIXS spectra of the Cu K$\beta_{1,3}$ fluorescence line has been measured at the beamline G3 of the HASYLAB, by using a Si 553 analyzer crystal in the 1m Rowland spectrometer which is described elsewhere [Schü95, Wohl00]. The incident radiation was monochromatized by a Ge 311 double crystal monochromator. The over-all energy resolution was about 1 eV. The energy of the incident photon has been varied between the 1s binding energy of Cu (8979 eV) and 9130 eV. Two of these spectra are shown in Fig. 7.10 and 7.12.

The K$\beta_{1,3}$ fluorescence line of Cu can be subdivided into four main contributions, as shown in Fig. 7.10. The fluorescence line is dominated by the diagram lines Kβ_1 and Kβ_3 that are separated by a spin orbit splitting of 2.5 eV, in accordance with other values found in the literature (e.g. see Table VI of [Deut95]). In the range of the low and high energy tails of the K$\beta_{1,3}$ line the Kβ' and Kβ'' satellite lines arise, respectively. These are due to shake processes during the absorption of the incoming photon, as found by M. Deutsch *et al.* [Deut95]. From multiplet calculations they have been attributed to 3d hole spectator states. In Appendix C this finding is confirmed by observing the intensity of the Kβ' and Kβ'' satellites as a function of the incident energy. The slowly decreasing low energy tail of the K$\beta_{1,3}$ fluorescence line originates from the KMN radiative Auger satellite, which arises from a shake process of a valence electron during the radiative transition of a 3p electron into the 1s hole.

The fit was performed according to Eq. 7.20. The occupied states $I^{\mathrm{o}}(E)$ consist of a
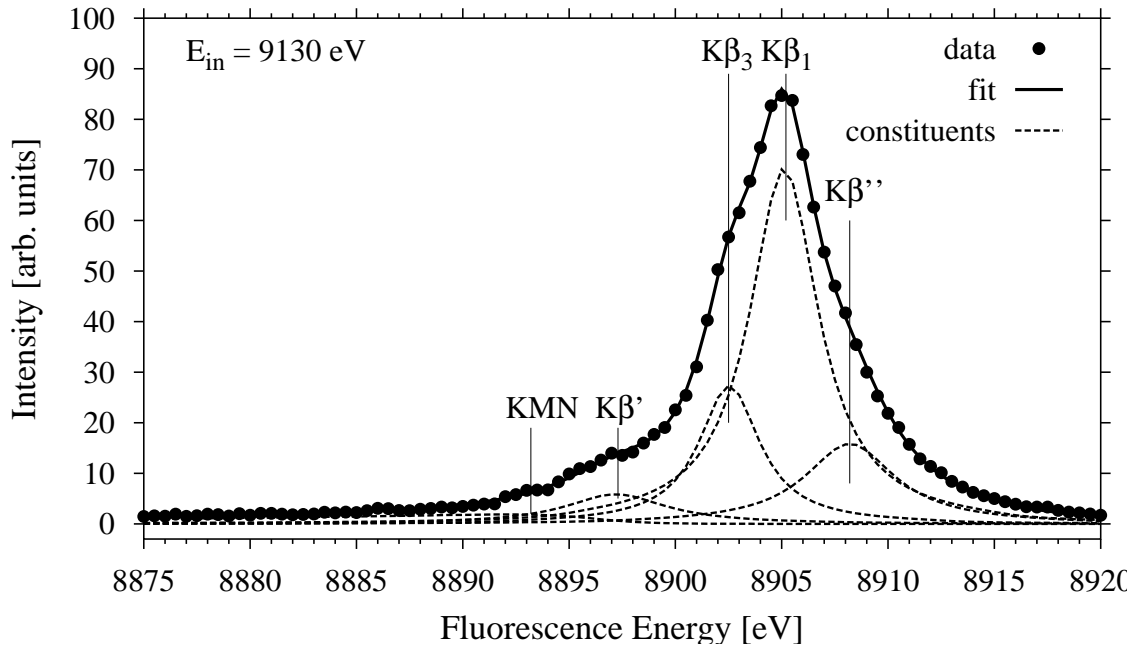
Figure 7.10: Fit of the Cu $K\beta_{1,3}$ diagram lines together with the $K\beta'$ and the $K\beta''$ satellite lines. The energy of the incoming photons is about 150 eV larger than the 1s binding energy.

sum of four Lorentzians. Each of these describes one diagram or satellite line. The Lorentzians account for the multiplet splitting as well as for the lifetime broadening of the final state. A Lorentzian of FWHM=1.55 eV accounts for the lifetime of the 1s core hole in Cu [Zsch89]. The function $I^{\mathrm{u}}(\hbar\omega_1)$ corresponds to the DOS of the unoccupied p-states multiplied by the corresponding matrix element. As shown in Fig. 7.11, $I^{\mathrm{u}}(\hbar\omega_1)$ has been extracted from a measured XANES spectrum by deconvolution from the core Lorentzian. The deconvolution has been done by fitting equidistanly distributed Lorentzians ($\Delta E = 0.5$ eV) with $\Gamma = 1.55$ eV to the measured XANES spectrum. The intensities of the Lorentzians, being the only variational parameters in the fit, yield the absorption intensity $I^{\mathrm{u}}(\hbar\omega_1)$. The energetic width of the incoming radiation, which is about 1 eV, has not been removed. Before performing the convolution, I_{abs} has been normalized to unity.

To describe the KMN radiative Auger satellite, an exponential multiplied by an arctan function has been used:

$$I_{\mathrm{KMN}}(E) = I\, e^{d(E-E_0)} \left[0.5 - \frac{1}{\pi} \arctan\left(\frac{(E-E_0)}{w} \right) \right] + b. \qquad (7.31)$$

The decay factor of the exponential results in $d = 0.041$ 1/eV, the center position E_0 is 8895.9 eV and the width of the arctan is $w = \Gamma/2 = 2.6$ eV, where Γ is the energetic width of the Cu $K\beta_{1,3}$-line. For details of the fit procedure see Appendix C.

The parameters obtained by the fit procedure are resumed in Table 7.1. Comparison to the values found by M. Deutsch and coworkers [Deut95] shows that the relative
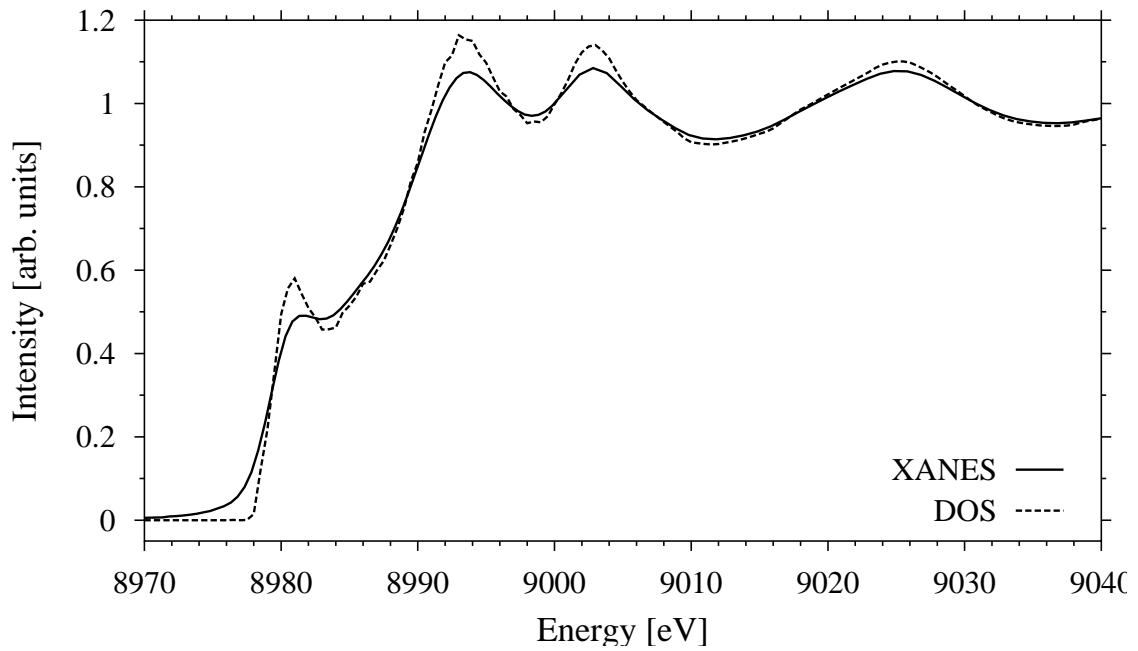
Figure 7.11: XANES and $I^{\mathrm{u}}(\hbar\omega_1) = DOS \cdot ME$ at the Cu K edge, as obtained from the XANES by deconvolution from a Lorentzian of FWHM = 1.55 eV.

intensities agree up to a few percent. The positions of the Kβ_1 and Kβ_3 lines differ by 0.40 eV and 0.45 eV, respectively, due to a different calibration, whereas the positions of the Kβ' and the Kβ'' satellite lines show a small but not systematic deviation. The widths of the diagram lines in the present fit are about 1.5 eV smaller due to the fact that the core Lorentzian is separately accounted for. However, the widths of the Kβ' and the Kβ'' satellite lines in the present work are significantly

Line	Parameter	this work	Deutsch	Difference
Kβ_1	E[eV]	8905.11	8905.51	0.40
	Γ[eV]	2.39	3.72	1.33
	I rel.	0.72	0.72	0%
Kβ_3	E[eV]	8902.65	8903.10	0.45
	Γ[eV]	1.89	3.43	1.54
	I rel.	0.31	0.32	3%
Kβ'	E[eV]	8897.20	8897.06	-0.14
	Γ[eV]	4.20	7.62	3.42
	I rel.	0.07	0.07	2%
Kβ''	E[eV]	8908.20	8908.45	0.25
	Γ[eV]	3.56	6.63	3.07
	I rel.	0.20	0.21	5%

Table 7.1: Parameters found for the K$\beta_{1,3}$ fluorescence line and for the Kβ' and the Kβ'' satellite lines in comparison with the parameters found by Deutsch [Deut95].
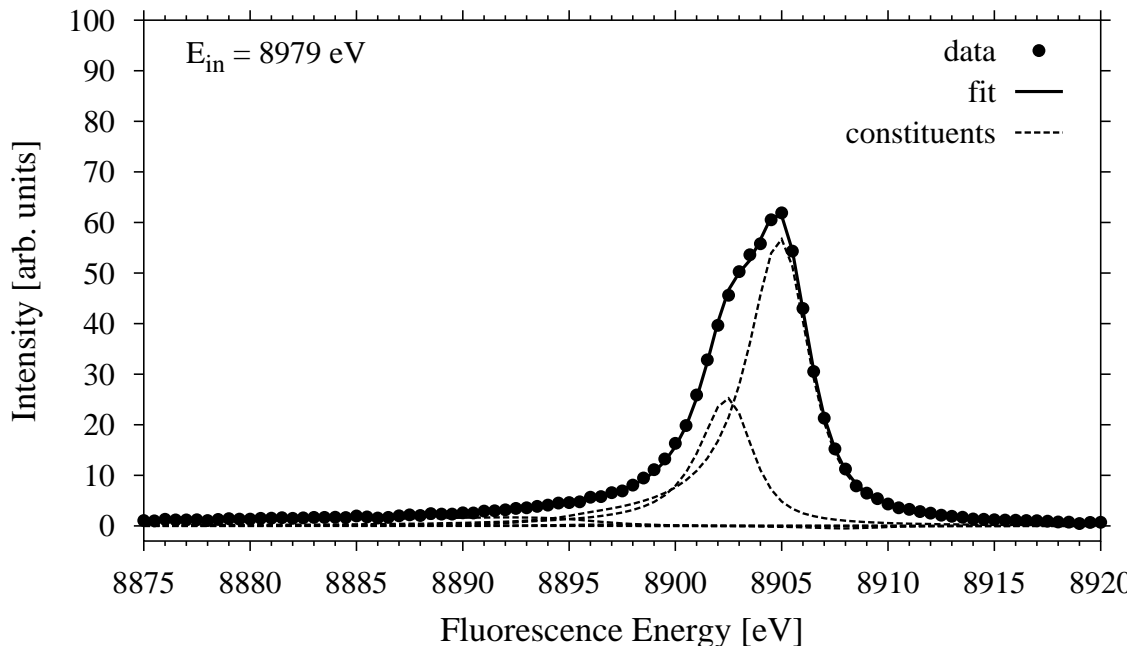
Figure 7.12: Fit of the Cu $K\beta_{1,3}$ fluorescence line excited at the 1s binding energy. The $K\beta'$ and the $K\beta''$ satellite lines have disappeared. The diagram contributions to the fluorescence line are strongly asymmetric due to the influence of the unoccupied DOS.

smaller than the values found by Deutsch, even if the different treatment of the core Lorentzian is considered.

As can be seen from Fig. 7.10 the agreement between measured data and the fit curve is excellent. However, at an incident energy of about 150 eV above the absorption edge, the influence of the unoccupied DOS on the shape of the fluorescence spectrum is not significant. This is no longer true at incident energies close to the absorption edge. In Fig. 7.12 a spectrum recorded at the 1s binding energy $E_K = 8979$ eV is shown. The $K\beta'$ and the $K\beta''$ satellite lines have disappeared and the fluorescence line is strongly asymmetric due to the influence of the unoccupied DOS. Again the agreement between the measured spectrum and the fit curve is very good, confirming the validity of the algorithm for the calculation of resonantly excited fluorescence spectra.

7.7   The KMM Radiative Auger Satellite of Cu

The KMM radiative Auger satellite of Cu has been measured at beamline W2 (HARWI) of the HASYLAB, making use of the Si 311 sagittally focussing double crystal monochromator. The fluorescence radiation was analyzed with the 1m Rowland spectrometer. In order to cover a significant fraction of the extended satellite structure, the 642 reflection of a Si 531 analyzer crystal has been used, with an asymmetry angle of 6.35°, and allowing for a covered energy from 8600 eV to 9100 eV. The over-all energy resolution was 1.5 eV.
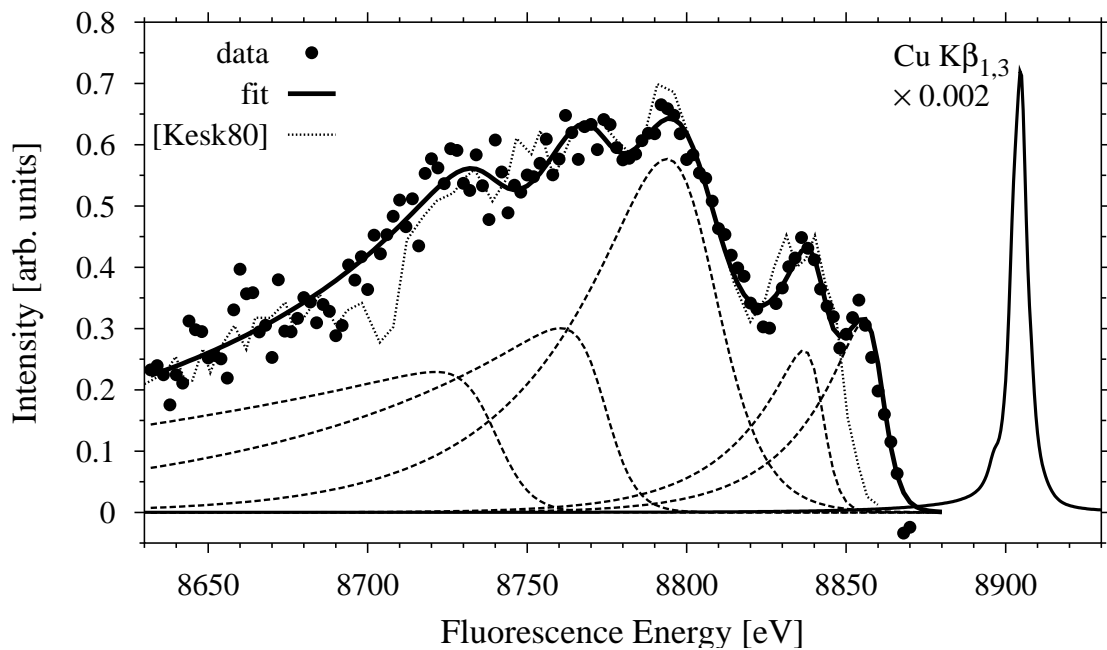
Figure 7.13: The measured Cu KMM radiative Auger satellite lines (dots) together with a fit function (solid line) consisting of five shark fin functions (dashed lines) according to Eq. 7.31. A measured spectrum obtained by Keski-Rahkonen and Ahopelto [Kesk80] is shown as a dotted line. For comparison, the scaled down Cu K$\beta_{1,3}$ spectrum is given as a thin solid line.

After the spectral decompositon of the Cu K$\beta_{1,3}$ fluorescence spectrum, its low energy tail has been extrapolated into the energetic region of the KMM radiative Auger satellite. Its subtraction leads to the pure KMM spectrum as shown in Fig. 7.13.

In comparison to the KMM spectrum obtained by Keski-Rahkonen and Ahopelto [Kesk80] a significantly better resolution and a slightly better statistical accuracy could be achieved. By means of a fit procedure the KMM satellite has been decomposed into five shark fin functions according to Eq. 7.31, given by the dashed lines. The respective parameters are summarized in Table 7.2.

The width of the shark fin functions are expected to be constant since they are

Line	I	w [eV]	d [1/eV]	E_0 [eV]
1	0.453	2.54	0.0492	8860.4
2	0.374	2.42	0.0455	8841.8
3	0.958	7.23	0.0284	8803.5
4	0.370	4.36	0.0115	8774.7
5	0.262	5.35	0.0056	8739.7

Table 7.2: Parameters for the KMM radiative Auger satellite lines of Cu. I, w, d, and E_0 are the intensity, the width, the decay factor, and the onset energy, respectively, of each shark fin, according to Eq. 7.31.

Shell	K	M_1	M_2	M_3	M_4	M_5	$M_{2,3}$	$M_{4,5}$
Cu	8979.0	120.0	75.3	72.8	1.8	1.5	73.6	1.6
Zn	9659.0	137.0	87.6	85.6	7.9	8.0	86.3	8.0

Table 7.3: Binding energies of the K and M shells in Cu and Zn [Zsch89], together with the averaged $M_{2,3}$ and $M_{4,5}$ energies, taking into account the occupation numbers.

connected to the width of the parent line. Only the width of he first two shark fins agree with the FWHM of the Cu $K\beta_{1,3}$ fluorescence line, whereas the widths of the other fins are too large. This is attributed to the overlap of several radiative Auger satellites within the same energy regime. The decay factor steadily decreases with decreasing onset energy.

In order to assign certain final states to the different onset energies, the KMM energies have been calculated within the frozen core and within the Z+1 approximation according to Eq. 7.4 and 7.5, respectively. Therein the energies as listed in Table 7.3 (taken from [Zsch89]) have been used and $j - j$ coupling has been applied by making use of the averaged 3p- and 3d-energies $M_{2,3}$ and $M_{4,5}$. Moreover, the onset energies can be derived from measured LMM Auger energies according to

$$\begin{aligned} E(\text{KMM}) &= E(\text{K}\alpha_1) + E(\text{L}_3\text{M}_i\text{M}_j) \\ &= E(\text{K}\alpha_2) + E(\text{L}_2\text{M}_i\text{M}_j) \quad \text{where} \quad i, j = 1, 2, \ldots, 5. \quad (7.32) \end{aligned}$$

These onset energies taken from [Kesk80] as well as the calculated energies from the Z+1 and frozen core approximation are summarized in Table 7.4. They are compared to the measured KMM satellite in Fig. 7.14.

As expected, the energies predicted by the frozen core approximation differ significantly from the values calculated within the Z+1 approximation. The latter agree fairly well with the energies obtained from measured LMM energies on which the assignment of the lines will be founded. Apparently the onset energies of the third

	KM_1M_1	$KM_1M_{2,3}$	$KM_{2,3}M_{2,3}$	$KM_1M_{4,5}$
LMM	8721.5	8765.1	8813.9	8841.5
		8778.1	8820.5	8845.5
Z+1	8722.0	8768.4*	8819.1	8840.4*
FC	8739.0	8785.4	8831.8	8857.4

Table 7.4: Onset energies of the KMM radiative Auger satellites obtained from measured LMM lines and calculated within frozen core and Z+1 approximation. The spin orbit splitting has been neglected by making use of the averaged energies $M_{2,3}$ and $M_{4,5}$ taken from the last two colmns of Tab. 7.3. In the energies marked with * $E(M_1)$ was chosen to be the 3s binding energy in Zn.
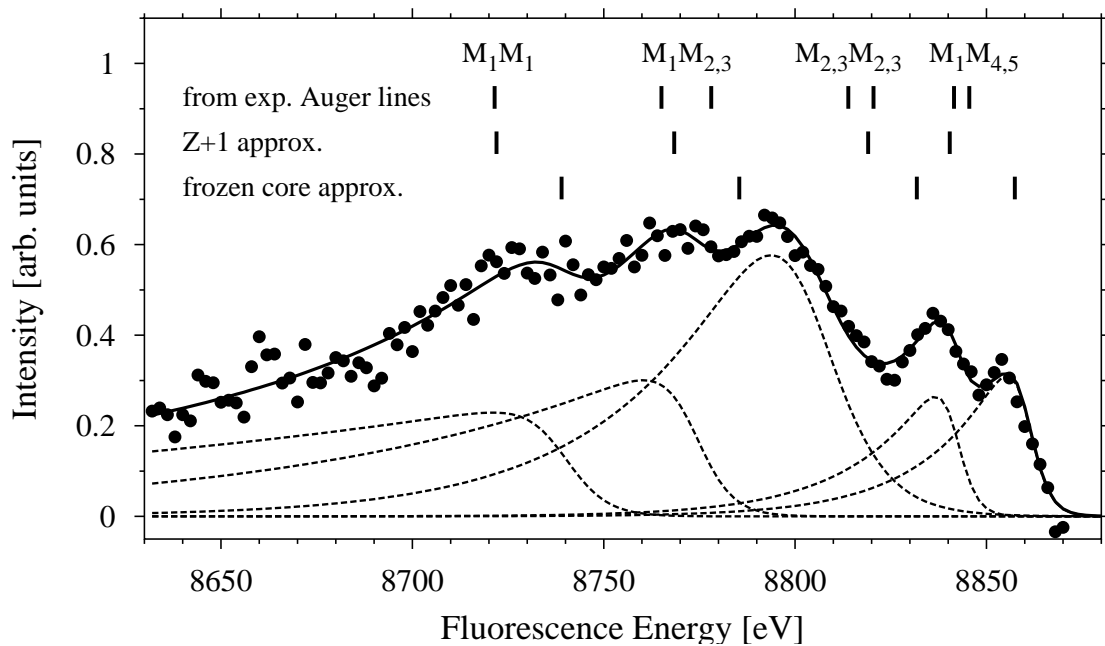
Figure 7.14: Calculated onset energies compared to the measured Cu KMM radiative Auger satellite line. The vertical bars indicate the calculated onset energies obtained within the frozen core (bottom row) and Z+1 approximation (middle row). Onset energies calculated from LMM Auger spectra [Kesk80] are shown in the top row. The shown spectra are identical to those in Fig. 7.13.

and the fourth shark fin can be assigned to $M_{2,3}M_{2,3}$ and $M_1M_{2,3}$ final states, respectively. The second shark fin belongs to a $KM_1M_{4,5}$ transition, stemming from a quadrupolar 3d→1s radiative decay with the simultaneous excitation of a 3s electron. However, the fifth shark fin, if at all, could be assigned to a M_1M_1 final state which is forbidden in a radiative Auger process. Moreover, the first shark fin could not be assigned.

For a more detailed analysis of the KMM radiative Auger satellite, considering all final states known from LMM Auger measurements and including the unoccupied DOS, data with a larger signal to noise ratio have to be obtained. Nevertheless, the general shape of the radiative Auger satellites can be approximated by the shark fin function, which will be used to account for the KNN satellite, present in the valence fluorescence spectra.

7.8   The KNN Radiative Auger Satellite of Cu

As shown in Section 7.5, the energy loss function S and thus the shape of the radiative Auger satellites depends on the DOS of the occupied states $N_l^o(E)$, the DOS of the unoccupied states $N_l^u(E)$, and the monopole matrix element $M_{l,l}^R(E, E')$ mediating the transition between these states.

The valence electrons of Cu have mainly d-character. As it is known from the band structure calculation 10 3d electrons oppose to 0.6 4p and 0.4 4s electrons.

From the supercell calculation one can conclude that within the valence band only the states of the 3d electrons change upon the creation or annihilation of the 1s hole, whereas the 4s- and 4p-states remain widely unaltered (see Chapter 5). Since those states that change much upon the annihilation of the core hole give rise to a large monopolar matrix element (see Page 78), within the valence band only the 3d electrons contribute significantly to the monopole excitation of the radiative Auger process[1].

Due to the final states rule, the electron configuration present after the annihilation of the core hole has to be considered in the calculation of the energy loss function. More precisely, the final state of the KNN satellite consists of one hole in the 4p-states, originating from the radiative part of the transition, and of one 3d hole created during the monopolar transition. Due to the delocalization of the 4p-states, the influence of the 4p hole can be neglected, whereas the 3d-states have to be shifted by about 1 eV to lower energies in the presence of a 3d hole, as was shown in Chapter 6. If the fine structure of the 3d-DOS is neglected, the DOS of the occupied states $N_{\rm d}^{\rm o}$ may be approximated by a Gaussian with a FWHM of 2 eV positioned at 3.5 eV below the Fermi energy (see Fig. 6.4), wherein the shift of -1 eV due to the screening of the 3d hole already is included.

As in the case of the other radiative Auger satellites, the DOS of the unoccupied states will be considered to be constant, and for the matrix element again an exponential is used. Thus, the loss function S is the matrix element convoluted with the Gaussian describing the occupied 3d-DOS.

According to Eq. 7.30 the satellite line can be calculated as the convolution of the energy loss function with a pure valence fluorescence spectrum. The shape of the fluorescence spectrum in the energy range between the K$\beta_{1,3}$ and the K$\beta_{2,5}$ line is the sum of the high energy tail of the K$\beta_{1,3}$ line, the KNN satellite line, and the K$\beta_{2,5}$ line. The fit yields a decay factor of 0.03788 1/eV in the exponential, in agreement with the decay factors of the KMN and the KMM satellites. The result is depicted in Fig. 7.15 showing good agreement between the fit function and the measured spectrum.

Conclusion

The diagram lines are accompanied by a variety of satellite lines. The low energy satellites are due to double excitation processes during the emission of a fluorescence photon. This radiative decay is complementary to the nonradiative Auger effect and thus is named radiative Auger effect. From the variety of radiative Auger satellites the KMM, the KMN, and the KNN satellites from Cu have been observed. The low energy tail of the valence fluorescence spectra is dominated by the KNN radiative Auger satellite, partly obscuring the shape of the Bloch $\vec{k}$-selective valence spectra. This satellite has been accounted for by a semiempirical model which was derived from the resonant double differential scattering cross section. The model involves

---

[1]Therefore, the Auger satellite to the valence line correctly must be named KMN. In analogy, the Auger satellite dominating the low energy tail of the Cu K$\beta_{1,3}$ line in reality is a KMM satellite (see Fig. 7.10). But in order to maintain a concise nomenclature the prior notation will be kept.
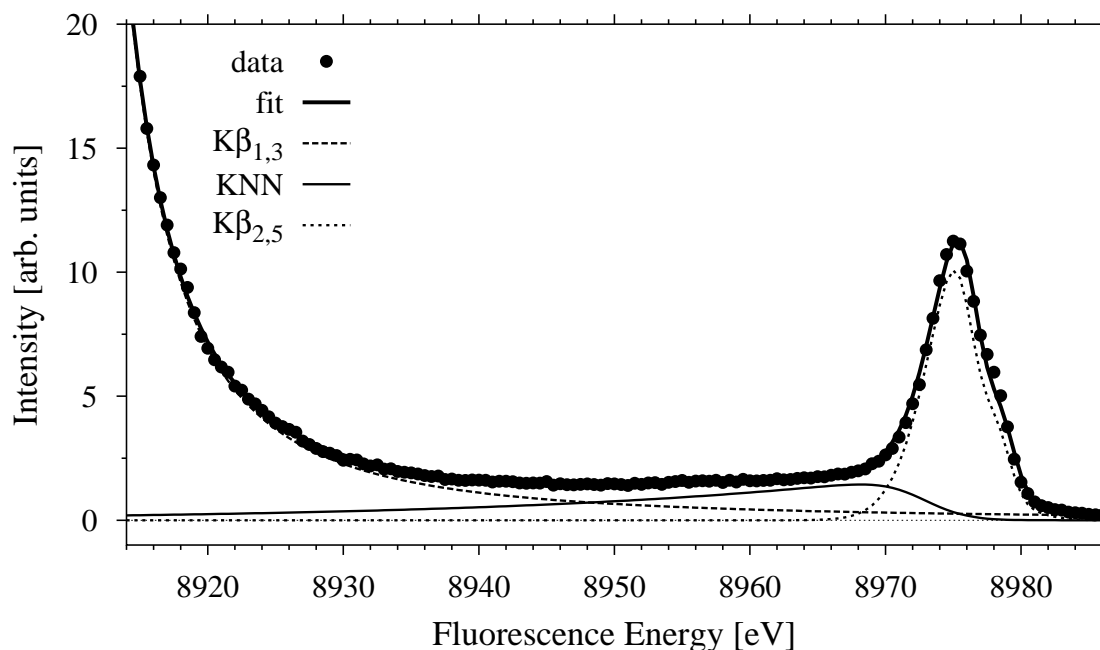
Figure 7.15: The radiative Auger satellite to the valence fluorescence line of Cu (thin solid line) together with the high energy tail of the Cu $K\beta_{1,3}$ line (dashed) and with the Cu $K\beta_{2,5}$ valence line (dotted) amounting to the thick solid line, in agreement with the measured spectrum (dots).

the convolution of an energy loss function with the parent line of the respective satellite. Investigating the KMN and KMM radiative Auger satellites this model has been confirmed.

For the first time the KNN satellite of the late 3d elements has been investigated. The relative intensity of the KNN satellite decreases with increasing atomic number Z as it is the case for other transition as the KMM and the KLL satellites.

From this it is concluded that the treatment evolved in this Chapter correctly describes the over-all shape of the radiative Auger satellites.

Chapter 8

Bloch $\vec{k}$-Selective RIXS from Copper

In contrast to the RIXS experiment on NiAl as described in Chapter 3, in the experiment on Cu not only momentum transfer vectors along one high symmetry direction were investigated, but a set of reduced $\vec{q}$-vectors was chosen to cover the whole Brillouin zone in an equidistant manner. The smallest set of $\vec{q}$-vectors complying with this requirement, consists of the six high symmetry points Γ, Δ, X, W, Σ, and L. However, since the measurement at the Γ-point, corresponding to a Bragg reflection and thus provoking a very intense quasi-elastic line, is experimentally not feasible, three neighbouring points on the ⟨100⟩, ⟨110⟩, and ⟨111⟩ axes have been considered instead. The actually used values of $\vec{q}_{\mathrm{red}}$ are depicted in Fig. 8.1.

Figure 8.1: The irreducible wedge of the Brillouin zone of fcc lattices. The $\vec{q}$ vectors considered in the experiment are marked by circles.
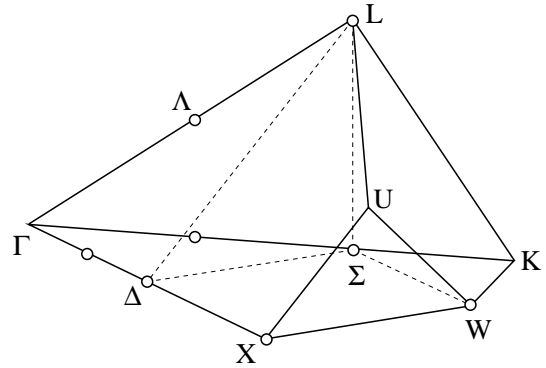
As in the experiment on NiAl the reduced momentum transfer vectors $\vec{q}_{\mathrm{red}}$ have been extended by a reciprocal lattice vector to obtain larger momentum transfer vectors $\vec{q}_{\mathrm{abs}}$ resulting in scattering angles close to 90°. Thereby the quasi-elastic Rayleigh line is widely suppressed. Fig. 8.2 clarifies the location of the irreducible wedge of the Brillouin zone that was actually used in the experiment. The Γ-point of this Brillouin zone is centered at the ⟨400⟩ reciprocal lattice vector.

The surface of the ⟨100⟩ single crystal sample was oriented perpendicular to the momentum transfer vector $\vec{q}$, thereby making one ⟨100⟩ axis parallel to $\vec{q}$. Moreover, by means of a Laue pattern, another ⟨100⟩ axis was adjusted to be perpendicular to the scattering plane. Thus, the values of $\vec{q}$ parallel to the ⟨100⟩ axis can be reached by choosing the scattering angle Θ according to Tab. 8.1 and by choosing both the inclinations between the sample and the incoming and outgoing x-ray beam equal to Θ/2. To access the other values of $\vec{q}$, the sample additionally must be tilted horizontally by α (see Fig.8.2) and vertically by β, as also denoted in Tab. 8.1.
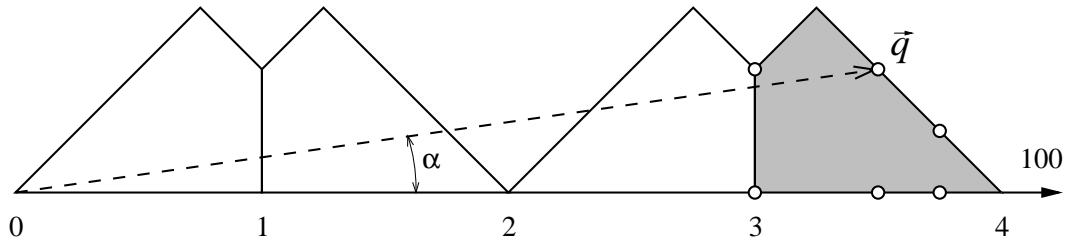
Figure 8.2: Location of the irreducible wedge of the Brillouin zone used in the RIXS experiment on Cu. The $\vec{q}$ vectors that have been accounted for are marked by the circles.

The experiment has been performed at beamline ID16 of the ESRF, making use of the Rowland spectrometer [Schü95, Kao96], equipped with a Si 642 analyzer crystal. The incoming beam was monochromatized by the Si 111 double crystal pre-monochromator. To stabilize the energy of the incident photons and to further narrow down the energetic width of the photon beam a Si 333 channel cut crystal was used. The over-all energy resolution was limited to 1.4 eV by the analyzer crystal. For each of the $\vec{q}$-vectors specified above, RIXS spectra at five different incident energies have been measured, namely at 2, 4, 6, 8 , and 10 eV above the 1s binding energy of Cu corresponding to 8979 eV. The full set of spectra is shown in Appendix D.

In Fig. 8.3 the impact of the three corrections on the calculated $\vec{k}$-selective spectra of Cu is demonstrated. In panel a) the valence line without the KNN radiative Auger satellite and without the 3d→1s quadrupolar transitions is shown. In this case the low energy region is not reproduced by the calculated spectrum. If the KNN satellite is accounted for, the over-all agreement is improved significantly, as it is shown in panel b). However, both tails of the valence fluorescence line are overemphasized in the calculated spectrum. This problem is overcome by additionally including the 3d→1s quadrupolar transitions. In panel c), the high and low energy tails are then correctly reproduced by the calculated spectra, but the position of the main peak is

$\vec{q}_{\text{red}}$ $[2\pi/a]$	$\vec{q}_{\text{abs}}$ $[2\pi/a]$	$|\vec{q}_{\text{abs}}|$ [a.u.]	Θ [°]	α [°]	β [°]
$1/4$, 0 , 0	3.75 , 0.00 , 0.00	3.45	91.56	0.00	0.00
$1/4$, $1/4$, 0	3.75 , 0.75 , 0.00	3.46	91.83	3.81	0.00
$1/4$, $1/4$, $1/4$	3.75 , 0.75 , 0.75	3.47	92.09	3.81	3.81
$1/2$, 0 , 0	3.50 , 0.00 , 0.00	3.22	83.97	0.00	0.00
$1/2$, $1/2$, 0	3.50 , 0.50 , 0.00	3.26	85.02	8.13	0.00
$1/2$, $1/2$, $1/2$	3.50 , 0.50 , 0.50	3.29	86.07	8.13	8.05
1 , 0 , 0	3.00 , 0.00 , 0.00	2.76	69.97	0.00	0.00
1 , $1/2$, 0	3.00 , 0.50 , 0.00	2.80	71.08	9.46	0.00

Table 8.1: Experimentally chosen reduced and absolute values of the momentum transfer $\vec{q}$ and the corresponding scattering angles for Cu, as well as the angles α and β defining the orientation of the sample.
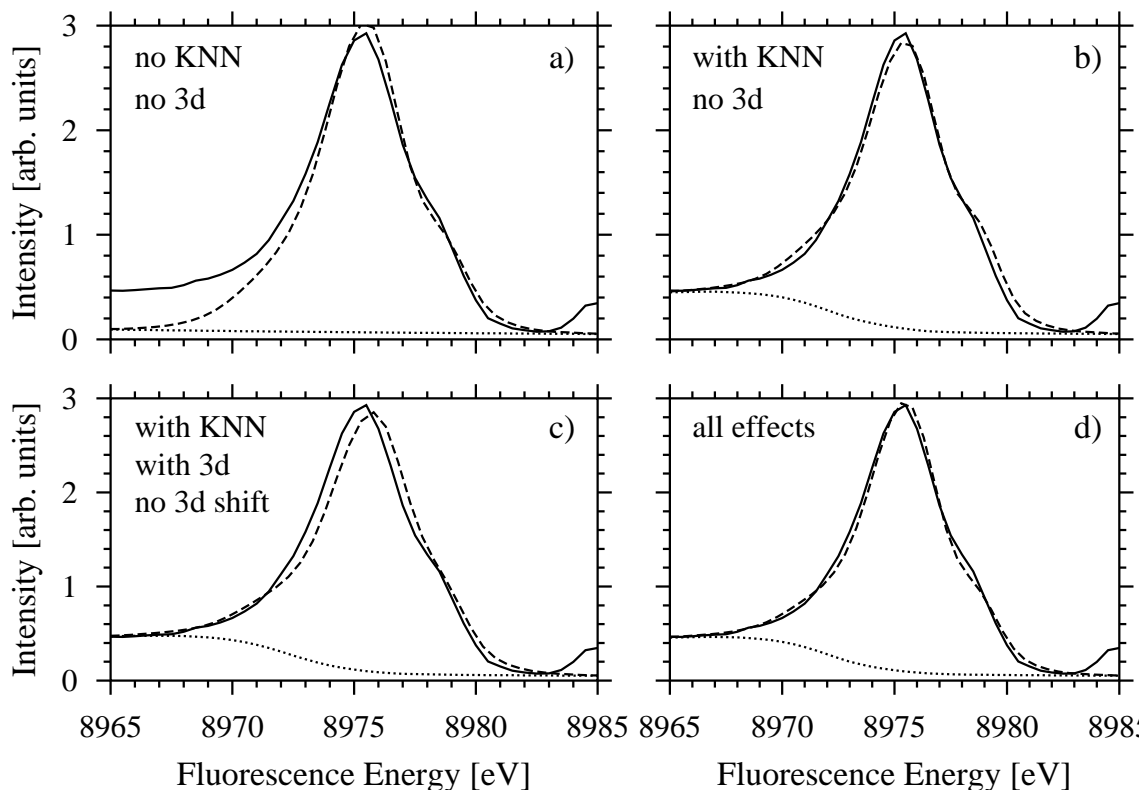
Figure 8.3: Impact of the three corretions on the calculated Bloch $\vec{k}$-selective RIXS spectra of Cu. The calculated spectra (dashed lines) are compared to the measured ones (solid lines). Also given is the sum of the KNN satellite and the high energy tail of the Cu $K\beta_{1,3}$ fluorescence line (dotted lines). The measured spectrum has been obtained at $\vec{q}_{\mathrm{red}} = \langle 1|0.5|0 \rangle \cdot \pi/a$ and at $\hbar\omega_1 = E_{\mathrm{K}} + 6\ eV = 8985\ eV$. For further explanations see text.

still not matching the measured spectrum. By considering the shift of the 3d states towards higher binding energies, which is due to the screening of the 3d hole, also the main peak position is properly accounted for. The corresponding calclulated spectrum including all three effects is depicted in panel d). Compared to panel b) the agreement between the calculated and the measured spectrum is significantly improved, emphasizing the importance of the proper consideration of the 3d states in the case of RIXS valence spectra from 3d elements. Thus, all three effects are important in order to correctly describe the shape of Bloch $\vec{k}$-selective RIXS spectra from Cu.

In Fig. 8.4 a series of RIXS spectra recorded at different incident energies and at a momentum transfer $\vec{q}_{\mathrm{red}} = \langle 1|0.5|0 \rangle \cdot \pi/a$ corresponding to the Γ-W distance is compared to calculated RIXS spectra. In the calculation the 3d-states of Cu have been accounted for as described in Chapter 6. For both the 4p→1s and the 3d→1s transitions the energy dependent radial matrix elements as well as the weight factors from the angular matrix elements have been used. Moreover, the 3d states have been shifted by 1 eV towards higher binding energies, accounting for the strong screening of the 3d hole present in the final state in case of a quadrupolar transition. The
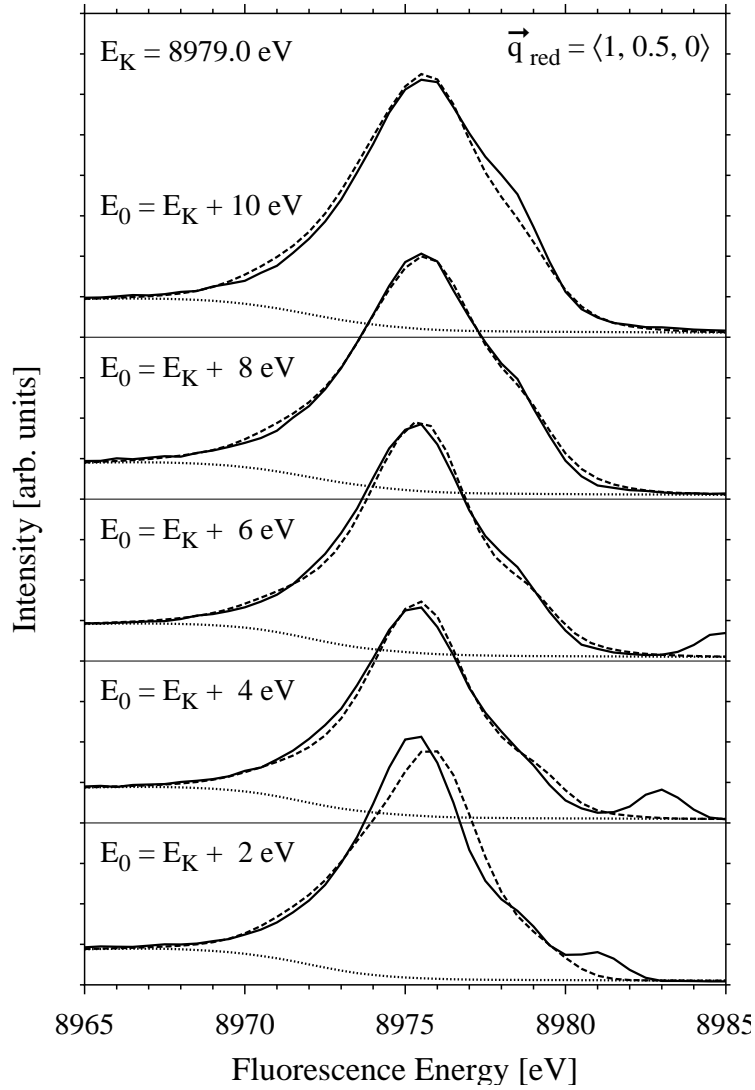
Figure 8.4: Measured (solid lines) and calculated (dashed lines) Bloch $\vec{k}$-selective RIXS spectra of Cu together with the KNN radiative Auger satellites (dotted lines). The incident energies are given with respect to the K edge of Cu. The reduced momentum transfer $\vec{q}_{\mathrm{red}}$ is equal to the Γ-W distance. The peaks at 8981, 8983, and 8985 eV are due to quasi-elastic scattering.

dotted lines depict the high energy tail of the Cu $K\beta_{1,3}$ line as well as the radiative Auger satellites, calculated according to Chapter 7.

Although the calculated spectra are in reasonable agreement with the measured ones in general, some details are not reproduced in the calculation. The shoulder at the high energy side of the spectrum recorded at 10 eV above the K edge is more prominent in the measured spectrum, and the main peak of the spectrum excited at 2 eV above the edge is not at the correct position in the calculated spectrum. The origin of these differences, also appearing in the spectra recorded at the other values of the momentum transfer $\vec{q}$, is unclear and requires further investigation.

An explanation for these differences may be found in the difficulty to treat correctly the 3d hole in the final state of the quadrupolar transitions. The screening of the 3d hole surely has more drastic consequences than a mere shift of the 3d band. In fact also a band narrowing, as observed at the 3d states in the presence of the 1s core hole, is to be expected. For a satisfactory treatment of the 3d hole final state a $3d^9$ configuration has to be enforced, as it has been done in Ga, Ge, and As. However, within the LAPW algorithm, this requires to treat the 3d states as core states, resulting in dipersion-less 3d bands surely being not appropriate for the late 3d elements. Thus, the 3d hole final states cannot be properly treated within the standard WIEN package. Additionally, interactions between the excited electron in the conduction band and the 4p or 3d hole in the final state may give rise to additional corrections, as they have been reported for RIXS in the soft x-ray regime [Shir01].

More generally, apart from the difficulty to account correctly for the hole states in the final state of the scattering process the remaining differences between the calculated and the measured spectra may indicate that the calculated band structure differs from the actual band structure of Cu.

Conclusion

In this thesis, the validity of the Bloch $\vec{k}$-momentum conservation of RIXS in the hard x-ray regime and its applicability to metallic samples have been demonstrated by probing the K edge of Cu and the K edge of Ni in NiAl. The shape of resonantly excited valence fluorescence spectra does not only depend on the incident energy but also on the size and the direction of the momentum transfer $\vec{q}$ if hard x-rays are used. Thus, in the hard x-ray regime more parameters can be varied in the experiment than in the soft x-ray regime, where only the incident energy determines the shape of the spectra. This is a clear advantage of hard x-rays.

Four effects influencing the Bloch $\vec{k}$-conserving RIXS process have been investigated: the destruction of the $\vec{k}$-conservation due to electron-phonon interaction in the intermediate state, the screening of the 1s core hole present in the intermediate state, the contribution of 3d→1s quadrupolar transitions in the fluorescence process, and the KNN radiative Auger satellite partly obscuring the valence fluorescence line.

There is no measurable contribution from non-$\vec{k}$-conserving processes in the case of Cu. Indeed, only a small $\vec{k}$-unselective fraction of a few percent is expected, since the lifetime of the 1s core hole in Cu is shorter than the electron-phonon interaction time, i.e. the energetic lifetime width Γ_{1s} is larger than the Debye energy $\hbar\omega_D$. Thus, in the case of hard x-rays a $\vec{k}$-unselective fraction does not have to be considered, faciliating the interpretation of the spectra.

For a determination of the $\vec{k}$-selective fraction free of doubt, experimental data with a better signal-to-noise ratio have to be obtained . Moreover, temperature dependent measurements of Bloch $\vec{k}$-selective RIXS spectra in the soft x-ray regime, where significant $\vec{k}$-unselective contributions exist, are desirable.

Due to the final states rule only the absorption part of the RIXS process can be affected by the core hole present in the intermediate state. By means of a supercell calculation of Cu it was found that the 1s core hole is completely screened by the core states and by the strongly localized 3d electrons. The 4p states, dominating the RIXS process via the dipole selection rules, remain largely unaffected. The good agreement between calculated and measured XANES spectra is only slightly improved by the consideration of the core hole. Therefore, the ground state electronic band structure can be legitimately used to calculate RIXS spectra in the case of RIXS at the K edge of the late 3d elements. This finding is emphasized by the fact that the measured spectra are nicely reproduced by calculated spectra, where the core hole has not been accounted for.

Moreover, a detailed description of the supercell approach has been given. The convergence of the charge density with respect to the size of the supercell has been

thoroughly investigated by monitoring various parameters as the DOS of the ion-ized and of the neutral atoms, as the binding energies of the core states, and as the number of iterations needed to obtain a converged charge density for a given supercell.

The intensity of the quadrupolar 3d→1s transition relative to the dipolar 4p→1s transition has been calculated from first principles. The result has been verified by comparing calculated to measured fluorescence spectra in the case of Ga, Ge, and As, where the 3d fluorescence line is separated from the 4p fluorescence line. Apart from a factor of 1.2 the calculated intensities of the 3d transitions agree with the experimental findings, whereas the measured energies of the 3d fluorescence lines are smaller than the calculated fluorescence energies obtained from the ground state band structure. This effect is due to the screening of the 3d hole existing in the final state if a quadrupolar transition takes place. The calculation of the 3d fluorescence lines in the presence of a 3d hole results in a shift towards smaller energies as expected, however leading to even lower fluorescence energies than in the experiment. To overcome this overestimation of the screening, the $3d^9$ configuration should be treated within a supercell calculation. Moreover, it was extrapolated from the data on As, Ge, Ga, and Zn that in case of Cu a shift of -1eV is necessary to account for the screening of the 3d hole.

The most striking feature of the valence fluorescence lines of the 3d elements is the KNN radiative Auger satellite, which is due to a double ionization process during the emission of a fluorescence photon. The KNN satellite extends between the $K\beta_{1,3}$ and the $K\beta_{2,5}$ valence line dominating the low energy tail of the valence line. In order to be properly considered in the investigation of the Bloch $\vec{k}$-selective valence spectra, the shape of the KNN satellite has been accounted for by a semiempirical model, which was derived from the resonant double differential scattering cross section. The model involves the convolution of an energy loss function with the parent line of the satellite. Investigating the KMN and KMM radiative Auger satellites of Cu this model has been confirmed.

For the first time the relative intensity of the KNN satellite has been investigated. In the range of Z from 27 (Co) to 33 (As) its intensity decreases as a function of the atomic number Z as it is the case for other radiative Auger satellites such as the KMM and the KLL satellites. In contrast to these, the KNN satellite can be as intense as its parent line.

Moreover, in Appendix C the Cu $K\beta'$ and Cu $K\beta''$ satellites, originating from a double ionization during the absorption of a photon, have been examined. From their threshold energy it was possible to confirm that they are due to a 3d spectator hole. The short saturation range of 50 eV corresponding to 0.5 % of the threshold energy indicates that the Cu $K\beta'$ and Cu $K\beta''$ satellites are dominated by shakeup processes.

Making use of the results described above Bloch $\vec{k}$-selective RIXS spectra from Cu have been calculated. Due to the proper consideration of the 3d states and of the KNN satellite they agree well with the measured spectra.

In this work versatile knowledge about the Bloch $\vec{k}$-selective resonant inelastic x-ray scattering process in the hard x-ray regime has been gained. Thanks to the thorough investigation of effects influencing the RIXS process such as electron-phonon interaction, hole screening, and double ionization, processes, the main features of the hard x-ray valence fluorescene line of the late 3d transition metals have been widely understood. Based on the results of this work it is possible to investigate the feasibility of a band structure reconstruction from hard x-ray Bloch $\vec{k}$-selective RIXS spectra, whithout making assumptions about the dispersion of the unoccupied bands. Such an attempt may also be beneficial for further research within the soft x-ray regime.

Appendix A

Details of the Supercells

Atomic Positions in the Supercells

supercell	ATOM	MULT	POS		
4 atoms	1	1	0	0	0
	2	3	$1/2$	0	0
8 atoms	1	1	0	0	0
	2	3	$1/4$	$1/4$	0
		3	$1/2$	$1/4$	$1/4$
	3	1	$1/2$	$1/2$	$1/2$
32 atoms	1	1	0	0	0
	2	3	$1/4$	$1/4$	0
		6	$3/4$	$1/4$	0
		3	$3/4$	$3/4$	0
	3	3	$1/2$	0	0
	4	3	$1/2$	$1/2$	0
	5	3	$1/2$	$1/4$	$1/4$
		6	$3/4$	$1/2$	$1/4$
		3	$3/4$	$3/4$	$1/2$
	6	1	$1/2$	$1/2$	$1/2$

supercell	ATOM	MULT	POS		
108 atoms	1	1	0	0	0
	2	3	$1/6$	$1/6$	0
		6	$5/6$	$1/6$	0
		3	$5/6$	$5/6$	0
	3	3	$1/3$	0	0
		3	$2/3$	0	0
	4	3	$1/3$	$1/3$	0
		6	$2/3$	$1/3$	0
		3	$2/3$	$2/3$	0
	5	6	$1/2$	$1/6$	0
		6	$5/6$	$1/2$	0
	6	3	$1/2$	$1/2$	0
	7	3	$1/3$	$1/6$	$1/6$
		3	$2/3$	$1/6$	$1/6$
		6	$1/3$	$5/6$	$1/6$
		6	$2/3$	$5/6$	$1/6$
		3	$5/6$	$5/6$	$1/3$
		3	$5/6$	$5/6$	$2/3$
	8	6	$1/3$	$1/6$	$1/2$
		6	$2/3$	$1/6$	$1/2$
		6	$2/3$	$5/6$	$1/2$
		6	$1/3$	$5/6$	$1/2$
	9	1	$1/3$	$1/3$	$1/3$
		3	$2/3$	$1/3$	$1/3$
		3	$2/3$	$2/3$	$1/3$
		1	$2/3$	$2/3$	$2/3$
	10	3	$1/2$	$1/2$	$1/3$
		3	$1/2$	$1/2$	$2/3$

ATOM: *number of inequivalent atom*
MULT: *multiplicity of the position*
POS : *position within the unit cell*

The actual atomic positions within the supercell are obtained from the coordinates POS *by means of permutation. The sum of the multiplicities yields the total number of atoms.*

Table A.1: *Atomic positions within the supercells*

DOS of Neutral Atoms in Charged Supercells
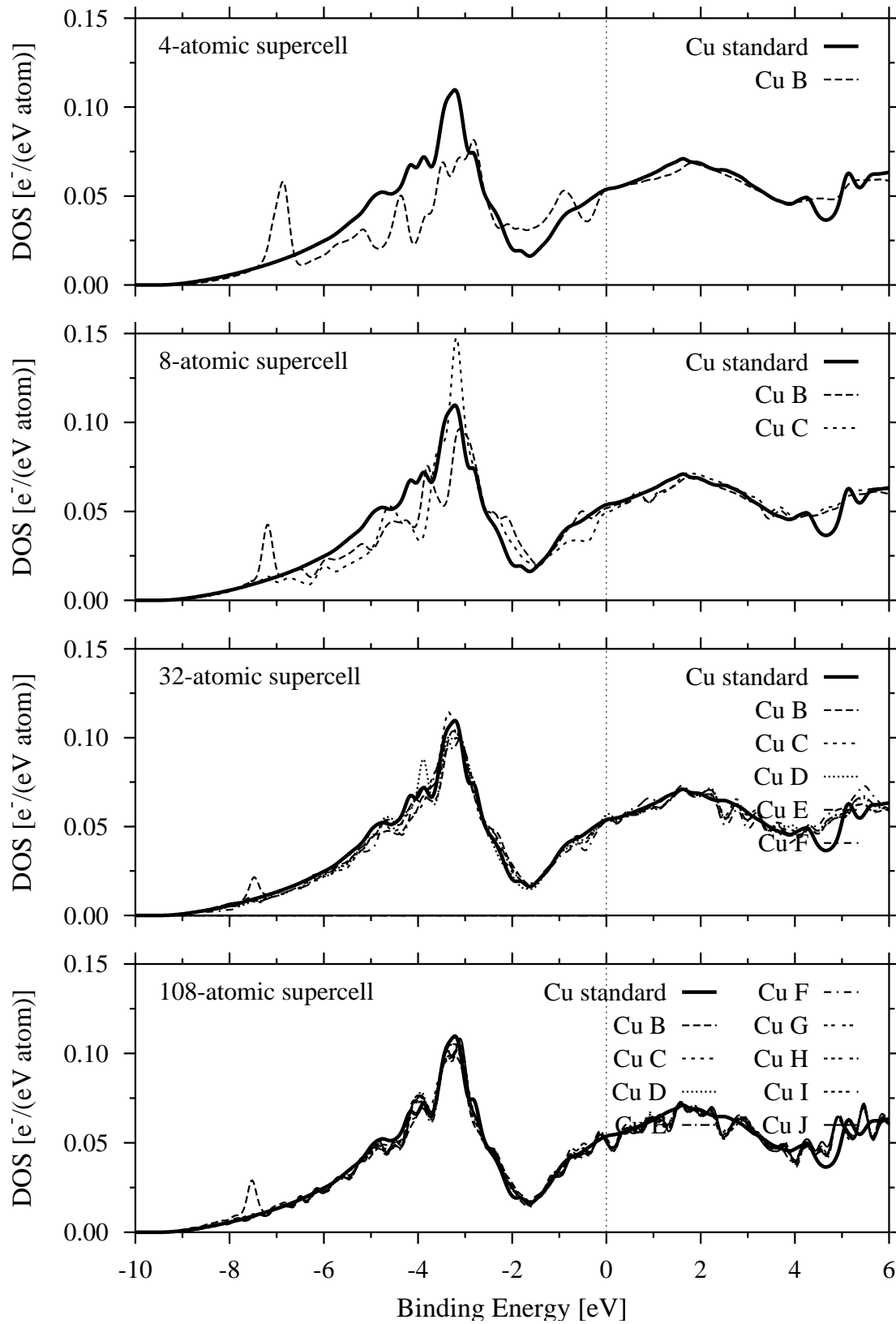
Figure A.1: The 4p-DOS of neutral atoms in charged supercells.
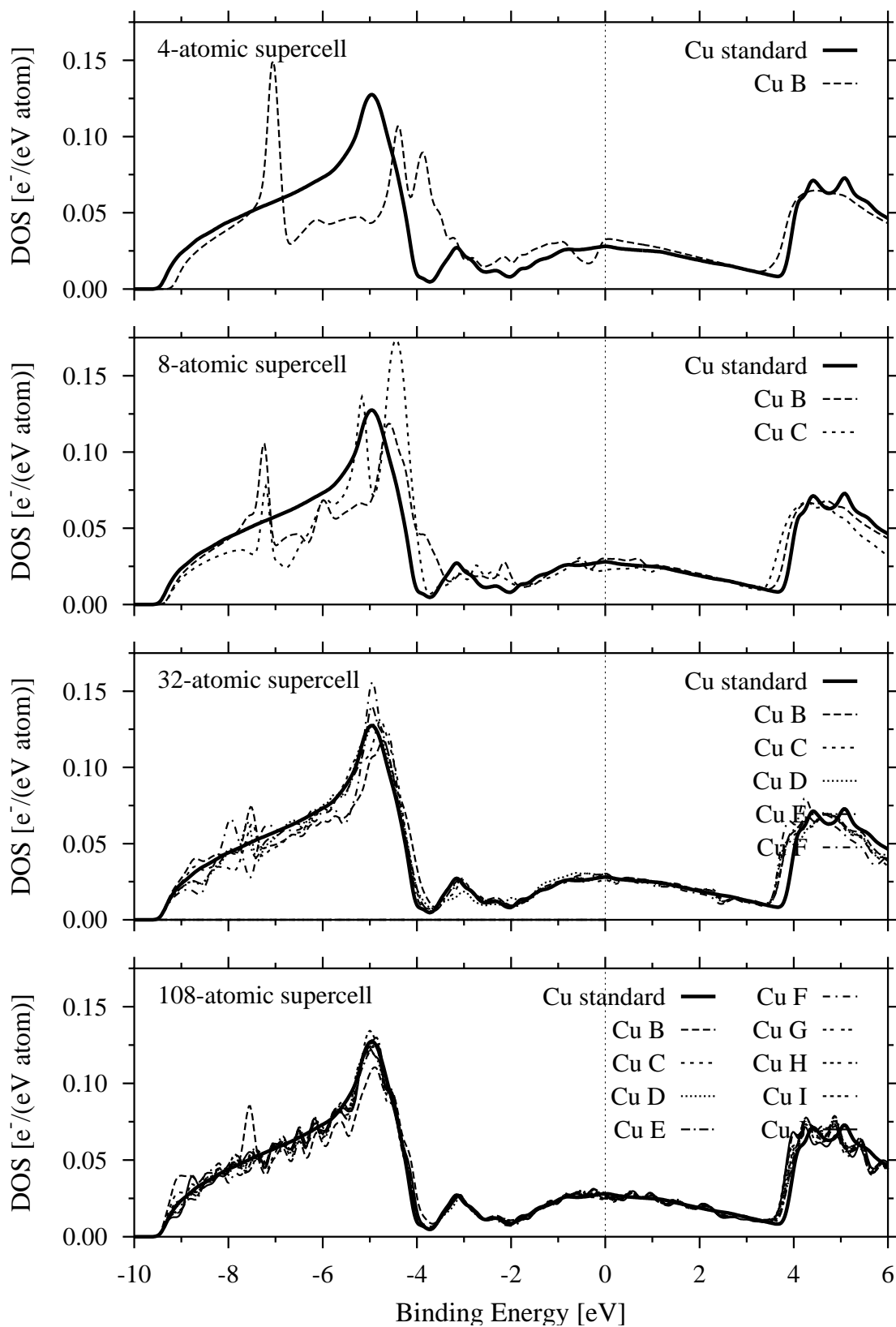
Figure A.2: The 4s-DOS of neutral atoms in charged supercells.

Appendix B

Angular Dependence of Quadrupolar Matrix Elements

The aim of this section, following [Bochar], is to transform the quadrupolar transition operator into an expression containing the Cartesian coordinates of $\vec{k}$ and $\vec{\epsilon}$ as well as the d-like solid harmonics, sometimes referred to as the real spherical harmonics, namely $\mathcal{Y}_{xy}$, $\mathcal{Y}_{yz}$, $\mathcal{Y}_{zx}$, $\mathcal{Y}_{x^2-y^2}$, and $\mathcal{Y}_{z^2}$.

First the product of the two scalar products is figured out and terms containing the same combinations of x, y, and z are combined:

$$
\begin{aligned}
\hat{\epsilon} \cdot \hat{r} \, \hat{k} \cdot \hat{r} &= (\epsilon_x x + \epsilon_y y + \epsilon_z z)(k_x x + k_y y + k_z z) & \text{(B.1)} \\
&= \epsilon_x k_x x^2 + \epsilon_x k_y xy + \epsilon_x k_z xz \\
&+ \epsilon_y k_x xy + \epsilon_y k_y y^2 + \epsilon_y k_z yz \\
&+ \epsilon_z k_x xz + \epsilon_z k_y yz + \epsilon_z k_z z^2 & \text{(B.2)} \\
&= (\epsilon_x k_y + \epsilon_y k_x)\, xy + (\epsilon_y k_z + \epsilon_z k_y)\, yz + (\epsilon_z k_x + \epsilon_x k_z)\, xz & \text{(B.3)} \\
&+ \epsilon_x k_x x^2 + \epsilon_y k_y y^2 + \epsilon_z k_z z^2 & \text{(B.4)}
\end{aligned}
$$

Looking at line B.3 one recognizes that these mixed terms are proportional the d-orbitals $\mathcal{Y}_{xy}$, $\mathcal{Y}_{yz}$, and $\mathcal{Y}_{zx}$, respectively. Thus, only the terms in line B.4 have to be considered further. For the time being the z^2-term is put apart and the x^2 and y^2 terms are extend and recombined:

$$
\begin{aligned}
& \epsilon_x k_x x^2 + \epsilon_y k_y y^2 & \text{(B.5)} \\
={}& +\frac{1}{2}\epsilon_x k_x x^2 \quad +\frac{1}{2}\epsilon_y k_y y^2 \quad +\frac{1}{2}\epsilon_x k_x x^2 \quad +\frac{1}{2}\epsilon_y k_y y^2 \\
& +\frac{1}{2}\epsilon_x k_x y^2 \quad +\frac{1}{2}\epsilon_y k_y x^2 \quad -\frac{1}{2}\epsilon_x k_x y^2 \quad -\frac{1}{2}\epsilon_y k_y x^2 & \text{(B.6)} \\
={}& +\frac{1}{2}\epsilon_x k_x\left(x^2+y^2\right) +\frac{1}{2}\epsilon_y k_y\left(x^2+y^2\right) +\frac{1}{2}\epsilon_x k_x\left(x^2-y^2\right) -\frac{1}{2}\epsilon_y k_y\left(x^2-y^2\right) & \text{(B.7)} \\
={}& +\frac{1}{2}\left(\epsilon_x k_x + \epsilon_y k_y\right)\left(x^2 + y^2\right) \quad +\frac{1}{2}\left(\epsilon_x k_x - \epsilon_y k_y\right)\left(x^2 - y^2\right). & \text{(B.8)}
\end{aligned}
$$

Here the second term of the last line is proportional to the $\mathcal{Y}_{x^2-y^2}$ solid harmonic. The first term will now be treated together with the previously postponed z^2 term.

First one makes use of the fact that $\vec{\epsilon} \cdot \vec{k} = \epsilon_x k_x + \epsilon_y k_y + \epsilon_z k_z = 0$:

$$
\begin{aligned}
\frac{1}{2} \left(\epsilon_x k_x + \epsilon_y k_y\right) \left(x^2 + y^2\right) + \epsilon_z k_z z^2 &= -\frac{1}{2}\epsilon_z k_z \left(x^2 + y^2\right) + \epsilon_z k_z z^2 \\
&= +\frac{1}{2}\epsilon_z k_z \left(2z^2 - x^2 - y^2\right) .
\end{aligned}
\tag{B.9}
$$

Then one notices that $x^2 + y^2 + z^2 = 1 \Leftrightarrow -x^2 - y^2 = z^2 - 1$ yielding

$$
+\frac{1}{2}\epsilon_z k_z \left(2z^2 - x^2 - y^2\right) = +\frac{1}{2}\epsilon_z k_z \left(3z^2 - 1\right) ,
\tag{B.10}
$$

which is proportional to the $\mathcal{Y}_{z^2}$-orbital. Collect the parts and end up with:

$$
\begin{aligned}
\hat{\epsilon} \cdot \hat{r}\, \hat{k} \cdot \hat{r} &= \left(\epsilon_x k_y + \epsilon_y k_x\right) xy + \left(\epsilon_y k_z + \epsilon_z k_y\right) yz + \left(\epsilon_z k_x + \epsilon_x k_z\right) xz \\
&+ \frac{1}{2} \left(\epsilon_x k_x - \epsilon_y k_y\right) \left(x^2 - y^2\right) + \frac{1}{2}\epsilon_z k_z \left(3z^2 - 1\right) .
\end{aligned}
\tag{B.11}
$$

Using the real representations of the $\mathcal{Y}$ to replace the components of $\hat{r}$:

$$
\begin{aligned}
\mathcal{Y}_{z^2} &= \sqrt{\tfrac{5}{16\pi}} \left(3z^2 - 1\right) &\Leftrightarrow& \quad \tfrac{1}{2}\left(3z^2 - 1\right) = \sqrt{\tfrac{4\pi}{15}} \mathcal{Y}_{z^2} \sqrt{3} \\
\mathcal{Y}_{x^2 - y^2} &= \sqrt{\tfrac{15}{16\pi}} \left(x^2 - y^2\right) &\Leftrightarrow& \quad \tfrac{1}{2}\left(x^2 - y^2\right) = \sqrt{\tfrac{4\pi}{15}} \mathcal{Y}_{x^2 - y^2} \\
\mathcal{Y}_{xy} &= \sqrt{\tfrac{15}{4\pi}}\, xy &\Leftrightarrow& \quad xy = \sqrt{\tfrac{4\pi}{15}} \mathcal{Y}_{xy} \\
\mathcal{Y}_{yz} &= \sqrt{\tfrac{15}{4\pi}}\, yz &\Leftrightarrow& \quad yz = \sqrt{\tfrac{4\pi}{15}} \mathcal{Y}_{yz} \\
\mathcal{Y}_{zx} &= \sqrt{\tfrac{15}{4\pi}}\, zx &\Leftrightarrow& \quad zx = \sqrt{\tfrac{4\pi}{15}} \mathcal{Y}_{zx}
\end{aligned}
\tag{B.12}
$$

the quadrupole operator can be written as:

$$
\begin{aligned}
\hat{\epsilon} \cdot \hat{r}\, \hat{k} \cdot \hat{r} &= \Big[\left(\epsilon_x k_y + \epsilon_y k_x\right) \mathcal{Y}_{xy} + \left(\epsilon_y k_z + \epsilon_z k_y\right) \mathcal{Y}_{yz} + \left(\epsilon_z k_x + \epsilon_x k_z\right) \mathcal{Y}_{xz} \\
&+ \left(\epsilon_x k_x - \epsilon_y k_y\right) \mathcal{Y}_{x^2 - y^2} + \sqrt{3}\epsilon_z k_z \mathcal{Y}_{z^2} \Big] \sqrt{\frac{4\pi}{15}} .
\end{aligned}
\tag{B.13}
$$

Since the angular part of s-wave functions is merely a constant, the quadrupolar matrix element between d- and s-orbitals reduces to an integral over two angular functions that is equivalent to the orthonormality condition of the solid harmonics. Thus, the transition intensity $I = |\langle d| \hat{\epsilon} \cdot \hat{r}\, \hat{k} \cdot \hat{r}\, |s\rangle|^2$ amounts to:

$$
\begin{aligned}
I_Q \propto\ & d_{xy} \left(\epsilon_x k_y + \epsilon_y k_x\right)^2 + d_{yz} \left(\epsilon_y k_z + \epsilon_z k_y\right)^2 + d_{xz} \left(\epsilon_z k_x + \epsilon_x k_z\right)^2 \\
&+ d_{x^2 - y^2} \left(\epsilon_x k_x - \epsilon_y k_y\right)^2 + 3d_{z^2} \left(\epsilon_z k_z\right)^2 ,
\end{aligned}
\tag{B.14}
$$

where the d_{xy}, $\ldots$ are the d-partial charges. Along the same lines the angular dependence of dipolar transitions to and from s-orbitals is calculated.

Appendix C

The Onset and Saturation of the Cu Kβ' and Cu Kβ'' Satellites

As already described in Section 7.6, the characteristic shape of the Cu K$\beta_{1,3}$ fluorescence line is due to the spin orbit splitting of the 3p states, giving rise to the asymmetric shape of the main line, and due to the two satellite lines provoking the shoulders at the low energy and the high energy tails of the fluorescence line (see upper left panel of Fig. C.1). These satellites are named Kβ' and Kβ'', respectively, and originate from a double ionization process during the absorption of the incoming photon [Deut95]. This leads to the subsequent emission of a fluorescence photon in the presence of a spectator hole. From a multiplet calculation, taking into account several double hole configurations, Deutsch and coworkers conclude that the Kβ' and Kβ'' satellites stem from the secondary excitation of a 3d electron resulting in a $\underline{3d}$ spectator $\underline{1s3d} \rightarrow \underline{3p3d}$ fluorescence process. Due to the interaction with the incompletely filled 3d-shell the 3p states split up into a multiplet which results in the two satellite lines. That the Kβ' and Kβ'' originate from a $\underline{3d}$ spectator state can be confirmed by monitoring the intensity of the two satellite lines as a function of the incident energy.

In Fig. C.1 spectra recorded at four different incident energies, selected from a series of nine spectra, are shown. Thanks to the consideration of the unoccupied DOS in the calculation of the RIXS spectra, as described in Section 7.4, the respective fit functions resemble even the smaller details of the fine structure. The intensity of the satellite lines decreases faster than the intensity of the main lines as the incident energy is reduced. At $\hbar\omega_1 = 8990$ eV the satellites have almost completely vanished.

The absence of the satellite lines in the spectra measured at lower incident energies leads to instabilities of the fit since in that case more Lorentzians are present than are actually needed to describe the spectra. In fact, the supplementary Lorentzians assume unphysically large widths of several tens of electron volts, occur at positions that are not sensible, and partly have a negative intensity. This failure of the fitfunction clearly indicates that the satellite lines have vanished. Therefore, the positions and widths of the satellite lines have to be determined from the spectra at higher incident energies.

Surprisingly, at incident energies below 9000 eV the sum of the redundant Kβ' and Kβ'' satellite functions amounts to a function having the shape and the energy as expected for the KMN radiative Auger satellite, clearly indicating the presence of
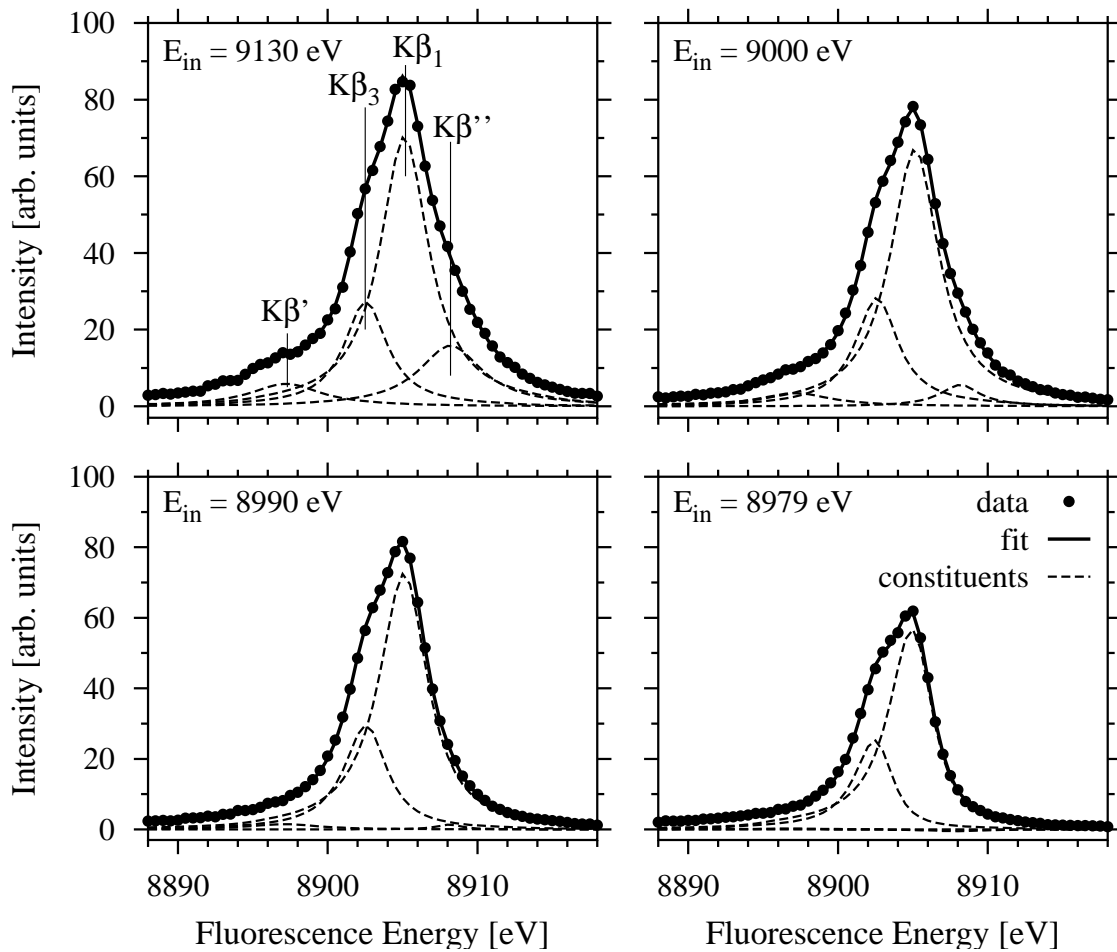
Figure C.1: *Series of RIXS spectra from the Cu $K\beta_{1,3}$ fluorescence line. The measured spectra (dots) are well reproduced by the fit (thick lines) as described in Section 7.6. The constituents of the fit function are depicted in thin lines. The KMN radiative Auger satellite, although present in the fit, has been omitted in the figure.*

the KMN satellite in the spectra. In the work of Deutsch *et al.* [Deut95] a linear background has been subtracted from the measured spectrum, thereby suppressing the KMN satellite.

In a first step the β_1, β_3, and β'' lines have been used to fit the measured spectra in the range between 8900 and 8920 eV. From these fits the position and width of the β'' contribution, as well as the widths of the β_1 and β_3 lines have been determined. These parameters were obtained by letting all parameters float at first and by consecutively fixing one after the other. In a second step the width and the position of the β' line have been acquired. The energy range for the fit was extended over the whole range covered in the experiment (8875 to 8920 eV), and the parameters for the β'' line have been set to the previously determined values. In this fit the shape of the KMN satellite, as extracted from the low energy residua occuring in the spectra at 8979, 8980, and 8985 eV incident energy, has been kept
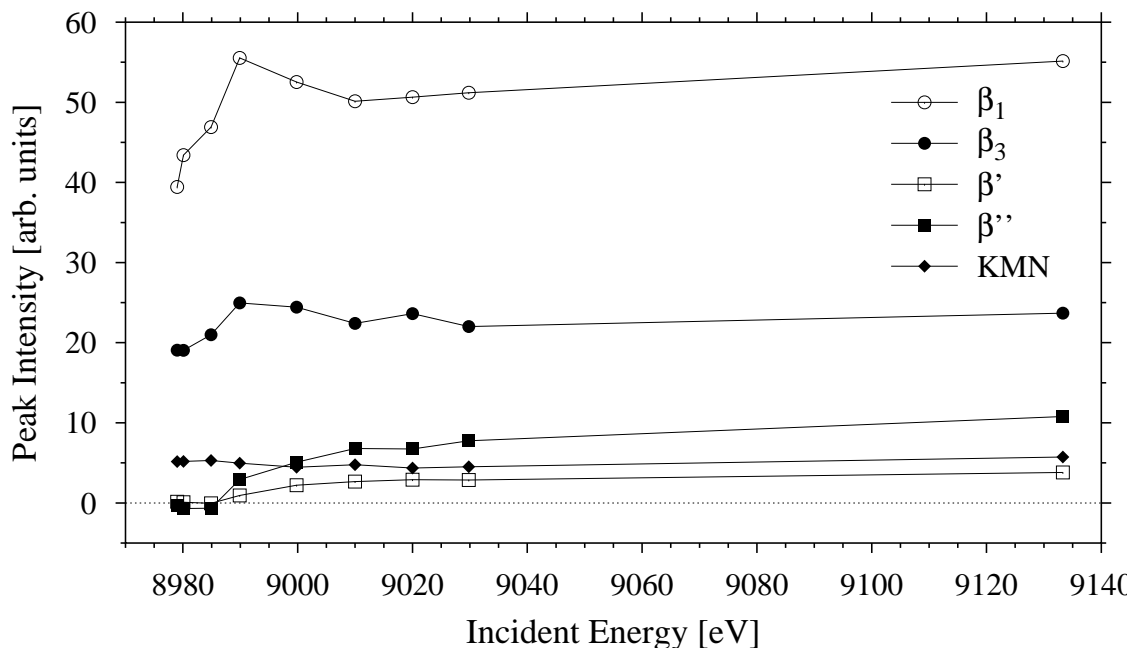
Figure C.2: Peak intensities of the five constituents of the Cu $K\beta_{1,3}$ fluorescence line as a function of the incident energy.

fix. Thus, the free parameters in the final fit were the positions of the $K\beta_1$ and $K\beta_3$ lines, as well as the intensities of all five constituents. The quality of the fit is emphasized by the fact that in the whole series of nine spectra the positions of the two main lines vary by only 0.07 eV and that the relative intensity of the main lines $I_{K\beta_1}/I_{K\beta_3} = 2.22$ varies only by about 6 %.

The peak intensities of the five constituents as a function of the incident energy are depicted in Fig. C.2. The intensities of the $K\beta_1$ and $K\beta_3$ lines resemble the near edge fine structure of the Cu K edge, as far as the limited number of data points permits to say. The intensities of the $K\beta'$ and $K\beta''$ satellite lines steadily decrease with decreasing incident energy and settle around zero below 8990 eV incident energy.

In Fig. C.3 the intensities of the $K\beta'$ and $K\beta''$ satellites normalized to the sum of the $K\beta_1$ and $K\beta_3$ intensities are shown. Apart from a factor of 2.7 the two satellite lines show the same onset behaviour, indicating that these satellites originate from the same shake process.

The onset energy is situated in the energy range between 8985 and 8990 eV, corresponding to 6 and 11 eV above the Cu K edge. From the supercell calculation the 3d binding energy in the presence of a 1s hole is found to be 7.5 eV (see Section 5.5). Additionally, the shift of the 3d states due to the 3d hole screening of about 1 eV must be accounted for (see Chapter 6.5), yielding an onset energy of 8.5 eV which is in good agreement with the experimental finding. Thus it is confirmed that the $K\beta'$ and $K\beta''$ satellites stem from the secondary excitation of a 3d electron resulting in a 3d spectator 1s3d→3p3d fluorescence process.

The intensity of the satellite lines reaches saturation at about 50 eV above the threshold which is 0.5 % of the threshold energy. This short saturation range indi-
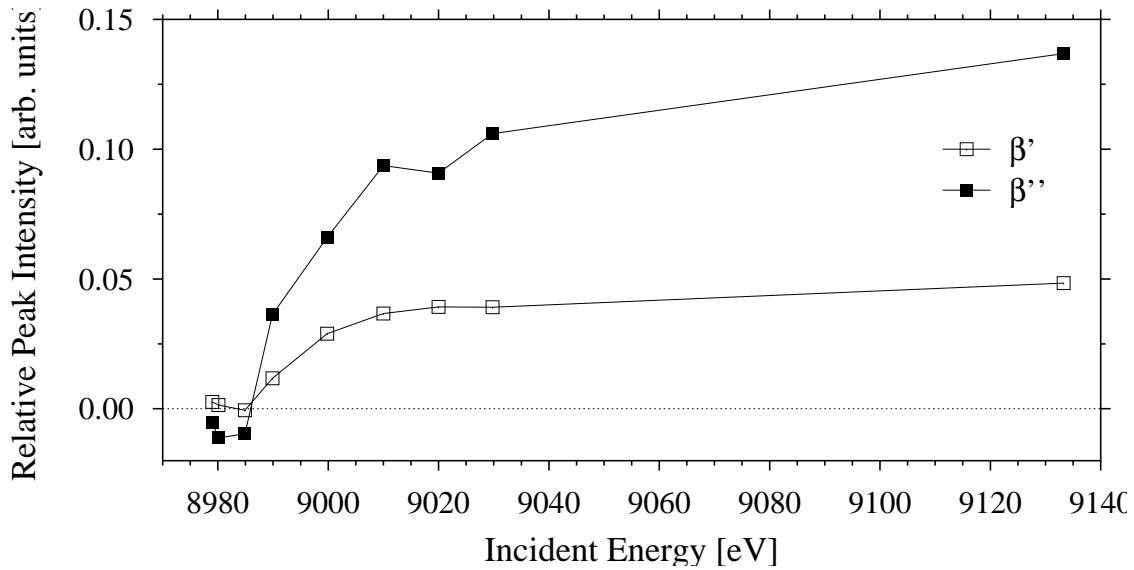
Figure C.3: Relative peak intensities of the Kβ' and Kβ'' satellite lines as a function of the incident energy.

cates that the Kβ' and Kβ'' satellites are dominated by shakeup processes, i.e. the shake electron is excited into localized states. This is in agreement with the fact that the shake processes are governed by the monopole selection rule (see Section 7.2), enforcing that the 3d shake electron is excited into the unoccupied 3d or 4d states, which are more localized than the other conduction band states.

Other shake satellites of Cu exhibit significantly larger saturation ranges. For the Cu K$\alpha_{3,4}$ satellites, stemming from a 2p spectator 1s2p→2p2p transition, a saturation range of 1 keV, or 10 % of the threshold energy, has been reported [Frit98]. The Cu K$^h\alpha_{1,2}$ hypersatellites, that are due to a 1s spectator 1s1s→1s2p transition, show an even larger saturation range. In fact, saturation is not reached at the upper measurement limit of 25 keV, beeing 6.5 keV above the threshold of 18.35 keV [Diam00]. Thus, the lower limit of the saturation range corresponds to 38 % of the threshold energy.

Appendix D

RIXS Spectra from Copper

Figure D.1: Series of Bloch $\vec{k}$-selective RIXS spectra from valence electrons at the K edge of Cu. The spectra have been normalized to the intensiy of the incident radiation.
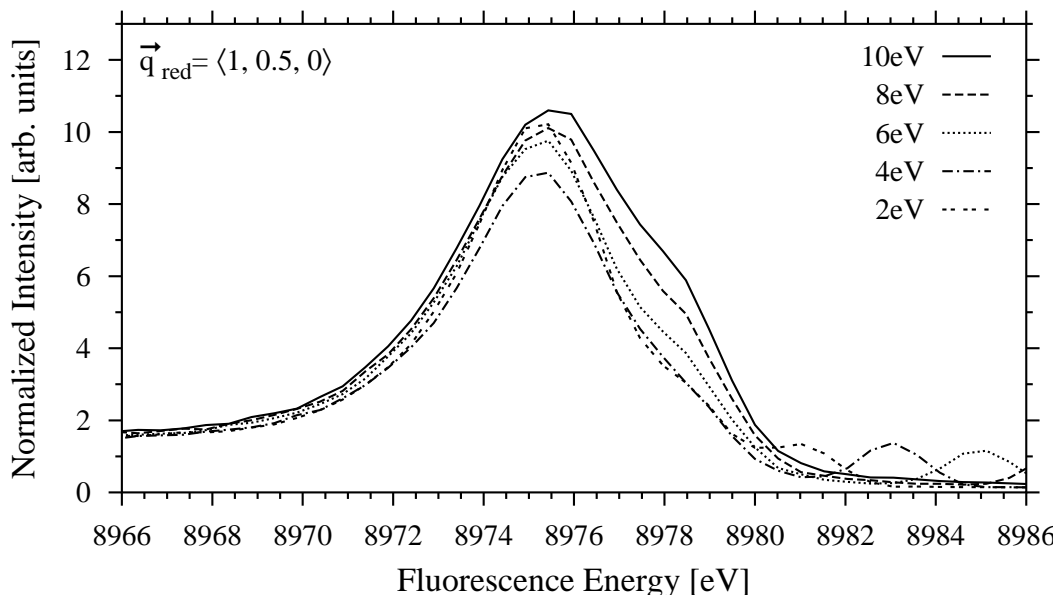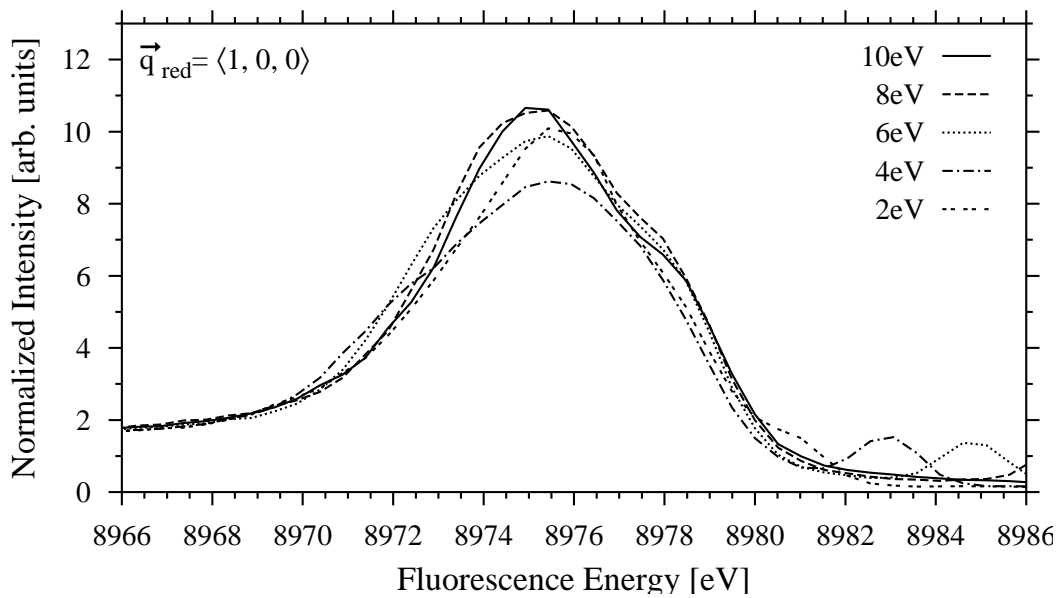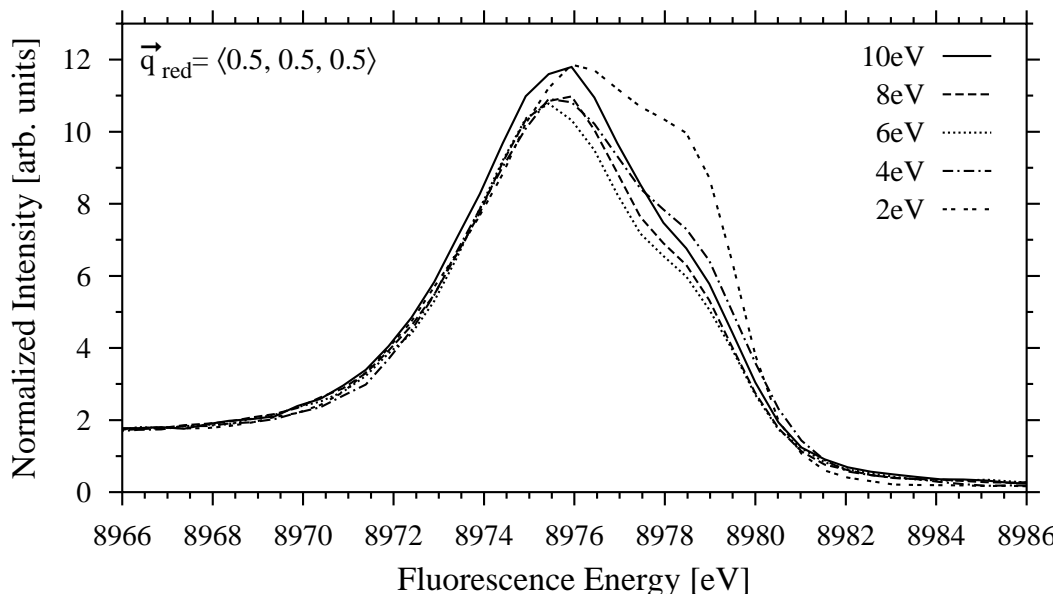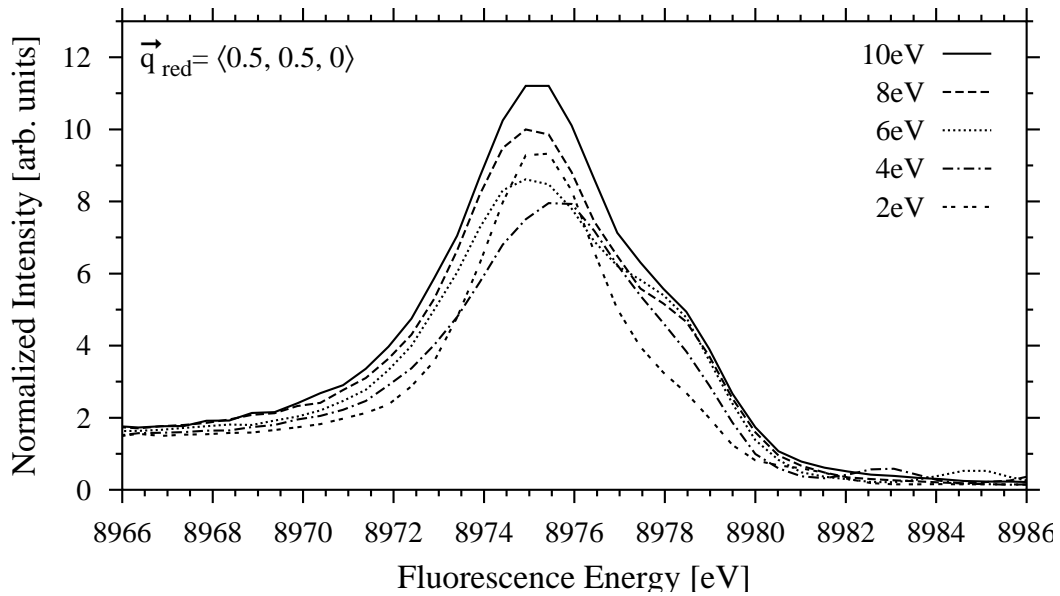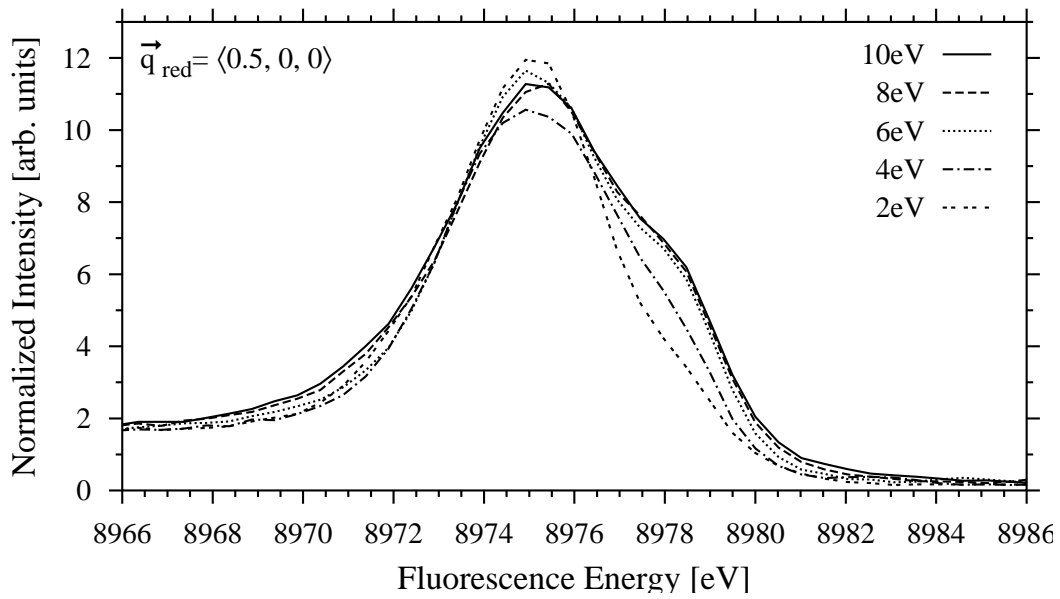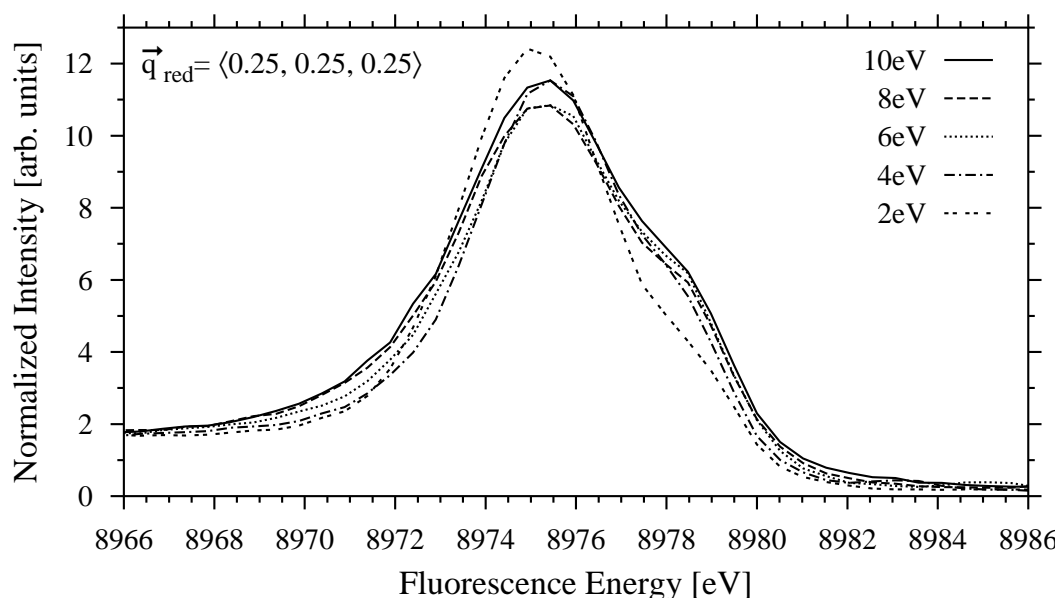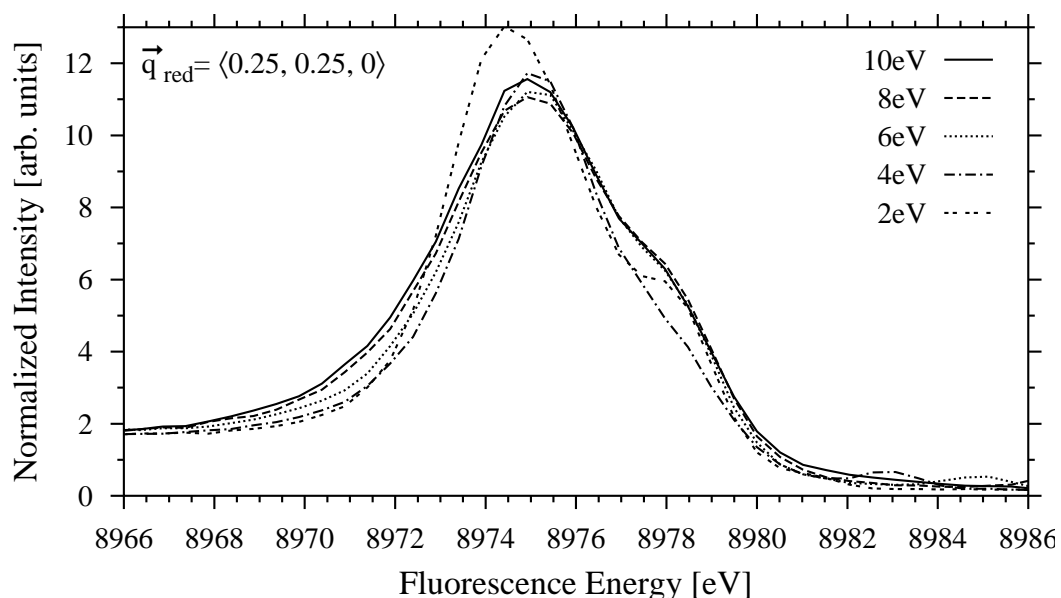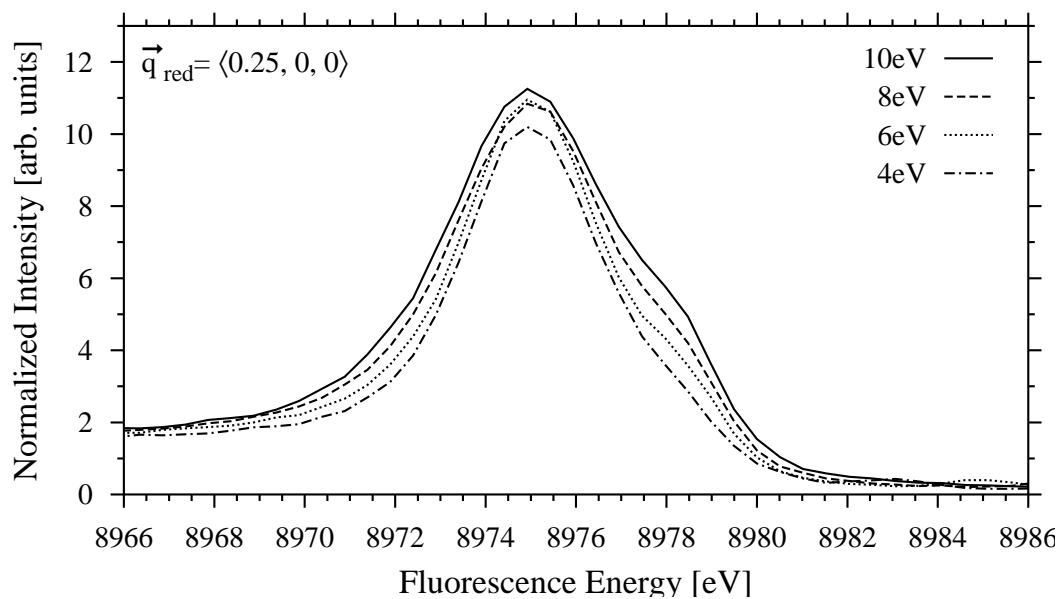
Appendix E

Details of the Experimental Setup

The measured spectra shown in this thesis have been obtained at the HASYLAB and at the ESRF. At the HASYLAB the bending magnet beamline G3 and the wiggler beamline W2 (HARWI), and at the ESRF the undulator beamlines ID28 and ID16 have been used. In all cases the incident synchrotron radiation was monochromatized by means of a double crystal monochromator. At the beamlines G3 and HARWI the monochromator has two separate single crystals, Si 311 at G3 and Si 511 at the HARWI, of which the first monochromator crystal is water cooled to compensate the heat load of the synchrotron radiation. The pre-monochromators of beamlines ID16 and ID28 of the ESRF consist of a liquid N_2 cooled monolithic Si 111 double crystal, which demands an additional two-bounce channel cut crystal to further narrow down the energetic width of the monochromatic beam. The channel cut serves also to compensate for the temperature drift of the pre-monochromators, stabilizing the beam at the selected energy. At ID16 of the ESRF the spot size of the monochromatic beam at the sample is reduced to 100 μm $\times$ 1 mm (hor. $\times$ vert.) by means of two x-ray mirrors. At the HARWI beamline of the HASYLAB the second monochromator crystal is bent sagittally to horizontally focus the wiggler beam, which has a width of 100 mm at the first monochromator crystal. Thereby on the sample a focus of 3 mm $\times$ 5 mm can be achieved. At the beamline G3 of the HASYLAB and at ID28 of the ESRF no focussing elements are available.

In order to obtain a proper normalization of the fluorescence spectra with respect to the intensity of the incoming beam, either a PIN diode (ESRF) or a NaJ detector (HASYLAB) is used. Moreover, at the HASYLAB beamlines an ionization chamber and a Ge-detector have been used to detect the incoming beam and the fluorescence radiation emitted from the sample, respectively, allowing for an additional intensity monitorization of the incoming and of the scattered beam.

The sample was mounted on a sample holder which, in the case of the measurements on Cu at ID16 was fully motorized, allowing for well defined rotation and tilting of the sample, required to select certain momentum transfer vectors $\vec{q}$ (see Chapter 8 Fig. 8.2 and Tab. 8.1). In the case of the temperature dependent measurements on Cu (see Chapter 4), the samples were mounted onto a closed cycle He cryostat, permitting sample temperatures down to 10 K.

The fluorescence radiation emitted from the samples in all cases has been energy analyzed by means of Rowland type single crystal spectrometers, having a Rowland circle radius of $r = 0.5$ m, corresponding to a bending radius of $R = 2r = 1$ m
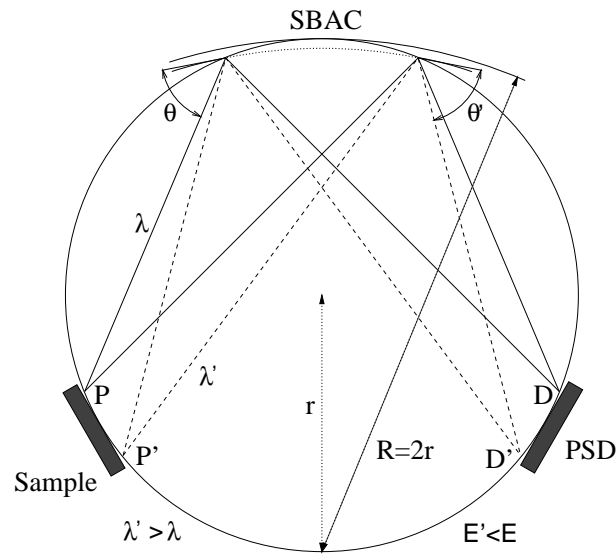
Figure E.1: The principle of a Rowland spectrometer.

for the spherically bent analyzer crystals (SBAC). The principle of the Rowland spectrometer is depicted in Fig. E.1. Photons emitted from one point P of the sample, are hitting the SBAC at different positions, but nevertheless have the same incident angle θ with respect to the spherically bent crystal planes of the analyzer crystal. Via Bragg's law $\lambda = 2d \sin \theta$, d being the distance of the scattering crystal planes, only photons having the wave length λ, corresponding to the energy $E = hc/\lambda$, are reflected from the SBAC and are focussed onto the point D of the detector, which is symmetric to the point P of the sample. X-rays emitted from another point P' of the sample are only then reflected by the SBAC and focussed onto the point D' of the detector, if they have the energy E' matching their incident angle θ'. Thus, each point P of the sample and each point D of the detector corresponds to one certain photon energy E[1]. As a consequence a whole fluorescence spectrum ranging from E' to E can be recorded by means of a position sensitive detector (PSD), if the region between P and P' of the sample is homogeneously illuminated by the incoming beam. The resulting spectrum is referred to as PSD spectrum.

The picture drawn above is true in the strict sense only, if the crystal planes of the SBAC are bent with the radius R and if the surface of the SBAC is curved with the radius r of the Rowland circle. However, since such a single crystal is difficult to produce, the curvature of the surface with r is omitted and the single crystal is only bent with the radius R. The resulting aberration can be neglected as long as the diameter of the SBAC is small compared to the radius r. Moreover, vertical to the rowland circle the crystal planes of the analyzer crystal have to be bent with a radius of $R' = R \sin(\theta)$, which requires a toroidally bent single crystal. Thus, if a spherically bent analyzer crystal is used instead, the resulting aberration is small if θ is close to 90°. A detailed analysis of these effects and their influence on the

---

[1]These x-ray optical properties of the Rowland spectrometer can be easily proven by applying some basic laws of geometry.

energetic resolution of the spectrometer can be found in [Wohl00].

The spectrometers used at the ESRF and at the HASYLAB exhibit several important differences. At the ESRF, the horizontal width of the spot on the sample is less than 100 μm. Therefore, the energetic width of the beam focussed on the detector, depending on the energy and on the analyzer crystal, is about 0.1 eV at 8 keV, in the case of a perfect analyzer crystal. Thus, instead of a position sensitive detector, a PIN diode can be used without degrading the energy resolution of the spectrometer. To measure an x-ray spectrum, the SBAC and the detector are moved to achieve different Bragg angles θ while retaining the Rowland geometry. At the spectrometer used at ID16 and ID28 only the angle of the SBAC with respect to the sample and the position of the detector are changed, but the distances between sample and SBAC, and between SBAC and detector are kept constant.

The spectrometer used at the HASYLAB, where the spot size on the sample measures several square millimeters, is equipped with a position sensitive gas proportional counter having a spatial resolution of 100 μm. Thus, the energy resolution of the spectrometer is only limited by the quality of the SBAC. To measure an x-ray spectrum, a series of PSD spectra obtained at different positionings of the spectrometer have to be combined. In contrast to the ESRF, in the spectrometer at the HASYLAB also the distances between sample, SBAC, and PSD have to be changed, in order not to spoil the resolution of the spectrometer. By acquirering PSD spectra that have a large (i.e. > 90%) overlap with their neighbouring PSD spectra, the resulting fluorescence spectrum is independent of the actual illumination distribution on the sample. A 3-dimensional view of the spectrometer used at the HASYLAB is shown in Fig. E.2.
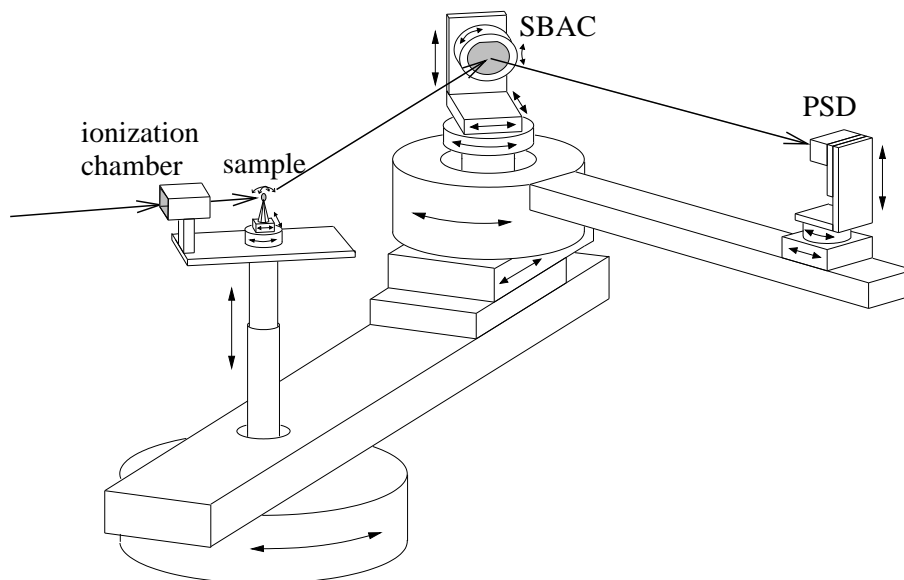
Figure E.2: A 3-dimensional view of the Rowland spectrometer as used at the HASYLAB (Picture reproduced from [Wohl00]).

Bibliography

[Åber71]   T. Åberg, Phys. Rev. A **4**, 1735 (1971). 27, 78, 79

[Åber75]   T. Åberg and J. Utriainen, Sol. Stat. Comm. **16**, 571 (1975). 88

[Atki97]   P. W. Atkins and R. S. Friedman, *Molecular Quantum Mechanics*, 3rd Edition, Oxford University Press (1997). 69

[Bark08]   C. G. Barkla, C. A. Sadler, Philos. Mag. **16**,550 (1908). 1

[Bied81]   L. C. Biedenharn, J. D. Louck, *Angular Momentum in Quantum Physics* in Encyclopedia of Mathematics Vol. 8, Addison-Wesley, 1981. 59

[Boch98]   S. Bocharov, G. Dräger, and D. Heumann, A. Šimůnek and O. Šipr, Phys. Rev. B **58**, 7668 (1998). 69

[Bochar]   S. Bocharov, private communication. 113

[Brou90]   C. Brouder, J. Phys.: Cond. Mat. **2**, 701 (1990). 57, 58

[Broy65]   C. G. Broyden, Math. Comp. **19**, 577 (1965). 23

[Carl75]   T. A. Carlson, *Photoelectron and Auger Spectroscopy*, Plenum Press, New York (1975). 77, 78

[Carl95]   J. A. Carlisle, E. L. Shirley, E. A. Hudson,L. J. Terminello, T. A. Callcott, J. J. Jia, D. L. Ederer, R. C. C. Perera, F. J. Himpsel, Phys. Rev. Lett. **74**, 1234 (1995). 2

[Carl99]   J. A. Carlisle, E. L. Shirley, L. J. Terminello, J. J. Jia, T. A. Callcott, D. L. Ederer, R. C. C. Perera, F. J. Himpsel, Phys. Rev. B **59**, 7433 (1999). 2

[Coop85]   M. J. Cooper, Rep. Prog. Phys. **48**, 415 (1985). 10

[Deut95]   M. Deutsch, G. Hölzer, J. Härtwig, J. Wolf, M. Fritsch and E. Förster, Phys. Rev. A **51**, 283 (1995). 11, 74, 89, 90, 91, 115, 116

[Diam00]   R. Diamant, S. Huotari, K. Hämäläinen, C. C. Kao, and M. Deutsch, Phys. Rev. Lett. **84**, 3278 (2000). 11, 74, 118

[Dräg84]   G. Dräger and O. Brümmer, Phys. Stat. Sol. B **124**, 11 (1984). 55

[Dräg88]   G. Dräger, R. Frahm, G. Materlik, and O. Brümmer, Phys. Stat. Sol. B
           146, 287 (1988). 55

[Druy27]   M. J. Druyvesteyn, Zeitschrift für Physik **43**, 707 (1927). 73

[Eise99]   S. Eisebitt, J. Lüning, J.-E. Rubensson, A. Karl, W. Eberhardt,
           Phys. Stat. Sol. B **215**, 803 (1999). 2

[Eise00]   S. Eisebitt, W. Eberhardt, J. El. Spec. Rel. Phen. **110**, 335 (2000). 12,
           34, 35

[Enki98]   H. Enkisch, *Experimente zur $\vec{k}$-Selektivität der Resonant Inelatischen
           Röntgenstreuung an Valenzelektronen des Kupfers*, diploma thesis, Uni-
           versity of Dortmund (1998). 28

[Enki99]   H. Enkisch, A. Kaprolat, W. Sch"ulke, M.H. Krisch, M. Lorenzen,
           Phys. Rev. B **60**, 8624 (1999).

[Frit98]   M. Fritsch, C. C. Kao, K. Hämäläinen, O. Gang, E. Förster, and
           M. Deutsch, Phys. Rev. A **57**, 1686 (1998). 74, 118

[Hämä89]   K. Hämäläinen, S. Manninen, P. Suortti, S. P. Collins, M. J. Cooper,
           D. Laundy, J. Phys.: Cond. Mat. **1**, 5955 (1989). 1

[Hohe64]   P. Hohenberg and W. Kohn, Phys. Rev. **136**, B864 (1964). 17

[Jia96]   J. J. Jia, T. A. Callcott, E. L. Shirley, J. A. Carlisle, L. J. Ter-
           minello, A. Asfaw, D. L. Ederer, F. J. Himpsel, R. C. C. Perera,
           Phys. Rev. Lett. **76**, 4054 (1996). 2

[John94]   P. D. Johnson, Y. Ma, Phys. Rev. B **49**, 5024 (1994). 2, 35

[Kao96]   C. C. Kao, W. A. Caliebe, J. B. Hastings, K. Hämäläinen, and
           H. M. Krisch, Rev. Sci. Instrum. **67**, 1 (1996). 25, 100

[Kesk74]   O. Keski-Rahkonen and J. Utriainen, J. Phys. B: Atom. Molec. **7**, 55
           (1974). 79

[Kesk80]   O. Keski-Rahkonen and J. Ahopelto, J. Phys. C: Solid St. Phys. **13**, 471
           (1980). 79, 93, 94, 95

[Koel75]   D. D. Koelling and G. O. Arbman, J. Phys. F: Metal Phys. **5**, 2041
           (1975). 22

[Kohn65]   W. Kohn, and L. J. Sham, Phys. Rev. **140**, A1133 (1965). 18

[Koo90]   Y. D. Koo and K. Das Gupta, Phys. Rev. A **42**, 5441 (1990). 79

[Krau68]   M. O. Krause, T. A. Carlson, and R. D. Dismukes, Phys. Rev. **170**, 37
           (1968). 89

[LandBö]   Landold-Börnstein, 6th Ed. Vol. II-1, pages 380 and 428f. 37

[Livi88]   P. Livins and S. E. Schnatterly, Phys. Rev. B **37**, 6731 (1988). 75, 88, 89

[Löwd55]   P.-O. Löwdin, Phys. Rev. **97**, 1474 (1955). 78

[Lüni97]   J. Lüning, J.-E. Rubensson, C. Ellmers, S. Eisbitt, W. Eberhardt, Phys. Rev. B **56**, 13147 (1997). 2, 34, 35

[Lytle]   F. D. Lytle, The XAFS Database, http://xafsdb.iit.edu:80/database/data/Farrel_Lytle_data/.

[Ma92]   Y. Ma, N. Wassdahl, P. Skytt, J. Guo, J. Nordgren, P. D. Johnson, J.-E. Rubensson, T. Boske, W. Eberhardt, S. D. Kevan, Phys. Rev. Lett. **69**, 2598 (1992). 1, 2

[Ma94]   Y. Ma, Phys. Rev. B **49**, 5799 (1994). 2, 12, 34

[Ma95a]   Y. Ma, M. Blume, Rev. Sci. Instr. **66**, 1543 (1995). 2

[Ma95b]   Y. Ma, K. E. Miyano, P. L. Cowan, Y. Aglitzkiy, B. A. Karlin, Phys. Rev. Lett. **74**, 478 (1995). 2

[Magd01]   U. Magdans, *Die Messung der spinpolarisierten unbesetzten 5d Zustandsdichte von Eu in EuO*, diploma thesis, University of Dortmund (2001). 86

[Müll82]   J. E. Müller, O. Jepsen, and J. W. Wilkins, Sol. Stat. Comm. **42**, 365 (1982). 53

[Miya93]   K. E. Miyano, D. L. Ederer, T. A. Callcott, W. L. O'Brian, J. J. Jia, L. Zhou, Q.-Y. Dong, Y. Ma, J. C. Woicik, D. R. Müller, Phys. Rev. B **48**, 1918 (1993). 1

[Neck75]   A. Neckel, K. Schwarz, R. Eibler, P. Rastl und P. Weinberger, Microchim. Acta, Suppl. **6**, 257 (1975). 64

[Perd92]   J. P. Perdew and Y. Wang, Phys. Rev. B **45**, 13244 (1992). 19

[Perd96]   J. P. Perdew, S. Burke, M. Ernzerhof, Phys. Rev. Lett. **77**, 3865 (1996). 19

[Pire64]   J. Pirenne and P. Longe, Physica **30**, 277 (1964). 75, 88, 89

[Rose57]   M. E. Rose, *Elementary Theory of Angular Momentum*, Wiley and Sons (1957). 59

[Rube90]   J.-E. Rubensson, D. Müller, R. Shuker, D. L. Ederer, C. H. Zhang, j. Jia, T. A. Callcott, Phys. Rev. Lett. **64**, 1047 (1990). 1

[Schü91]   W. Schülke, in *Handbook on Synchrotron Radiation,* Vol. 3, Chap. 15, edited by G. Brown and D. E. Moncton, Elsevier Science Publishers B. V. Amsterdam (1991). 10

[Schü95]   W. Schülke, A. Kaprolat, T. Fischer, K. Höppner, F. Wohlert, Rev. Sci. Instrum. **66**, 2446 (1995). 25, 89, 100

[Scof74]   J. H. Scofied, Phys. Rev. A **9**, 1041 (1974). 79

[Serv75]   A. Servomaa and O. Keski-Rahkonen, J. Phys. C: Solid St. Phys. **8**, 4124 (1975). 79

[Shir98]   E. L. Shirley, Phys. Rev. Lett. **80**, 794 (1998).

[Shir01]   E. L. Shirley, J. A. Soininen, G. P. Zhang, J. A. Carlisle, T. A. Callcott, D. L. Ederer, L. J. Terminello, R. C. C. Perera, J. El. Spec. Rel. Phen. **114**, 939 (2001). 2, 103

[Sing94]   D. J. Singh, *Planewaves Pseudopotentials and the LAPW Method*, Kluwer Academic Publishers (1994). 17

[Ster00]   C. Sternemann, A. Kaprolat, M. H. Krisch, and W. Schülke, Phys. Rev. A **61**, 20501(R) (2000). 11, 41, 56, 74, 80

[Utri73]   J. Utriainen, M. Linkoaho and T. Åberg, *Proc. Int. Symp. X-Ray Spectra and Electronic Structure of Matter, Munich*, vol. **1**, 382 (1973). 79

[Veen97]   M. van Veenendaal and P. Carra, Phys. Rev. Lett. **78**, 2839 (1997). 25

[Wien97]   P. Blaha, K. Schwarz, and J. Luitz, **WIEN97**, Vienna University of Technology, 1997.
Improved and updated UNIX version of the original copyrighted WIEN-code, which was published by P. Blaha, K. Schwarz, P. Sorantin, and S. B. Trickey in Comput. Phys. Commun. **59**, 399 (1990). 28, 65

[Wohl00]   F. N. Wohlert, *Ein hochauflösendes Spektrometer für die resonant unelastische Röntgen-Streuung*, doctoral thesis, University of Dortmund (2000). 33, 89, 125

[Zsch89]   G. Zschornack, *Atomdaten für die Röntgenspektralanalyse*, Springer (1989). 29, 53, 90, 94

List of Figures

131

List of Tables

Acknowledgement